Décrochage tournant dans un diffuseur lisse radial : Étude de stabilité et effet sur la performance.

Yaguang Heng

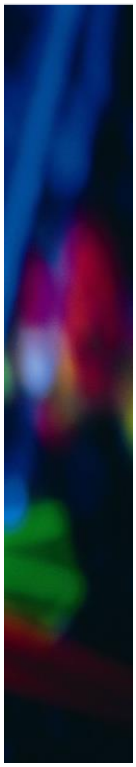

2017-ENAM-0049

École doctorale n° 432 : Sciences des Métiers de l'ingénieur

Doctorat ParisTech

T H È S E

pour obtenir le grade de docteur délivré par

l'École Nationale Supérieure d'Arts et Métiers

Spécialité "Mécanique-matériaux (AM)"

présentée et soutenue publiquement par

Yaguang HENG

le 15 Décembre 2017

Décrochage tournant dans un diffuseur lisse radial: Étude de stabilité et effet sur la performance

Directeur de thèse : **Antoine DAZIN**
Co-encadrement de la thèse : **Najib OUARZAZI**

Jury

M. Jean-Christophe ROBINET, Professeur, DYNFLUID Laboratory, Arts et Métiers ParisTech (Paris)	Président
M. Pascal FERRAND, Directeur de recherche, CNRS. Laboratoire de Mécanique des Fluides et d'Acoustique, Ecole Centrale de Lyon	Rapporteur
M. Nicolas BINDER, Professeur associé, ISAE-SUPAERO	Rapporteur
M. Antoine DAZIN, Professeur, Laboratoire de Mécanique de Lille, Arts et Métiers ParisTech (Lille)	Examinateur
M. Najib OUARZAZI, Professeur, Laboratoire de Mécanique de Lille, Université Lille 1	Examinateur
M. Alexandre DELACHE, Maître de Conférences, Laboratoire de Mécanique des Fluides et d'Acoustique, Université Jean Monnet de Saint-Etienne	Examinateur

T H È S E

Arts et Métiers ParisTech - Campus de Lille
Laboratoire de Mécanique de Lille

N° d'ordre:

École Nationale Supérieure d'Arts et Métiers

T H È S E

présentée en vue

d'obtenir le grade de

Docteur

en

Mécanique

Par

Yaguang HENG

DOCTORAT DELIVRÉ PAR L' ÉCOLE NATIONALE SUPÉRIEURE D'ARTS ET MÉTIERS

Titre de la Thése:

Décrochage tournant dans un diffuseur lisse radial: Étude de stabilité et effet sur la performance

Rotating instability in a radial vaneless diffuser: stability analysis and effect on the performance

Soutenue le Decembre 2017 devant le jury d'examen:

Jury

M. Jean-Christophe ROBINET, Professeur, DYNFLUID Laboratory, Arts et Métiers ParisTech (Paris)	Président
M. Pascal FERRAND, Directeur de recherche, CNRS, Laboratoire de Mécanique des Fluides et d'Acoustique, Ecole Centrale de Lyon	Rapporteur
M. Nicolas BINDER, Professeur associé, ISAE-SUPAERO	Rapporteur
M. Antoine DAZIN, Professeur, Laboratoire de Mécanique de Lille, Arts et Métiers ParisTech (Lille)	Examinateur
M. Najib OUARZAZI, Professeur, Laboratoire de Mécanique de Lille, Université Lille 1	Examinateur
M. Alexandre DELACHE, Maître de Conférences, Laboratoire de Mécanique des Fluides et d'Acoustique, Université Jean Monnet de Saint-Etienne	Examinateur

Thése préparée au Laboratoire de Mécanique de Lille

École Doctorale nº 432: Sciences des métiers de l'ingénieur

Contents

Contents 3
List of figures 5
List of tables 8
Symbols 9
Introduction 13
1 Literature review 15
1.1 Introduction 15
1.2 Rotating stall in turbomachineries 15
1.3 Rotating stall in radial diffusers 17
1.3.1 In vaned diffusers 17
1.3.2 In vaneless diffusers 18
1.3.2.1 Three dimensional rotating stall 22
1.3.2.2 Two dimensional rotating stall 24
1.3.3 Effects of the geometry 28
1.3.4 Pressure losses in vaneless diffusers 30
1.3.5 Control methods for diffuser rotating stall 31
1.4 Research object and method 33
2 Experimental study 35
2.1 Introduction 35
2.2 Experimental test rig 36
2.2.1 SHF radial impeller 36
2.2.2 Vaneless diffuser 37
2.2.3 Brüel & Kjaer condenser microphones 38
2.3 Impeller and diffuser performance 38
2.3.1 Pressure measurements 38
2.3.2 Flow rate calibration 41
2.3.2.1 Flow rate from the tank Q_T 42
2.3.2.2 Leakage flow Q_{L1} 44
2.3.2.3 Leakage flow Q_{L2} 44
2.4 Vaneless diffuser rotating stall 45
2.4.1 Spectrum analysis 45

2.4.2 Characteristics of rotating stall 49
2.4.2.1 Number of stall cells 49
2.4.2.2 Propagation velocity of stall cells 51
2.5 Effect of rotating stall on the diffuser performance 53
2.6 Effect of the geometrical configuration 62
2.7 Conclusions 64
3 Linear stability analysis 67
3.1 Introduction 67
3.2 Hypotheses 67
3.3 Linear model 68
3.3.1 Dimensional equations and basic solutions 68
3.3.2 Dimensionless form 71
3.3.3 Linearization 72
3.3.4 Normal Modes Analysis 73
3.3.5 Solutions of linear stability analysis 73
3.4 Results of linear stability analysis 77
3.4.1 Critical flow angle and propagation velocity 77
3.4.2 The growth rate of stall mode 80
3.4.3 Comparison between theory and experiment for case R = 1.5 84
3.4.4 Velocity vector and pressure distribution 86
3.4.5 Analysis of the perturbed flow 92
3.4.6 Characteristic times associated with the convection of a perturbation 95
3.5 Discussions and conclusions 97
4 Weakly nonlinear stability analysis 99
4.1 Introduction 99
4.2 Governing equations for finite amplitude disturbances 99
4.3 Derivation of the amplitude equation 100
4.3.1 First order solutions 101
4.3.2 Adjoint problem 102
4.3.3 Second order solutions 105
4.3.4 Third order solvability condition 106
4.4 Comparison with experimental results 109
5 Conclusions and future works 111

5.1 Conclusions 111
5.2 Future works 113
Appendix A Diffuser leakages 115
A.1 Diffuser upper side leakage 115
A.2 Diffuser lower side leakage 115
Appendix B Frequency spectra 117
Appendix C Spectrum analysis 121
Appendix D Pressure recovery 123
Bibliography 127

List of figures

Figure 1.1 Evolutions of rotating stall in shrouded (left) and unshrouded (right) centrifugal impellers (Lennemann and Howard, 1970) 16
Figure 1.2 Vaned diffuser rotating stall (Lejvar, 2007) 17
Figure 1.3 Rotating stall in vaneless diffuser: (a) radial, (b) tangential, and (c) axial velocity distributions. (d) velocity vectors (Dazin et al, 2011) 18
Figure 1.4 Variation of non-dimensional rotational speed with the diffuser inlet flow angle (Jansen, 1964(a), Abdelhamid et al, 1979) 19
Figure 1.5 Waveforms of the pressure signals at stall conditions: (a) Abdelhamid and Bertrand, 1979 (b) Abdelhamid et al, 1979 20
Figure 1.6 Phase-averaged radial velocity distributions with diffuser radius ratio and axial distance (Shin et al,1998) 20
Figure 1.7 Narrow and wide vaneless diffusers (Lejvar, 2007) 21
Figure 1.8 Stable operating range of the flow in the vaneless diffuser (Jansen, 1964a) 22
Figure 1.9 Effects of the diffuser inlet (a) Reynolds number and (b) flow angle on the wall boundary layer flow angle (Dou and Mizuki, 1998) 23
Figure 1.10 Separation locations versus the diffuser inlet flow angle (Dou and Mizuki, 1998) 24
Figure 1.11 The critical flow angle and propagation velocity of rotating stall versus diffuser radius ratio (Tsujimoto et al, 1996) 26
Figure 1.12 Contours of velocity magnitude from stable to unstable conditions (Ljevar, 2007) 27
Figure 1.13 Variation of *K* (ratio between total losses and wall friction losses) versus the mean inlet flow angle (Dou, 1991) 31
Figure 1.14 Stall control by jet flow (Tsurusaki and Kinoshita, 2001) 32

Figure 1.15 Radial grooves used for stall suppression (Kurokawa et al, 2000) 32
Figure 1.16 J-groove structure (Saha et al, 2001) 33

Figure 2.1 Experimental test rig 35
Figure 2.2 Inner structure of the tank 36
Figure 2.3 SHF radial impeller 36
Figure 2.4 Vaneless diffuser 38
Figure 2.5 Brüel & Kjaer condenser microphone (Type 4135) 38
Figure 2.6 Pressure measurement in suction pipe 39
Figure 2.7 Pressure taps on the diffuser 40
Figure 2.8 (a) The Sélecteur BEXHILL: 20 pneumatic channels. (b) Thermo – hygrometer: DOSTMANN T870. (c) YEW digital manometer (Type 2654). (d) Mercury manometer 41
Figure 2.9 Leakage flow in the system 41
Figure 2.10 Diaphragm on the inlet tank 42
Figure 2.11 Flow rate coefficient versus the inner diameter of the diaphragm 42
Figure 2.12 Local quantities in the tank and atmosphere 43
Figure 2.13 The joint shapes between impeller and diffuser at upper and lower side 44
Figure 2.14 Pump and diffuser performance curves (Static pressure rise, the x-axis for the pump and diffuser performance is respectively the impeller flow rate Q and the diffuser flow rate Q_D) 45
Figure 2.15 Cross-power spectra at two impeller angular velocities 46
Figure 2.16 Cross-power spectra at different flow rates 49
Figure 2.17 Phase difference in the spectrum 50
Figure 2.18 Angle difference between two microphones 50
Figure 2.19 Dominant stall mode at $Q/Q_d = 0.26$ (Dazin et al., 2008) 51
Figure 2.20 The amplitude (a) and circumferential velocity (b) of stall cells for 1200 RPM .. 52
Figure 2.21 Velocity triangles at impeller outlet (diffuser inlet) 52
Figure 2.22 Diffuser static pressure recovery versus flow rate ratio (P_4 – Diffuser outlet pressure, P_3 – Diffuser inlet pressure) 53
Figure 2.23 Pressure recovery curve at design flow rate $Q/Q_d = 1.0$ 54
Figure 2.24 Moody diagram 55
Figure 2.25 Streamline in the vaneless diffuser 56
Figure 2.26 Length of streamline versus the flow rate 57

Figure 2.27 Experimental Diffuser loss coefficient at diffuser outlet versus length of streamline 58
Figure 2.28 Losses at diffuser outlet versus flow rate ratio Q/Q_d 58
Figure 2.29 Diffuser losses coefficient versus static pressure recovery coefficient 59
Figure 2.30 Radial velocity in the vaneless diffuser at Q/Q_d = 0.26 (Dazin et al., 2011) 60
Figure 2.31 Two assumed regions in the vaneless diffuser 60
Figure 2.32 Assumption of the real streamline 61
Figure 2.33 Comparison between experimental losses and corrected losses 61
Figure 2.34 Convection at the diffuser outlet 62
Figure 2.35 Comparison of the critical flow rate for the dominant stall modes 63
Figure 2.36 Comparison of the critical flow angle for the dominant stall modes 63
Figure 2.37 Flow field in the vaneless diffuser (Pavesi et al, 2011) 64

Figure 3.1 Velocity triangle at impeller outlet 67
Figure 3.2 Flow in the vaneless Diffuser 68
Figure 3.3 Calculation process of μ and ω_{real} by Mathematica 78
Figure 3.4 Comparisons between present results and Tsujimoto et al (1996) 79
Figure 3.5 Critical flow angle (a) and propagation velocity (b) versus the diffuser radius ratio (Ljevar, 2007) 80
Figure 3.6 Comparisons of critical flow angle and propagation velocity with experiments (Tsujimoto et al, 1996) 81
Figure 3.7 Calculation of σ and ω_{real} by Mathematica 82
Figure 3.8 Growth rates of instabilities for different cases 83
Figure 3.9 Propagation velocity of cases R = 2 and 2.5 84
Figure 3.10 Comparison of propagation velocity between experiment and theory (R = 1.5) .. 85
Figure 3.11 The dominant stall mode for R = 1.5 85
Figure 3.12 Comparison of the velocity distribution 88
Figure 3.13 Comparison of the radial and tangential velocity components 90
Figure 3.14 Comparisons of the pressure fluctuation between present results and literatures 92
Figure 3.15 Contributions of the two parts on the instability: R = 2, n = 4 95
Figure 3.16 New perturbation and the stall cell in the vaneless diffuser 95
Figure 3.17 Comparison of tan α and $n(r_4/r_3\text{-}1)(1\text{-}k)/2\pi$ 97

Figure 4.1 Supercritical bifurcation diagram in the case of positive coefficient γ_r (the solid line represents stable solution while the dashed line represents unstable solution) 108

Figure 4.2 Subcritical bifurcation diagram in the case of negative coefficient γ_r (the solid line represents stable solution while the dashed line represents unstable solution) 109

Figure 4.3 Slopes of the experimental angular velocity of rotating stall 109

Figure B1 Crosspower spectra at all tested flow rates 119

Figure D1 Theoretical and experimental pressure recovery in the vaneless diffuser 126

List of tables

Table 2.1 Impeller geometries 37

Table 2.2 Geometries of the vaneless diffuser 37

Table 2.3 The radii of 9 pressure taps 39

Table 2.4 Technical data of the thermo-hygrometer – DOSTMANN T870 40

Table 2.5 Different modes of rotating stall 50

Table 3.1 Critical flow angle for different parameters 77

Table 3.2 Critical propagation velocity for different parameters 78

Table 4.1 Comparison of the slope of angular frequency 110

Table A1 Leakage flow in the vaneless diffuser 116

Table C1 Spectrum analysis at $Q/Q_d = 0.26$ 121

Table C2 Spectrum analysis at $Q/Q_d = 0.36$ 121

Table C3 Spectrum analysis at $Q/Q_d = 0.47$ 121

Table C4 Spectrum analysis at $Q/Q_d = 0.56$ 122

Table C5 Spectrum analysis at $Q/Q_d = 0.58$ 122

Table D1 Loss coefficients at diffuser outlet 126

Symbols

Latin letters		
Symbol	**Definition**	**Unit**
B_2	Impeller outlet width	mm
B_3	Diffuser width	mm
C	Constant	(–)
C_P	Perimeter of the cross-section of the vaneless diffuser	m^2
D	Diameter	mm
D_H	Hydraulic diameter	(–)
D_S	Diameter of the suction pipe	m
f	Frequency	Hz
f_{BPF}	Blade passing frequency	Hz
f_{imp}	Impeller frequency	Hz
f_{rs}	Rotating stall frequency	Hz
K	Mean blade thickness	mm
L	Length of the streamline in the vaneless diffuser	m
n	Number of stall cells/number of modes	(–)
N	Rotational speed of impeller	RPM
p	Pressure of the perturbation	Pa
P	Pressure	Pa
P_{atm}	Atmospheric pressure	Pa
P_{BEP}	Total pressure rise of the impeller at best efficiency point	Pa
P_D	Pressure at diffuser inlet	Pa
P_m	Microphone pressure	Pa
$\tilde{P}_m$	Microphone pressure fluctuation	Pa
P_s	Pressure in the suction pipe	Pa
Q	Volume flow rate	$m^3 s^{-1}$
Q_{BEP}	Flow rate at best efficiency point	$m^3 s^{-1}$
Q_d	Design flow rate	$m^3 s^{-1}$
Q_D	Flow rate in the vaneless diffuser	$m^3 s^{-1}$
Q_T	Flow rate from the inlet tank	$m^3 s^{-1}$
Q_{L1}	Leakage flow rate at suction pipe - impeller	$m^3 s^{-1}$
Q_{L2}	Leakage flow rate at impeller – vaneless diffuser	$m^3 s^{-1}$

r	Radial position	mm
r_s	Specific speed	(–)
R	Diffuser radius ratio	(–)
Ra	Roughness	mm
Re	Reynolds number	(–)
S	Area	m^2
S_D	Inlet area of the diaphragm	m^2
t	Time	s
T	Temperature	ºC
u	Velocity of the perturbation	$m\ s^{-1}$
U	Impeller tip speed	$m\ s^{-1}$
V	Absolute velocity	$m\ s^{-1}$
V_r	Radial component of the absolute velocity	$m\ s^{-1}$
V_θ	Tangential component of the absolute velocity	$m\ s^{-1}$
Z	Number of blades	(–)
Greek letters		
α	Flow angle of the streamline in the vaneless diffuser	º
α_c	Critical flow angle for rotating stall	º
β_2	Impeller outlet blade angle	º
ω	Angular velocity	$rad\ s^{-1}$
ω_{imp}	Angular speed of impeller	$rad\ s^{-1}$
ω_r	Theoretical angular velocity of rotating stall	$rad\ s^{-1}$
ω_s	Specific speed of impeller	(–)
ρ	Density	$kg\ m^{-3}$
μ	1/tan α	(–)
θ	Wrap Angle of the streamline	°
λ	Friction factor	(–)
ψ	Scaled amplitude of the pressure fluctuation	(–)
σ	Growth rate of the instability	s^{-1}
ζ	Vorticity	s^{-1}
ε	Loss coefficient	(–)
ε_s	Loss coefficient at stable conditions	(–)
Γ	Circulation	$m^2\ s^{-1}$
Subscripts		

1	Impeller inlet	
2	Impeller outlet	
3	Diffuser inlet	
4	Diffuser outlet	
① – ⑨	Location of the pressure taps from diffuser inlet to outlet	
(1)	First order of the nonlinear terms	
(2)	Second order of the nonlinear terms	
(3)	Third order of the nonlinear terms	
B	Basic	
c	Critical	
imp	Impeller	
real	Real part	
r	Radial direction	
θ	Tangential direction	
z	Z direction	
Superscripts and signs		
–	Complex conjugate or dimensional quantities	
→	Vector	
~	Perturbation quantities	
Δ	Step / Difference	
rot	Curl	
*	Adjoint quantities	

Rotating instability in a radial vaneless diffuser: stability analysis and effect on the performance

Introduction

Turbomachineries are important parts of many devices in modern society, and are widely used in many domains such as water supply, aeronautics, ships, air-conditioning system etc.

The design of turbomachineries can be focused on many aspects. One of them is to increase the operating range of the machine. At partial flow rates, the operating range is limited by the occurrence of unstable phenomena. One of them, which is named rotating stall, has attracted more and more attention in the recent years. Rotating stall has many negative effects, such as noise, vibration, and particularly overall performance reduction. Therefore, the presence of rotating stall is not only threat for the machine itself, but also for the system surrounding it. It is known as a local phenomenon which exists in several passages or components of the machine (example: inducer, impeller or diffuser). The full developed rotating stall often turns into surge, another notable unstable phenomenon which affects the whole system. The present study is focusing on one type of rotating stall which is occurring in radial vaneless diffusers of centrifugal turbomachineries.

In the recent years, one of the test benches of the Laboratoire de Mécanique de Lille was the support of experimental and numerical studies on this topic. In a wide vaneless diffuser, Ljevar et al (2005, 2006a-e and 2007) associated the onset of rotating stall to the two-dimensional core flow instability by using a two dimensional numerical model. This numerical model also has been used to analyze the physical aspects of the instability and to evaluate the effects of geometry parameters. 3D unsteady numerical simulation with a SAS (Scale-Adaptive Simulation) turbulence model was applied on this test bench to study the characteristics of rotating stall in the vaneless diffuser (Pavesi et al, 2011). It has been shown that these kinds of simulation are able to predict reliably the occurrence and characteristics of rotating stall. However, this kind of computations (completely 3D and fully unsteady) is very time consuming. Wuibaut et al (2001, 2002a and b) successfully applied PIV technique to the characterization of velocity distributions in one vaneless diffuser. Using the same technique, Dazin et al (2008 and 2011) identified the characteristics and topology of stall cells in a vaneless diffuser. The results have shown that each cell is composed by two cores with inward and outward radial velocity, and rotating stall is characterized by the development of several rotating cells rotating around the diffuser at a speed which is a fraction of the impeller rotational speed. Further analyses have shown that different stall modes which are characterized by different number of stall cells can exist intermittently at one given flow condition. More detailed of these previous studies are presented in the later literature review.

The aims of the present study are:

(1) To determine if it is possible to use some 2D stability analysis to get a low cost tool which will be able to predict correctly the occurrence, the characteristics and the effects of rotating stall.

(2) To use these tools to try to determine more clearly the cause of this kind of instability.

(3) To conduct some new experiments to have a more complete database to check the validity of the analytical results. The experimental results are also used to discuss the effect of the rotating stall on the diffuser performance.

This work is divided into 5 chapters:

In chapter 1: A review of rotating stall in turbomachineries is presented to show the state of the art of this unsteady phenomenon. Since rotating stall has been observed in different turbomachineries (such as compressors, pumps, etc), their mechanisms and characteristics are summarized. A special focus is made on radial vaneless diffuser rotating stall. Many studies have shown that the behaviors of rotating stall are affected by the geometries of the machine, such as diffuser width, diffuser radius ratio, impeller blade number, etc. The effects of those geometries on rotating stall are specially classified and summarized.

In chapter 2, the experimental test rig and its instrumentation are introduced. The impeller and vaneless diffuser performance are also presented in this chapter. Based on this test rig, the characteristics of rotating stall have been experimentally analyzed, and then the effect of rotating stall on the diffuser performance is investigated.

In chapter 3, a linear stability analysis is presented to characterize rotating stall in the wide vaneless diffuser. The flow in this kind of wide vaneless diffuser is assumed to be two dimensional and axisymmetric, and the fluid is assumed to be incompressible and inviscid. The continuity equation, momentum equations and vorticity equations are written and solved with specific boundary conditions, and the calculated characteristics of rotating stall have been compared to the experiment and the results in literatures. The modes growth rates are used to determine the dominant stall mode. Through the comparisons, the abilities and limits of the linear stability analysis is summarized. At last, a discussion on the cause on of the instability, based on the kinetic energy of the perturbed flow and on the characteristics time associated with the convection of a perturbation are proposed.

In chapter 4, a nonlinear analysis is proposed to take into account the nonlinear combinations which are neglected in the linear analysis. The solutions are extended to the three orders: the first order solutions are the same as the linear ones. The second order solutions have been proposed and verified, and the solvability of the third order results is discussed.

In chapter 5, the conclusions in this study are summarized, and the future works are suggested.

Chapter 1 Literature review

1.1 Introduction

The behavior of work-absorbing turbomachines operating at off design conditions, and especially at partial flow rates, is subject to instability phenomena that could affect their performance and can be dramatic for the machines or their environment. The two most studied instabilities are known as rotating stall and surge, and it is proved in many studies that rotating stall is prior to surge (Senoo and Kinoshita, 1978; Day, 1993 and 1999; Bianchini et al, 2013; Biliotti et al, 2015). Therefore, to improve the safe margin and widen the operating range, rotating stall should be well understood. As rotating stall have been found in many kinds of turbomachineries, the mechanisms, characteristics and general conclusions of rotating stall in each type of turbomachineries are briefly summarized. A special focus is made on the vaneless diffuser rotating stall. The research objective and method of the present study are then introduced.

1.2 Rotating stall in turbomachineries

As a very common unstable phenomenon, rotating stall has been widely studied in many aspects. This phenomenon, which appears at partial flow rate, is characterized by the fact that certain portions of the annulus of blades appear to be stalled while others remain unstalled. In addition, these patterns do not remain fixed to the rotor or the stator, but rotate at a velocity which is a fraction of the rotor velocity. The result is that the blades are exposed to very high, low frequency, aerodynamic load variations. For the stall inception in axial compressors, Mathioudakis and Breugelmans (1985) found that rotating stall is triggered by the interaction between the blade surface boundary layer separation and the blade passage flow. Garnier et al (1990) and Hoying (1995) found that rotating stall is sometimes preceded by periodical pressure waves. The waves evolved into rotating stall smoothly without any sudden change of phase or amplitude. They indicated that the rotating waves and rotating stall are the same phenomenon but at different stage. McDougall et al (1990), Day (1993), Camp and Day (1997) and Inoue et al (2000) concluded that two types of stall inception can exist in low speed axial compressors, which are known as spike and modal oscillation. Spike is a short-length-scale disturbance which is characterized by a sharp peak in the velocity and pressure signal. The appearance of spike stall is related to the local flow separation in the blade row, and occurs when the critical incidence is exceeded. Modal oscillation is a long-length-scale disturbance which grows smoothly into rotating stall. It gives rise to flow separations in a larger number of blade passages, results in broader, slower rotating stall cells, and this cell formation is attributed to the flow separation near the hub side. Day et al (1999) reported that the type of stall inception is strongly depending on the compressor rotational speed. Spike type stall occurs at low rotational speed and it possibly turns into modal oscillation when the rotational speed is increased to a certain value. A typical evolution of short-length-scale stall to long-length-scale wave in axial compressor has been shown in Inoue et al (2000). Numerical simulations also have been applied to study the axial compressor rotating stall in the aspects of their effect and characteristics (Saxer-Felici et al, 1999; Crevel et al, 2014; Dodds and Vahdati, 2015).

In centrifugal turbomachineries, rotating stall also received a great attention. Lennemann and Howard (1970) illustrated the different stall evolutions in shrouded and unshrouded centrifugal impellers. The stall originates from the flow separation generated at the blade suction or pressure side, as shown in Figure 1.1. Arnulfi et al (1996) studied the stall inception at two-stage and four-stage centrifugal blowers. The results showed that the characteristics of rotating stall in the two configurations are almost the same for all flow conditions, and stall inception occurs almost at the same time in all components. It is then concluded that the onset of rotating stall is only depend on the interaction between the impeller and diffuser. Bianchini et al (2015) illustrated the evolution of stall to surge by using a real time analysis. It has been shown that with a further reduction of the flow coefficient, the rotating stall pattern was first replaced by a new and more intense rotating phenomenon, coupled with the onset of e surge conditions. Finally, surge conditions were reached and the pressure fluctuations in the diffuser are replaced by a uniform pressure field, associated with the mass-flow oscillations.

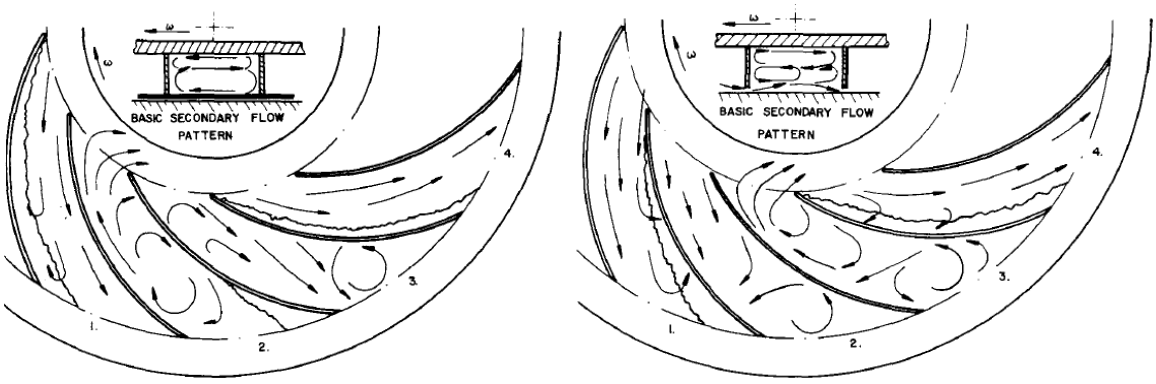

Figure 1.1 Evolutions of rotating stall in shrouded (left) and unshrouded (right) centrifugal impellers (Lennemann and Howard, 1970)

Since the stall inception is characterized by several phenomena, it can be predicted by monitoring the corresponding phenomena. For example, Lawless and Fleeter (1995) studied the spatially coherent pressure waves to warn the arising of instability in a low speed centrifugal compressor. Using some sensitive microphones which have been arranged on the diffuser and around the compressor inlet, and with a Fourier analysis, the experimental results showed that the transition from stable condition to stall condition is a gradual process, and the pressure waves which are used to warn the stall inception is 26 impeller revolutions before a full developed stall. Kang JS and Kang SH (2001) found that the stalling process in a centrifugal compressor is related to the impeller rotational speed, a stall warning is proposed based on the spectrum at impeller frequency. The tested warning time is about 200 impeller revolutions. Another method, which is called traveling wave energy method has also been proved to be a reliable method, and the warning time is 100 impeller revolutions for low impeller speed and 1000 impeller revolutions for high impeller speed.

The occurrence of rotating stall always causes extra loads on the machine, which is a strong threat for the system stability and safety. The pressure fluctuations and vibrations due

to rotating stall have been studied by Lucius and Brenner (2011), Bianchini et al (2013) and Biliotti et al (2015).

1.3 Rotating stall in radial diffusers

In general, the flow coming from centrifugal impeller outlet has a great kinetic energy. Therefore, diffusers are widely used to convert the kinetic energy into pressure, and also help to keep the flow uniform. There are two families of diffusers: vaned diffuser and vaneless diffuser, and many studies have shown that rotating stall can exist in both of them. Actually, it also has been shown that the use of diffusers is always accompanied by rotating stall when the machine is operating at partial flow rates. This was experimentally reported by Abdelhamid and Bertrand (1979), Abidogun and Ahmed (2000), and Biliotti (2013). They found that the flow always became unstable at a certain condition when the machine is operating with a diffuser. However, the mechanisms of rotating stall in these two kinds of diffusers are different, and even only in the vaneless diffuser, different mechanisms which are responsible for the onset of rotating stall can be found.

1.3.1 In vaned diffusers

The mechanism of rotating stall in vaned diffusers is similar to the one that can be found in inducers or impellers, which is associated with local flow separation over the blades or vanes at large positive incidence angles. This kind of rotating stall have been studied by many authors (Tramm and Dean, 1976; Lakshminarayana and Runstedler, 1980; Ötügen et al, 1988; Yoshida et al, 1991; Sinha et al, 2001; Sano et al, 2002). Lejvar (2006) illustrated a typical vaned diffuser rotating stall, as shown in Figure 1.2, where three passages are stalled. The stalled area is called a stall cell, which is characterized by a reduced or no through flow. Rotating stall is formed by several of this kind of stall cell, and propagates in the same direction as the impeller, with a speed which is a fraction of the impeller speed.

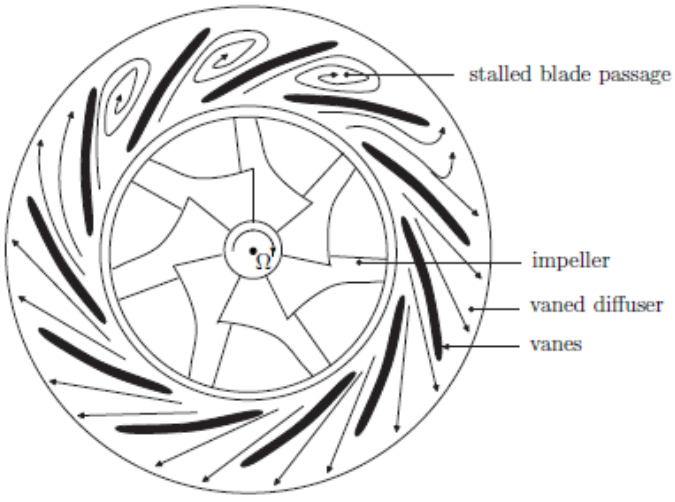

Figure 1.2 Vaned diffuser rotating stall (Lejvar, 2007)

1.3.2 In vaneless diffusers

Rotating stall in the radial vaneless diffuser is somehow different than in other machines due to the non-vane/blade structure, it is not a real stall but a stall-like unstable phenomenon which occurring at partial flow rate. With the similarity to the rotating stall in other machines, it is also named as vaneless diffuser rotating stall. This kind of rotating stall has been extensively studied in many aspects: experimental studies can be found in Abdelhamid and Bertrand (1979), Abdelhamid et al (1979), Abdelhamid (1981), Ligrani et al (1982), Frigne and van den Braembussche (1984), Abidogun and Ahmed (2000), Ferrara et al (2004), Abidogun (2006), Dazin et al (2008 and 2011), and theoretical analyses were presented by Jansen (1964a), Senoo et al (1977), Abdelhamid (1980), Frigne and van den Braembussche (1985), Moore (1989 and 1991), Tsujimoto et al (1996). Several numerical simulations can be found in Ljevar et al (2005, 2006a-e), Ljevar (2007), Pavesi et al (2011).

In Figure 1.3, the PIV results presented by Dazin et al (2011) have clearly shown the topology of rotating stall in a vaneless diffuser. In this case, three stall cells can be identified. Each cell is located near the outlet of the vaneless diffuser, and is composed by two cores with inward and outward radial velocities. These stall cells propagate in the same direction as the impeller rotational direction, and their propagation velocity is proved to be a fraction of the impeller speed (Dazin et al, 2008). This also can be seen from Figure 1.3(b), the stalled regions are characterized by relative negative tangential velocity. In the axial direction, it has been found that the stall cells are developing in the hub-to-shroud direction.

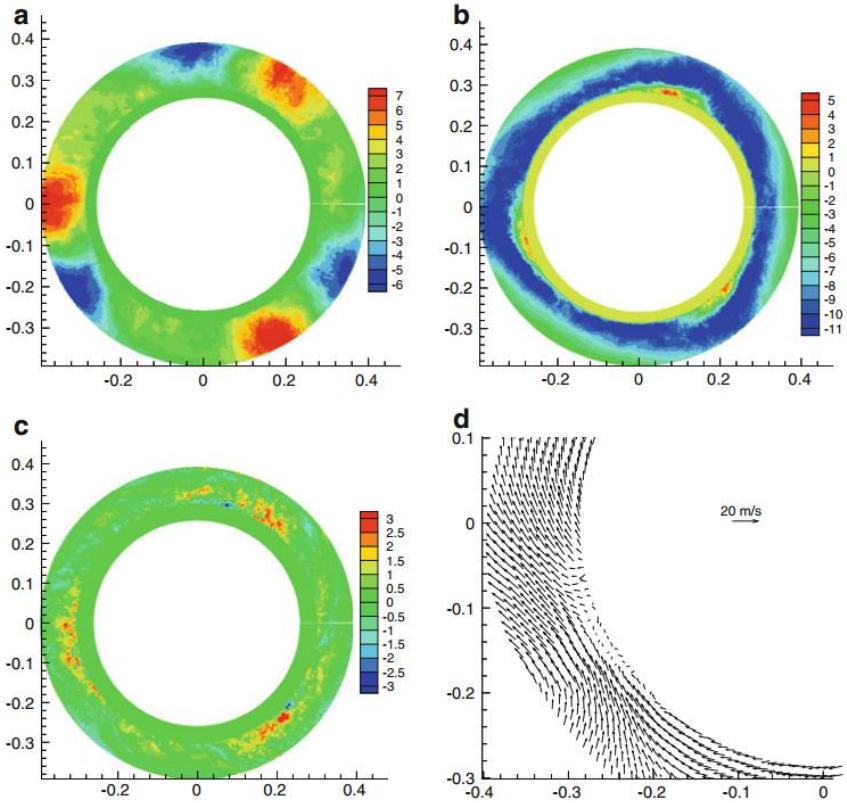

Figure 1.3 Rotating stall in vaneless diffuser: (a) radial, (b) tangential, and (c) axial velocity distributions. (d) velocity vectors (Dazin et al, 2011)

The mechanisms of the vaneless diffuser have been extensively studied, and many studies have revealed that more than one mechanism should responsible for the onset of rotating stall. Abdelhamid and Bertrand (1979) found the measured characteristics of rotating stall in their study are different from the results presented by Jansen (1964a) and Abdelhamid et al (1979) in many aspects, and then they pointed out the possibility of the existence of more than one set of flow conditions which could lead to the occurrence of rotating stall in the vaneless diffuser. The geometrical parameters in these studies are listed as follow:

- Jansen (1964a): $D_4/D_3 = 2.93$, $B_3/D_2 = 0.068$
- Abdelhamid and Bertrand (1979): diffuser 1: $D_4/D_3 = 1.83$, $B_3/D_2 = 0.038 – 0.063$

  diffuser 2: $D_4/D_3 = 1.55$, $B_3/D_2 = 0.038 – 0.063$
- Abdelhamid et al (1979): diffuser 1: $D_4/D_3 = 1.51$, $B_3/D_2 = 0.032$

  diffuser 2: $D_4/D_3 = 1.52$, $B_3/D_2 = 0.065$

The first difference comes from the comparison of non-dimensional rotational speed of the stall patterns. This rotational speed did not change as the flow rate was reduced after the onset of rotating stall in Abdelhamid and Bertrand (1979), but it increased as the flow rate was decreased in Jansen (1964a) and Abdelhamid et al (1979), as shown in Figure 1.4.

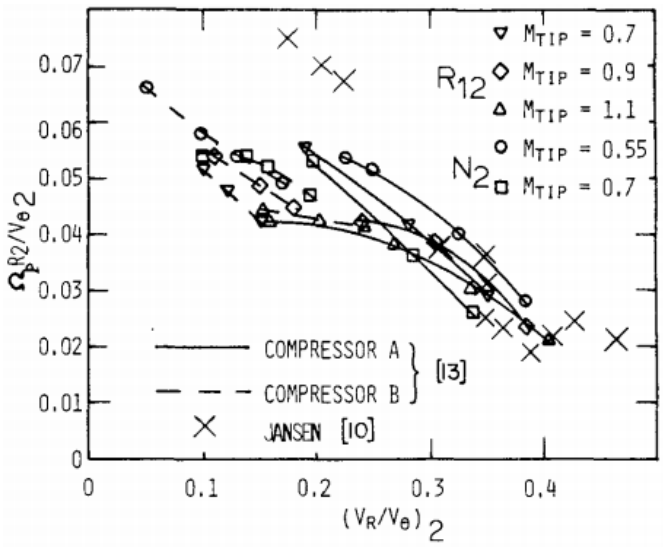

Figure 1.4 Variation of non-dimensional rotational speed with the diffuser inlet flow angle (Jansen, 1964(a), Abdelhamid et al, 1979)

The difference also can be seen in the waveform of the pressure signals at stall condition. The waveform in Abdelhamid and Bertrand (1979) is characterized by a sharp variation while in Abdelhamid et al (1979) the waveform is sinusoidal or almost sinusoidal.

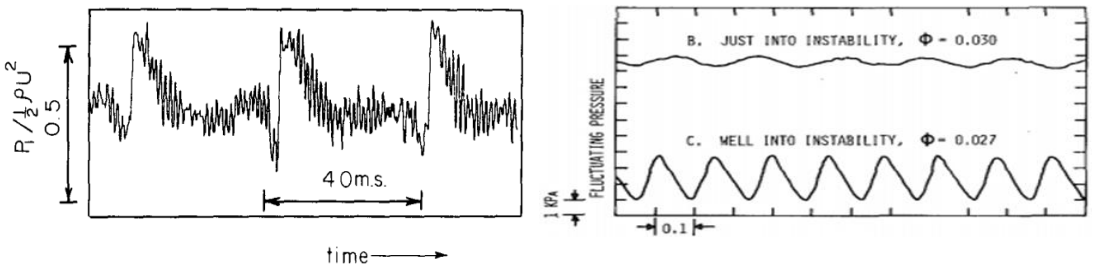

(a) (b)

Figure 1.5 Waveforms of the pressure signals at stall conditions: (a) Abdelhamid and Bertrand, 1979 (b) Abdelhamid et al, 1979

More differences can be found in terms of amplitude of the pressure fluctuation and number of lobes. The amplitude of the pressure fluctuation is 11% (of ρU_2^2), and the number of lobes varies from 1 to 4 in Abdelhamid and Bertrand (1979), while the amplitude is only about 0.4% - 2%, and only one stall pattern with 2 lobes can be obtained in Abdelhamid et al (1979). Although the geometrical parameters are similar in these two studies, but the observed characteristics of rotating stall are clearly different. It is then concluded that more than one set of flow mechanisms could responsible to the occurrence of rotating stall in the vaneless diffuser.

Shin et al (1998) reported two mechanisms responsible for the development of reverse flow which further results in abrupt rotating stall development in a vaneless diffuser. Figure 1.6 gives the phase-averaged radial velocity distribution at the stall inception for two flow rates ($\phi = Q/\pi D_2 B_3 U_2$), the shaded areas represent reverse flow regions. It can be seen that the reverse flow at $\phi = 0.16$ is dominated by the extension of the reentering flow from the diffuser exit, and at $\phi = 0.06$, it is dominated by the growth of the local flow separation zone on the hub and shroud side.

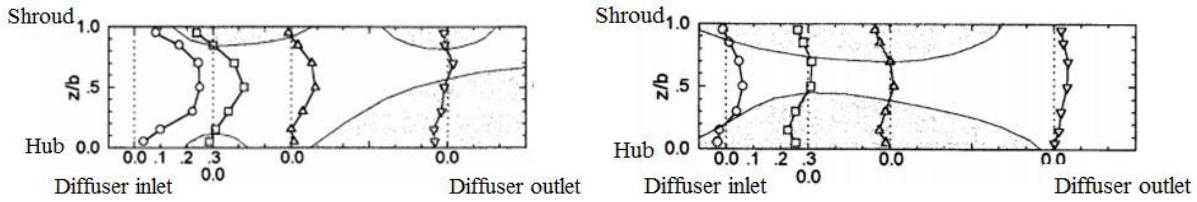

(a) $\phi = 0.16$ (b) $\phi = 0.06$

Figure 1.6 Phase-averaged radial velocity distributions with diffuser radius ratio and axial distance (Shin et al,1998)

Gao et al (2007) summarized the effects of geometries on rotating stall in the vaneless diffuser by wavelet neural networks. The results have shown that the stall behavior in diffusers with large and small width ratio responds differently for variation of one same parameter. For example, the critical flow angle is found to increase with the width ratio in Jansen (1964a), and this result contradicted with Abidogun (2006). This suggests that the stall mechanisms in two kinds of diffuser are possibly different. According to that, depending on the ratio of diffuser width to impeller outlet radius B_3/r_2, Ljevar (2007) proposed two kind of vaneless diffusers geometry: wide vaneless diffuser ($B_3/r_2 > 0.1$) and narrow vaneless diffuser

($B_3/r_2 < 0.1$), as shown in Figure 1.7. The stall mechanisms in two types of diffuser are different due to the different forms of the boundary layers.

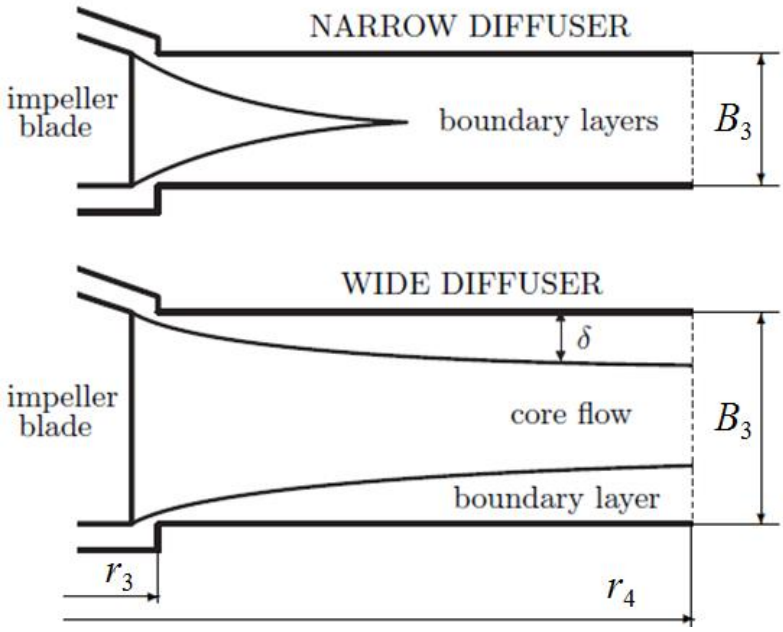

Figure 1.7 Narrow and wide vaneless diffusers (Lejvar, 2007)

(1) In narrow vaneless diffusers, the mechanism of rotating stall is associated with a three dimensional boundary layer instability. From the diffuser inlet, the boundary layers on both walls gradually develop with the increase of radius, then they merged together and interact with the core flow. The interaction between boundary layers and the core flow will leads to unsteady flow (flow separation, reverse flow, reentering flow, etc) in the flow channel. Consequently, rotating stall could occur when those unsteady flow are combined with the rotating system.

(2) In wide vaneless diffusers, it is assumed that the space between two walls is large enough to have a two dimensional core flow which separates the wall boundary layers from each other. In this case, the mechanism of rotating stall is mainly associated with a two dimensional core flow instability, and the effect of boundary layers on the core flow is weak.

However, one can notice that the diffuser radius ratio r_4/r_3 is also important to define the type of diffuser. According to the previous diffuser definition, one can imagine that the boundary layers in a "wide vaneless diffuser" can be in the same situation as in the narrow vaneless diffuser if the diffuser radius ratio is also large enough. Similar considerations have also been reported by Senoo and Kinoshita (1977). They indicated that no reverse flow occurs in a wide vaneless diffuser if the diffuser radius ratio is small enough. Besides, the mass flow rate also strongly affects the development of the boundary layer, the decrease of the mass flow rate results in a smaller diffuser inlet flow angle, and an increase of the length of the streamlines. Consequently, the boundary layer thickness will increase and the flow topology in a wide vaneless diffuser will be similar to the one we have in a narrow vaneless diffuser.

Nevertheless, how to define “narrow” or “wide” vaneless diffuser is not clear even if different diffuser geometries can lead to different instability mechanisms. The main focus of next part will be to introduce these different mechanisms of rotating stall in the two kind of vaneless diffusers.

1.3.2.1 Three dimensional rotating stall

Three dimensional rotating stall in vaneless diffusers, associated with a flow separation or a reverse flow due to the boundary layer instability, have been extensively studied. This kind of diffuser stall has been studied with the help of the boundary layer theory. Jansen (1964a) found that a steady flow may change into rotating stall when the radial velocity component is directed inward along the diffuser side walls. The three-dimensional boundary layer theory used in Jansen (1964b) indicated that the inward flow take place when a three-dimensional boundary layer separation occurs. Therefore, rotating stall will be expected when a three-dimensional flow separation exists in the vaneless diffuser. The criterion to predict the boundary layer separation is given in Figure 1.8. The flow separation (or rotating stall) will be present when the machine is operated in the region on the right of the curves.

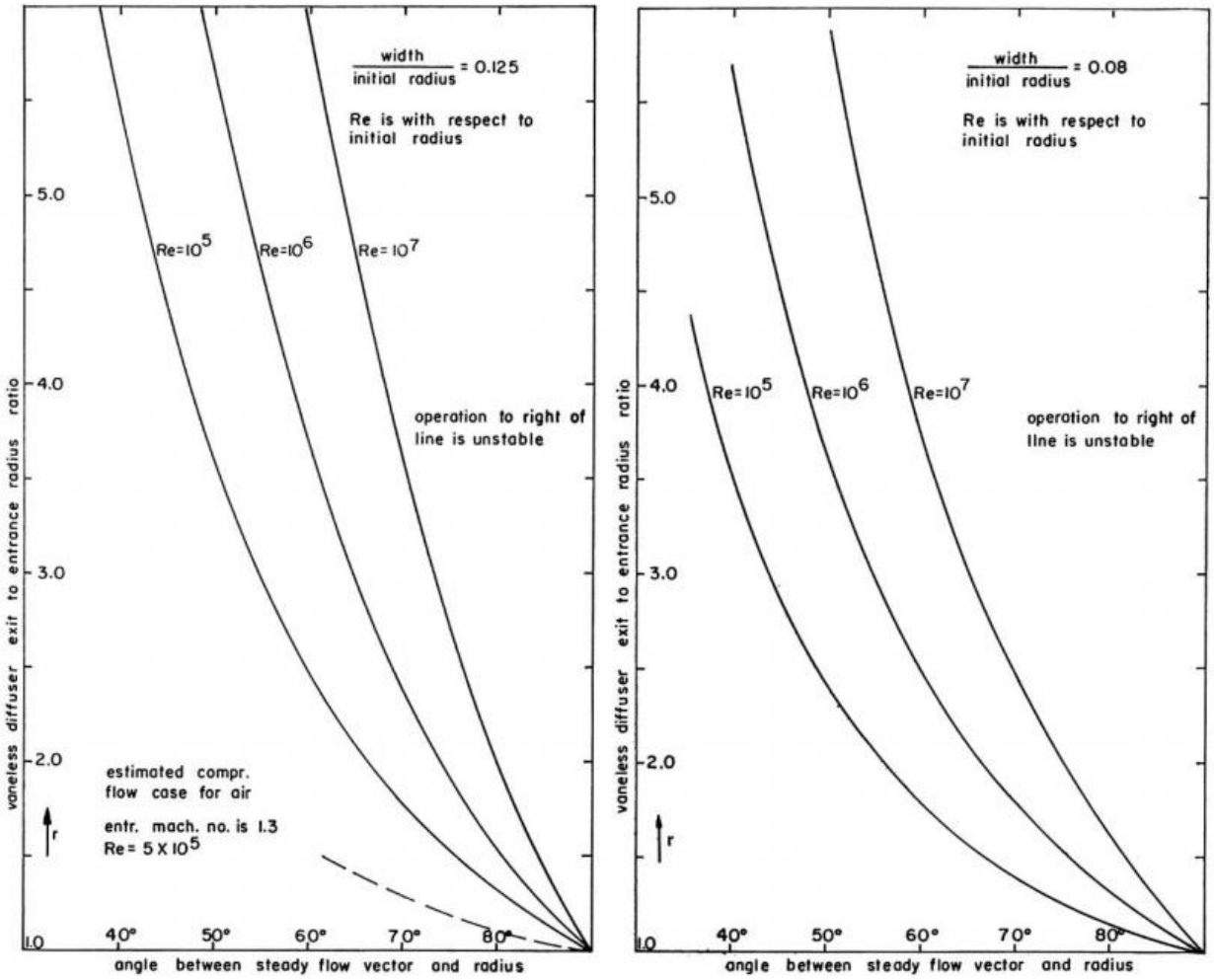

Figure 1.8 Stable operating range of the flow in the vaneless diffuser (Jansen, 1964a)

Using the same boundary layer theory, Dou and Mizuki (1998) indicated that the location of the flow separation varies with different parameters. In Figure 1.9, the value of $\alpha - \gamma_w = 0$ indicates the separation location. It can be seen that with a given diffuser inlet flow angle $\alpha = 30^o$, the flow separation is closer to diffuser inlet with the increase of Reynolds number (Figure 1.9(a)). On the other hand, Figure 1.9(b) shows that the separation is moving to the diffuser inlet with the decreasing flow angle when the Reynolds number is fixed. Therefore, the physical mechanism of the onset of rotating stall is explained as: with the decrease of flow rate, the flow separation or the reverse flow zone moves to the diffuser inlet and interacts with the rotating jet-wake flow pattern discharged from impeller outlet, and rotating stall is then generated. The importance of the interaction between jet-wake pattern and the reverse flow on the diffuser instability also haven been reported by Mizuki et al (1985). Some other studies of the jet-wake pattern can be found in Dean and Senoo (1960), Johnston and Dean (1966) and Cumpsty (1989).

More studies of rotating stall associated with the three-dimensional boundary layer theory can be found in Senoo and Kinoshita (1977), Senoo et al (1977), Frigne and van den Braembussche (1985).

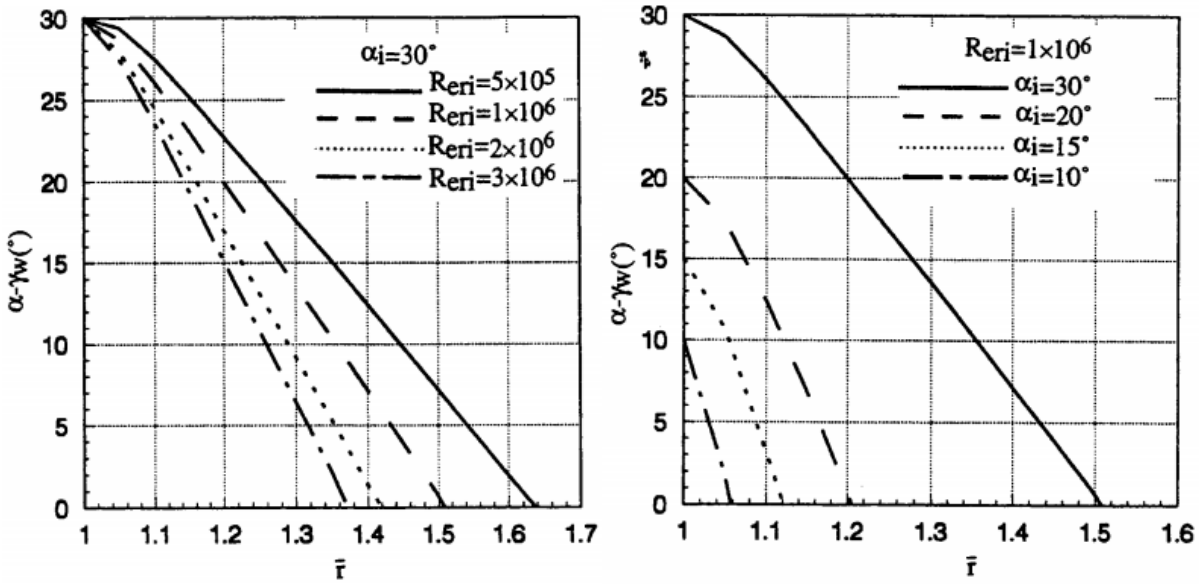

(a) (b)

Figure 1.9 Effects of the diffuser inlet (a) Reynolds number and (b) flow angle on the wall boundary layer flow angle (Dou and Mizuki, 1998)

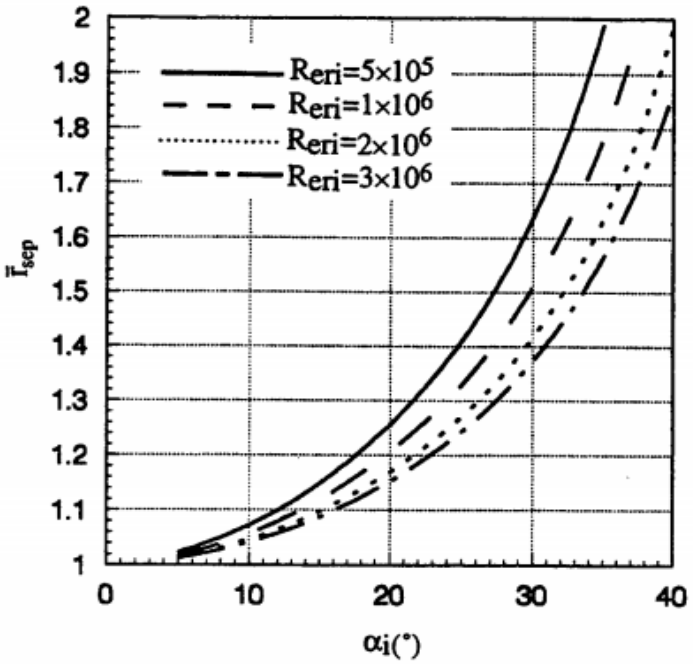

Figure 1.10 Separation locations versus the diffuser inlet flow angle (Dou and Mizuki, 1998)

1.3.2.2 Two dimensional rotating stall

As it has been introduced before, rotating stall in a wide vaneless diffuser is associated with the two dimensional core flow instability which appears when a critical flow angle is reached, and the effect of the boundary is weak and can be neglected. Studies for this kind of rotating stall have been presented by Jansen (1964a), Abdelhamid (1980), Moore (1989 and 1991), Tsujimoto et al (1996), Ljevar et al (2005, 2006a-e and 2007).

Jansen (1964a) has not only indicated that the occurrence of rotating stall is linked with the three dimensional boundary layer separation, but also proposed a two dimensional theoretical model to determine the stability of the two dimensional diffuser core flow. It was assumed that the diffuser flow in the vaneless diffuser is two dimensional, incompressible and inviscid, and the perturbed flow is treated as the superposition of a steady and a perturbed flow. The model is constructed by the continuity and momentum equations, and the solution which expresses the perturbation in periodic waves is given in the following form:

$$\phi = \psi(r)e^{i(\sigma t+\lambda\alpha)} \tag{1.1}$$

where σ is a complex number,

$$\sigma = \sigma_{re} + i\sigma_{im} \tag{1.2}$$

In this analysis, λ represents the number of stall cells, and σ_{re} is the angular velocity of rotating stall. The stability criterion for the two dimensional flow is determined by the sign of σ_{im}, the perturbations grow for $\sigma_{im} < 0$, decay for $\sigma_{im} > 0$, and keep constant for $\sigma_{im} = 0$. That is, the flow turns into unstable regime when $\sigma_{im} < 0$.

With the same assumption of the diffuser flow as Jansen (1964a), Abdelhamid (1980) proposed a theoretical analysis to estimate the effects of relevant parameters on the stability limits. The flow properties were written as a mean flow plus the perturbations,

$$\begin{aligned} V_r &= \bar{V}_r(r,\theta) + u_r(r,\theta,t) \\ V_\theta &= \bar{V}_\theta(r,\theta) + u_\theta(r,\theta,t) \\ p &= \bar{p}(r,\theta) + p(r,\theta,t) \end{aligned} \tag{1.3}$$

The linearized equations were obtained and the perturbations were written in a form similar to the one proposed by Jansen (1964)

$$\begin{aligned} u_r(r,\theta,t) &= u_r(r)e^{i(\omega t+m\theta)} \\ u_\theta(r,\theta,t) &= u_\theta(r)e^{i(\omega t+m\theta)} \\ p(r,\theta,t) &= p(r)e^{i(\omega t+m\theta)} \end{aligned} \tag{1.4}$$

The model was solved with specified boundary conditions. The determination of stable or unstable regimes has been done by introducing a small imaginary part to the quantity $\omega r_2 / \bar{V}_{\theta 2}$. Based on this model, the effects of diffuser radius ratio, diffuser inlet flow angle, frequency of the oscillation, and number of stall cells have been discussed, the general conclusions are

(1) Diffusers with small radius ratio are more stable than the large ones.

(2) The decrease of diffuser inlet flow angle leads to the decrease of diffuser stable margin.

(3) Depending on the boundary conditions, diffuser stable margin responses differently for the increase of number of stall cells.

(4) The coupling between the impeller and the diffuser is important to the generation of self-excited oscillation. The diffuser flow maybe stable with one impeller, but unstable with another even with the same diffuser inlet flow angle.

Tsujimoto et al (1996) presented a two dimensional inviscid flow analysis to study the characteristics of rotating stall in vaneless diffusers. It is assumed that the vorticity is transported on the steady flow which is given by:

$$\begin{aligned} V_r &= \frac{Q}{2\pi r} \\ V_\theta &= \frac{\Gamma}{2\pi r} \end{aligned} \tag{1.5}$$

It is also assumed that the relative flow exits the impeller tangentially to the vanes, then the following condition can be obtained by:

$$\tilde{v}_{\theta 2} = -\tilde{v}_{r2} \cot\beta \tag{1.6}$$

where β is the vane angle.

The linear model is constructed to give the solutions for the disturbance velocity components and the vorticity. In the subsequent simplified case, the boundary conditions of vanishing velocity fluctuation at thediffuser inlet and vanishing pressure fluctuation at the diffuser outlet are applied, that is, for the velocity fluctuations at the diffuser inlet:

$$\tilde{v}_{r2} = \tilde{v}_{\theta 2} = 0 \tag{1.7}$$

and for the pressure fluctuation at diffuser outlet:

$$\tilde{p}_3 = 0 \tag{1.8}$$

It is interesting to note that the above condition (1.6) associated with the impeller parameter is always satisfied by the proposed boundary condition (1.7) regardless the vane angle. Therefore, this simplified analysis is independent on the upstream impeller. A further analysis also showed that the diffuser rotating stall is nearly unaltered even if a more realistic flow taking into account: the impeller is used as an inlet flow condition.

If the diffuser radius ratio and the number of stall cells are given, this analysis is able to calculate the corresponding flow angle and propagation velocity of the stall mode at critical condition, as shown in Figure 1.11, where the flow angle is defined as the angle between the flow path and the tangential direction: $\bar{\alpha} = \arctan(V_r / V_\theta)$

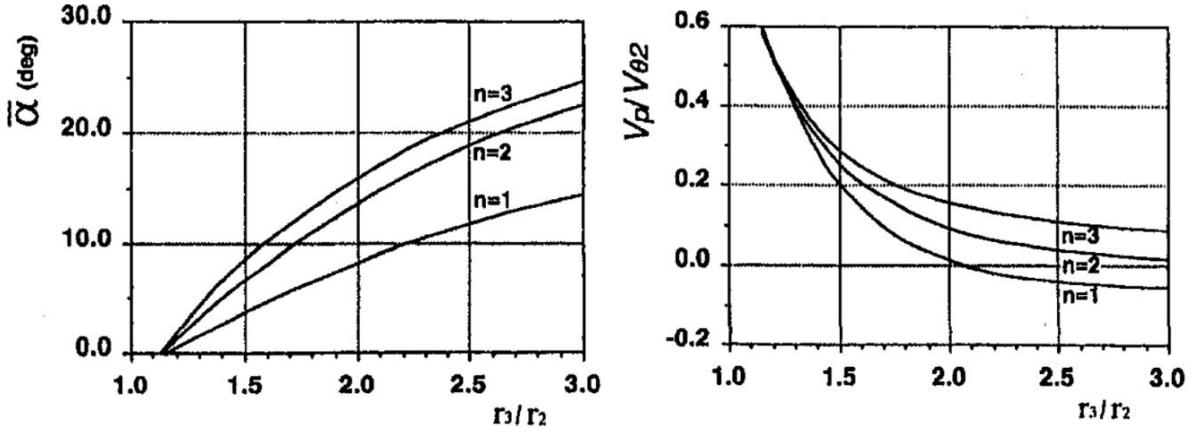

Figure 1.11 The critical flow angle and propagation velocity of rotating stall versus diffuser radius ratio (Tsujimoto et al, 1996)

The general conclusions for this two dimensional analysis are

(1) Rotating stall occurs when the critical flow angle is reached. The critical flow angle and propagation velocity are the functions of the diffuser radius ratio and number of stall cells, and independent on the impeller.

(2) The critical flow angle is larger for larger number of stall cells when the radius ratio is fixed, and is larger for larger radius ratio when the number of stall cells is given.

(3) Smaller propagation velocities are observed for larger radius ratio.

In addition to theoretical analysis, two dimensional rotating stall have also been numerically simulated by Ljevar et al (2005, 2006a-e, and 2007). The studied vaneless diffuser is a typical wide one with a radius ratio equal to 1.52. A laminar incompressible flow model is used, and the jet-wake pattern is prescribed at the diffuser inlet. The transition from stable to unstable conditions is shown in Figure 1.12. It can be seen that at stable condition (α_m = 11º), counter-clockwise vortices alternate near the diffuser outlet, and the number of the vortices equal to the number of the prescribed jet-wake patterns; at the unstable condition (α_m = 3.9º), two dimensional rotating instability which characterized by seven counter-clockwise rotating vortex structures can be identified. It is believed that this two dimensional rotating instability is associated with rotating stall phenomenon since it develops in few impeller revolutions and characterized by rotating cells which propagate with a fraction of impeller speed around the circumference. This transition is obtained by varying the diffuser inlet radial and tangential velocity, that is the inlet flow angle which is known to be the critical parameter for the occurrence of rotating stall. The authors also suggest that the occurrence of the two dimensional rotating instability is due to the interaction between the diffuser inlet jet-wake pattern and the alternating flow pattern near the diffuser outlet. When the flow angle is large, the jet-wake pattern is more radial toward to the alternating flow pattern, and they gear perfectly into each other. With the decrease of the flow rate, the jet-wake pattern becomes more circumferential. Once it is circumferential enough to pass underneath the alternating flow instead of interacting with it, rotating instability starts to occur. The small and weak vortices merge into larger ones, and finally several cells are formed and equally distributed around the diffuse space.

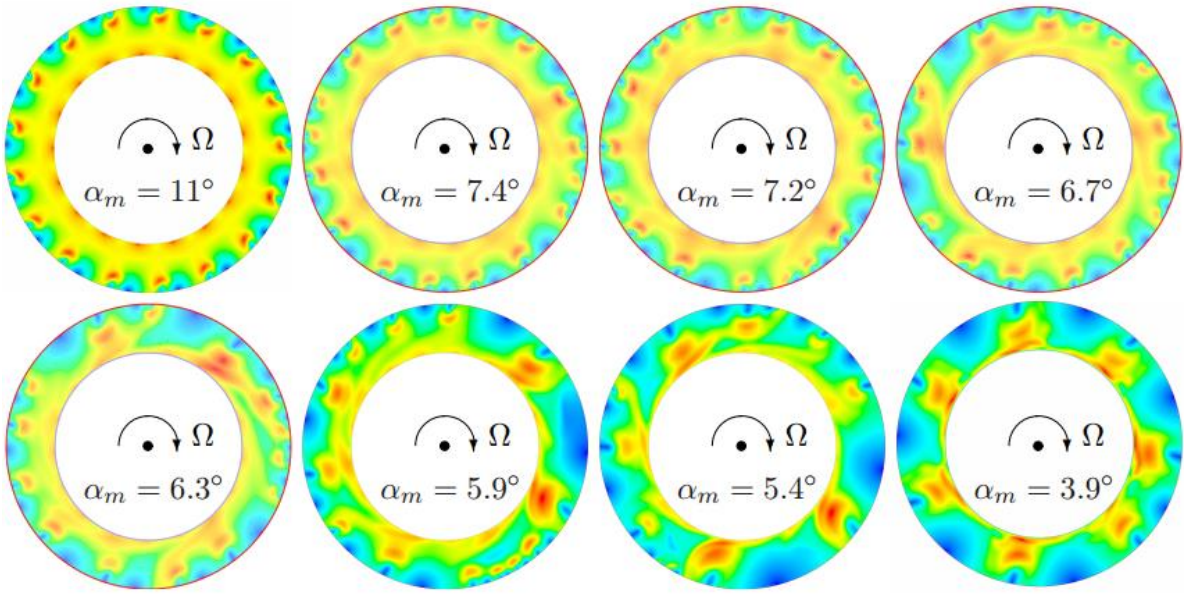

Figure 1.12 Contours of velocity magnitude from stable to unstable conditions (Ljevar, 2007)

This two dimensional simulation has also been applied to study the influence of the geometrical parameters, that is the effect of diffuser radius ratio, diffuser width ratio and the impeller on the stall characteristics.

1.3.3 Effects of the geometry

Rotating stall is characterized by several characteristics (number of cells, critical condition, propagation velocity, etc) which can depend on the geometrical parameters of the machine. Therefore, the study of the effects of these parameters on the instability behavior can help to predict the stall at the design phase, this is particular important for industrial application. The main studies that have been conducted on these subjects are summarized as follows.

Diffuser radius ratio: Senoo and Kinoshita (1977) reported that the decrease of radius ratio helps to suppress the reverse flow which is expected at the rear part of a wide vaneless diffuser, and leads to a decrease of the critical inlet flow angle. Abdelhamid (1981) found that the rotational speed of stall cells varied inversely with the diffuser radius ratio, and that critical flow angle of stall inception increased with the diffuser radius ratio, but the slope the critical angle evolution with the radius ratio decreased significantly when the radius ratio larger than 1.75. Tsurusaki et al (1986), and Tsurusaki and Mori (1988) experimentally observed that the critical flow angle of rotating stall decreases with the decrease of the diffuser radius ratio. Theoretically, Tsujimoto et al (1996) have shown that the critical flow angle increases with the increase of the diffuser radius ratio in a linear stability analysis. The effect of the diffusion ratio reported by Ferrara et al (2004), is actually the effect of diffuser radius raio. It has been found that the radius ratio has a great influence on both of the stall inception and the stall pattern. In a shorter vaneless diffuser, a smaller stall inception flow angle is expected but the stall pattern becomes more complex. The numerical study presented by Lejvar (2007) agrees that the critical angle of rotating stall decreases with decreasing diffuser radius ratio, and the number of cells and their propagation velocity decrease with the increase of the diffuser radius ratio. The propagation velocity of stall cells seems only affected by the size of the diffuser space. She has shown that a larger diffuser radius ratio leads to cells which are far from the diffuser inlet and which are consequently propagating at a lower velocity. As a conclusion, if other geometrical parameters remain unchanged, smaller radius ratio diffusers are more stable than larger ones. The reasons are twofold: on the one hand, the boundary layer get easily fully developed in a diffuser with a large radius ratio. This leads to a flow separation or a reverse flow which is one of the rotating stall triggers; on the other hand, the stable margin for a small radius ratio is wider because the critical condition will be reached at a much smaller flow angle. However, it should be noticed that the decrease of radius ratio also leads to a performance reduction. Therefore, the balance between the stability and performance should be carefully considered.

Diffuser width ratio: Jansen (1964a) reported that a decrease of the diffuser width ratio will increase the flow angle at diffuser inlet, and thus keep the flow angle away from the critical stall condition: the operating range of the system is then increased. Senoo and Kinoshita (1977), and Ligrani et al (1982) also gave similar conclusions about the effect of diffuser width ration on the flow stability. Tsurusaki et al (1986) experimentally plotted the critical flow angle of rotating versus 4 diffuser width ratios, the results have shown that the critical flow angle increase with the increase of diffuser width ratio. Ötügen et al (1988) stated that the onset of rotating stall is delayed with the decreased diffuser width ratio due to the

critical flow angle of rotating stall decreases with the decreased diffuser width ratio. Moore (1991) also observed that narrow diffusers are more stable than wide ones, because the boundary layer displacement makes the flow in narrow diffusers more convergent than in wide ones. Ferrara et al (2004) agree that the diffuser width strongly influence the critical flow rate of stall inception, but seems to not influence very much the stall evolution. Ishida et al (2005) found that the operation range of narrow diffuser is larger than wide ones: the unstable flow range of the test blower was reduced about 45% by implementing a narrower diffuser. Lejvar (2007) explained why the stability range is improved in narrow diffuser: first, a narrow diffuser gives additional friction forces which make the flow structure more stable; second, a narrow diffuser increases the radial velocity component. Consequently, the flow angle becomes larger. However, Abidogun (2006) reported that the critical flow rate of rotating stall in a vaneless diffuser increases with the decrease of diffuser width ratio, which is inconsistent with previous studies. He also indicated that the frequency of rotating stall is not affected by the diffuser width ratio, but increases with the increase of diffuser radius ratio: this result is also opposite to what was observed by Ljevar (2007). Nevertheless, it seems that most of the studies agree to say that small diffuser width ratio helps to widen the stable operating range of the system, but leads also to a performance drop.

Impeller: Zhu and Sjolander (1987) studied the effects of the impeller geometry on the diffuser performance. The main geometrical parameters for the impeller are: blades number, inlet blade angle and outlet blade angle. The results showed that the diffuser performance was not affected by the impeller geometries. Ötügen et al (1988) also reported that the behavior of rotating stall is not affected by the impeller tip speed. Tsurusaki and Ichihara (1988), Tsujimoto et al (1996) have concluded that the vaneless diffuser rotating stall is nearly unaffected by the upstream impeller. Lejvar (2007) indicated that the scaled propagation velocity of cells is independent on the impeller speed and the number of blades, but that the number of stall cells and the critical flow angle vary with the number of impeller blades. As a conclusion, it seems that the diffuser rotating instability is not affected too much by the impeller, diffuser rotating stall is more likely linked to the nature of the diffuser itself.

Diffusion shape: Zhu and Sjolander (1987) studied two kind of diffusers with divergent or convergent structures. The results showed that the convergent diffuser can help to stabilize the inner flow because it helps to reduce or eliminate the reverse flow which is the main cause of rotating stall in a wide vaneless diffuser. However, the penalty of the convergence diffuser is the performance reduction. Therefore, it is suggested to select an optimised wall convergence angle to satisfy both the performance and the stability requirements.

Clearance between impeller and diffuser : Yoshida et al (1991) performed an experiment to study rotating stall by changing the clearance between impeller and diffuser. It has been found that the clearance has a great effect on rotating stall. With the decrease of the clearance, rotating stall became weakened and exists in a narrower flow range, which means the flow is more stable with a small clearance. Sano et al (2002) simulated the effect of the clearance between the vaned diffuser and the impeller on the stall inception. The results also showed that a small clearance leads to an increase of the safe margin.

Mach number: Senoo and Kinoshita (1977) indicated that the critical flow angle is affected by the diffuser inlet Mach number, and that the influence is strong for diffuser with large width ratio. The critical flow angle increases with the increase of Mach number because a larger Mach number results in a greater density and consequently a decrease of the flow angle. The influence is strong for large width ratio diffuser because the reverse flow occurs at larger radius and the effect of Mach number is magnified. The results presented by Ferrara et al (2004) also showed that the Mach number strongly influence stall inception flow rate, but does not influence too much on the stall evolution.

1.3.4 Pressure losses in vaneless diffusers

Senoo and Kinoshita (1978) reported that the pressure losses in a vaneless diffuser consist of exit losses and wall friction losses. For diffusers with small radius ratio, the pressure loss is mainly contributed by the exit loss, and it is increased with the increase of flow rate. On the other hand, the pressure losses in large radius ratio vaneless diffuser are mainly coming from the wall friction losses and it increases with the decrease of flow rate.

Dou (1989) concluded that the losses in the vaneless diffuser consist of: mixing losses at the diffuser inlet, the divergence losses caused by the pressure gradient, secondary flow losses, and wall friction losses. The mixing losses are caused by internal friction resulting from the shear stress distribution over the whole inlet cross section of the diffuser passage, and it is mainly focused in the region: $D/D_2 = 1.00 \sim 1.06$. The divergence loss is significant when the flow angle is large, because the boundary layer easily separates from the diffuser wall due to the large divergence of the passage. On the other hand, the secondary flow loss becomes important when the flow angle is small, because the flow tends to be unstable because of the large curvature of the streamline and the reverse flow. Based on a semi-empirical method, it is found that i/ the total energy loss is strongly depending on the flow angle and the diffuser width ratio, ii/ the friction losses are important in the front part of the diffuser and are small in the rear part.

Dou (1991) added that the friction losses are significant when the flow path is long in the vaneless diffuser, consequently, the friction losses should depend on the diffuser width ratio, diffuser radius ratio, diffuser inlet flow angle and Reynolds number. Therefore, this analysis discussed the diffuser losses together with the diffuser width ratio and the inlet flow angle. The results cited from Den (1960), Johnston and Dean (1966) and Dou (1989) are plotted in Figure 1.13.

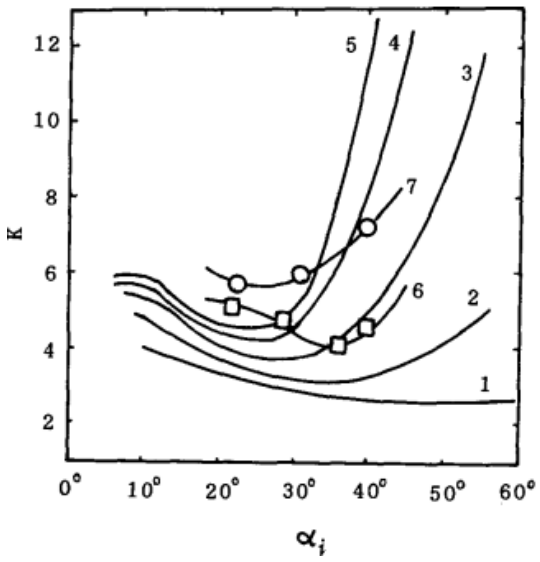

References	number	B	r_e / r_i	β_{2A}
Den(1960)	1 2 3 4 5	0.0187 0.0312 0.0468 0.0608 0.0697	1.583	45°
Johnston & Dean (1966)	6	0.0313	1.80	90°
Dou(1989)	7	0.0601	1.45	40°

Figure 1.13 Variation of *K* (ratio between total losses and wall friction losses) versus the mean inlet flow angle (Dou, 1991)

where *B* is the diffuser width ratio, r_o/r_i is the diffuser radius ratio, and β_{2A} is the blade angle at the impeller outlet. *K* represents the ratio between total losses and wall friction losses. The minimum value of *K* in each case represents the point for which the wall friction losses are the largest portion of the total losses, and one flow angle α_i is corresponding to the minimum *K* value. When the flow angle is smaller than this value of α_i, the contribution of the secondary flow losses increases; when the flow angle is larger than α_i, the diffusion losses increase. It can be seen that the friction losses are the primary source of losses in diffuser with small width ratio, and that the other losses are small. On the other hand, the friction losses become a small part of the total losses in large width ratio diffusers especially when the flow angle is large.

More studies about the losses analysis in the vaneless diffuser can be found in Johnston and Dean (1966) which is focused on the mixing losses and the wall friction losses, in Senoo et al (1977) which is focused on the wall friction losses coefficient. Nevertheless, no study can be found on the effect of rotating stall on the diffuser performance and losses.

1.3.5 Control methods for diffuser rotating stall

Many studies have reported that one of the stall mechanisms is linked with the flow angle. The flow angle in the diffusers is determined by the radial and tangential velocity components. Therefore, based on this observation, experimental control techniques have been carried out to delay the arising of rotating stall.

Tsurusaki and Kinoshita (2001) used jet flows to control rotating stall in a parallel vaneless diffuser, as shown in Figure 1.14. The rotatable jet nozzles were inserted in the vaneless diffuser. By rotating the nozzle, rotating stall was suppressed when the jet direction was opposite to the impeller tangential velocity, and was amplified when set the jet was in the same direction as the impeller tangential velocity. This is because when the mass flow rate

remains unchanged, the flow angle will be increased (decreased) by the decrease (increase) of the tangential velocity.

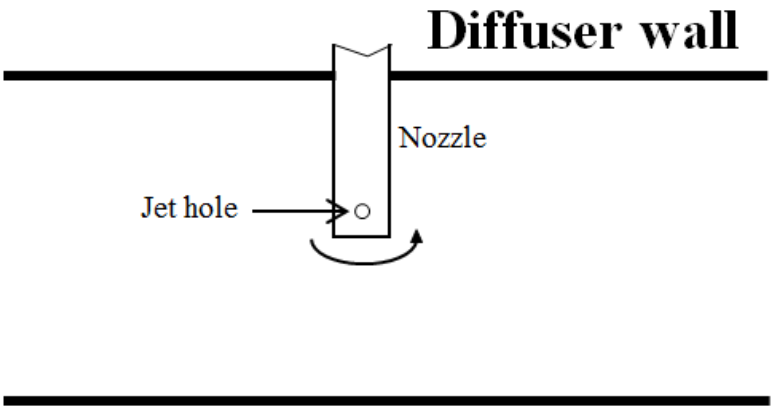

Figure 1.14 Stall control by jet flow (Tsurusaki and Kinoshita, 2001)

Kurakawa et al (2000) used radial grooves to suppress rotating stall in a vaneless diffuser, as shown in Figure 1.15. The grooves are characterized by different length, width and depth. The results showed that all grooves are helpful to suppress rotating stall because the radial grooves increased the radial velocity at the diffuser inlet due to the groove reverse flow, and also decreased the tangential velocity due to the mixing between the main flow and the groove flow. Both of these two effects lead to an increase of the diffuser inlet flow angle. Consequently, the onset of rotating stall is delayed.

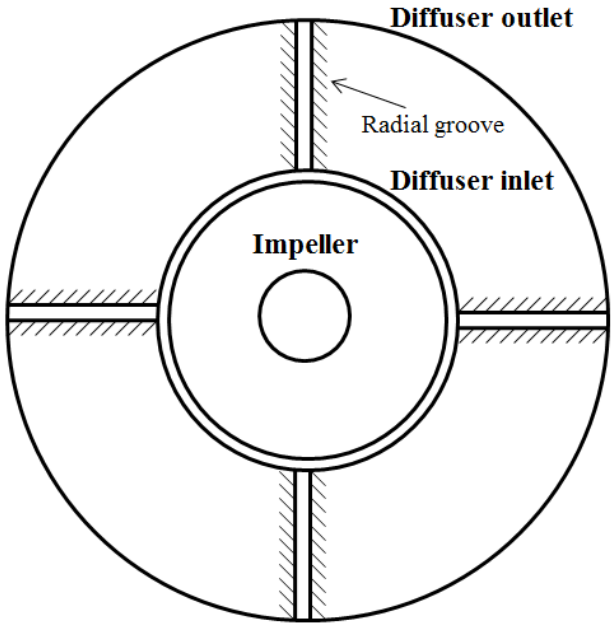

Figure 1.15 Radial grooves used for stall suppression (Kurokawa et al, 2000)

With the similar consideration, Saha et al (2001) applied J-groove structure to suppress rotating stall in a vaned diffuser of radial impeller, as shown in Figure 1.16. The tested results showed that rotating stall can be entirely suppressed by J-grooves, and any increase of the

length, number, width and depth of the grooves will increase the suppression effect, but with an increase of performance loss.

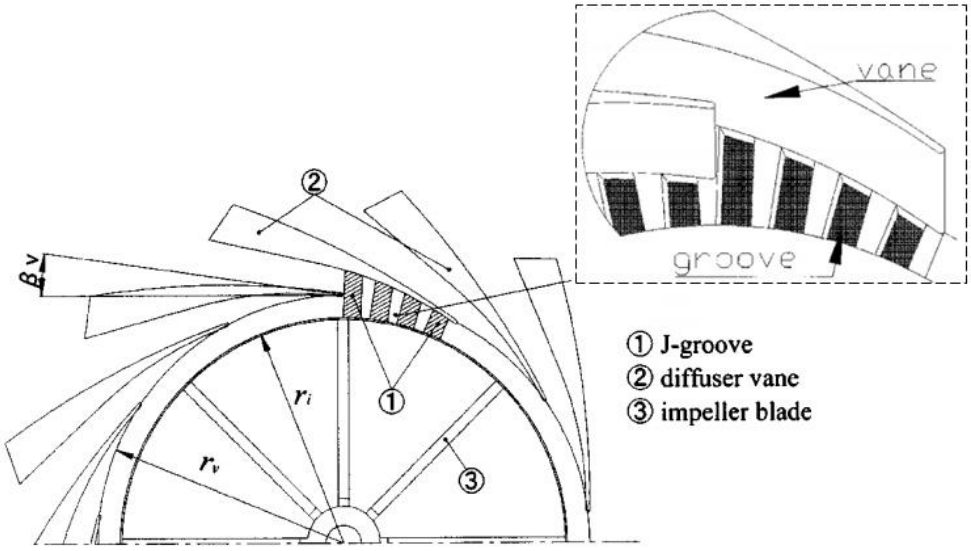

Figure 1.16 J-groove structure (Saha et al, 2001)

On the other hand, as it has been introduced, one of the mechanisms of rotating stall is associated with the boundary layer instability and suppressing this instability could be an effective way to control rotating stall. Ishida et al (2001) studied the effect of the hub side wall roughness on rotating stall in the vaneless diffuser. The results showed that the increase of wall roughness decreased the skewed angle of the three dimensional boundary layer, consequently the boundary layer separation is suppressed, and the onset of rotating stall was delayed with only a small performance reduction (less than 1%). Ahmed (2008) also used the surface roughness to delay rotating stall in a radial diffuser. The results showed that the onset of rotating stall was delayed to a lower flow rate by applying a rough surface. However, the balance between flow stability and system performance should be considered.

1.4 Research object and method

Rotating stall has been widely studied in many aspects as listed above (mechanisms, characteristics, influences, controlling, etc), The present work is focusing on wide vaneless diffuser for which rotating stall is due to a core flow instability. It aims at evaluating the ability of some theoretical approaches to predict correctly the arising and characteristics of rotating stall in a given vaneless diffuser. Some methods based on linear stability analysis, liked the most recent ones proposed by Tsujimoto et al (1996) exist in literature. Nevertheless, in this study, the estimated characteristics of rotating stall are limited to the critical conditions. Besides, many studies have shown that several unstable modes can coexist in a vaneless diffuser at a given operating range. The interactions between these modes are ignored by a linear stability analysis. At last, if many existing studies are concerning the losses and performance of a vaneless diffuser, nothing can be found on the effect of rotating stall on the diffuser losses. Based on these reviews the objectives of the present work are the following:

(1) Extend the linear stability to developed stall conditions.

(2) Extend the study to (weakly) non-linear stability analysis

(3) Conduct new experiments to validate the stability analysis and study the effect of rotating stall on the performance of the diffuser.

Chapter 2 Experimental study

2.1 Introduction

In this chapter, the experimental test rig used in the present study is introduced. This test rig, working with air, was first designed by Morel (1993), and has been used for many studies with the same impeller but with different stators, as shown in Figure 2.1. For example, numerical studies presented by Lejvar (2007), Pavesi et al (2011), experimental studies presented by Wuibaut (2001, 2002a and b), Cavazzini (2007), and Dazin et al (2008, 2011).

Based on this test rig, an experimental study of rotating stall in the vaneless diffuser is presented in this chapter. Using the signal phase difference analysis, the propagation velocity of rotating stall and their number of stall cells are obtained by two microphones on the diffuser upper wall. After the determination of the characteristics of rotating stall, the impeller and diffuser performance are calculated based on some static pressure measurements. Then, an analysis is provided to estimate the effect of rotating stall on the diffuser performance. It is usually admitted that rotating stall has negative effect on the overall performance, but the interest in the present study is focused on the diffuser performance only. With the decreasing flow rate (from stable conditions to unstable conditions), the performance and pressure fluctuations in the vaneless diffuser are measured, and the effect of rotating stall on the diffuser performance is estimated through a comparison of the losses at stable and stall conditions. The influence of rotating stall is then discussed.

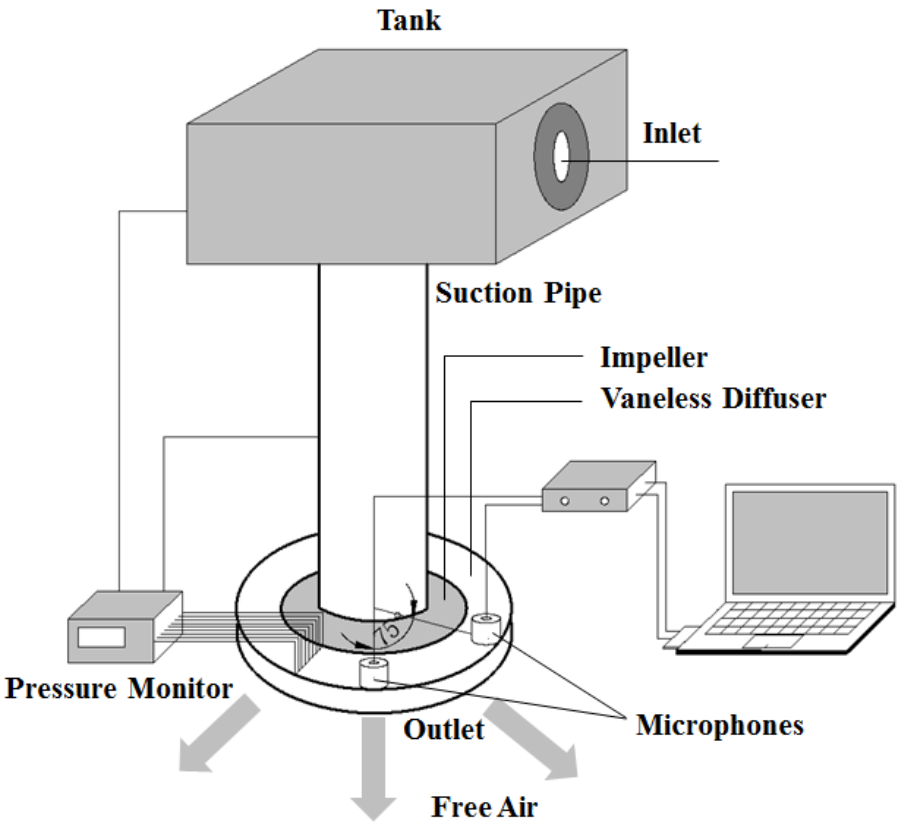

Figure 2.1 Experimental test rig

2.2 Experimental test rig

The sketch of the test bench is shown in Figure 2.1, the configuration used in the present study consists of the so-called “SHF” (Société Hydrotechnique de France) radial impeller coupled with a wide vaneless diffuser downstream of the impeller. It has to be noted that the outlet of the diffuser is at free air to assure an axisymmetric boundary condition at diffuser outlet.The diameter of the suction pipe is D_S = 290 mm, and a tank is placed upstream of this pipe. The tank is equipped with a set of changeable diaphragms which are used to adjust the flow rate. The bottom of the tank is equipped with a honeycomb flow straightener to stabilize the air coming from the tank inlet, and then the stabilized flow will enter into the suction pipe, as shown in Figure 2.2.

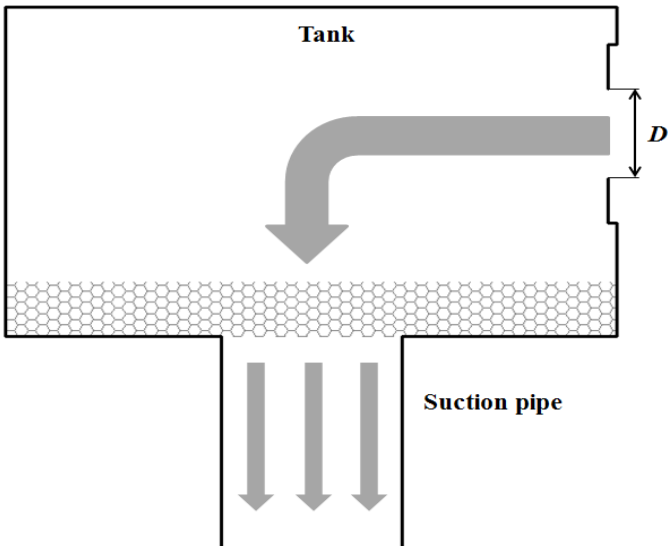

Figure 2.2 Inner structure of the tank

2.2.1 SHF radial impeller

Figure 2.3 SHF radial impeller

The specific speed ω_s and radius r_s of the SHF radial impeller are:

$$\omega_s = \omega_{imp} \frac{Q_{BEP}^{0.5}}{(\Delta P_{BEP} / \rho)^{0.75}} = 0.577$$

$$r_s = r_2 \frac{(\Delta P_{BEP} / \rho)^{0.75}}{Q_{BEP}^{0.5}} = 2.43$$

with

ω_{imp} – Angular speed of the impeller

r_2 – Impeller outlet radius

ρ – Density of the fluid

ΔP_{BEP} – Total pressure rise of the impeller at best efficiency point

Q_{BEP} – The volume flow rate at best efficiency point

Some geometric details are given in Table 2.1. The impeller is driven by a motor, and the rotational speed is measured by a Brüel & Kjaer Type 4913 transducer which is coupled with a photoelectric cell.

Table 2.1 Impeller geometries

r_1	Inlet diameter	141.1 mm
r_2	Outlet diameter	256.6 mm
B_2	Impeller outlet width	38.5 mm
Z	Number of blades	7
β_2	Impeller outlet blade angle	22.5°
K	Mean blade thickness	9 mm
Q_d	Design flow rate(1200rpm)	0.236 m^3/s
$R_e=\rho V D_H/\mu_1$	Reynolds number(in Q_d)	9.08×10^4

2.2.2 Vaneless diffuser

The vaneless diffuser is connected to the impeller outlet and is composed of two parallel walls, as shown in Figure 2.4. The outlet of the vaneless diffuser is connected with the atmosphere. The main geometrical characteristics of the vaneless diffuser are given in Table 2.2.

Table 2.2 Geometries of the vaneless diffuser

r_3	Inlet diameter	257.1 mm
r_4	Outlet diameter	390 mm
B_3	Diffuser width	38.5 mm

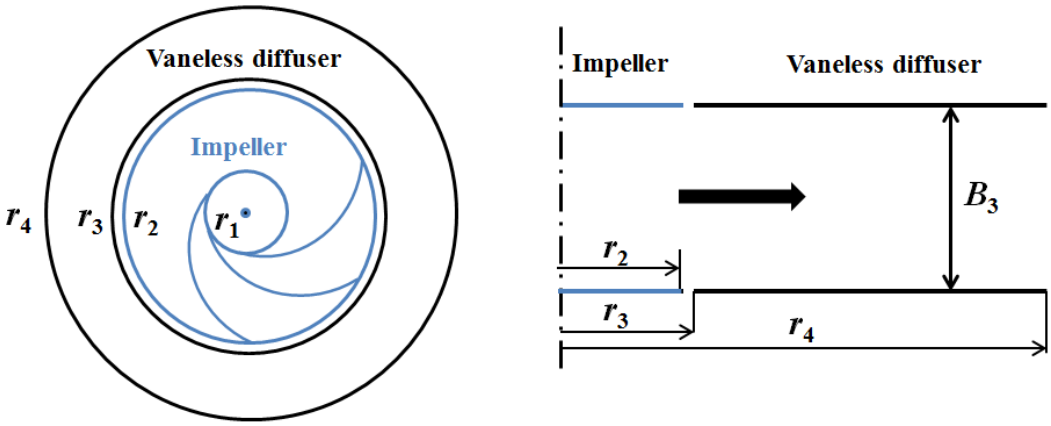

Figure 2.4 Vaneless diffuser

2.2.3 Brüel & Kjaer condenser microphones

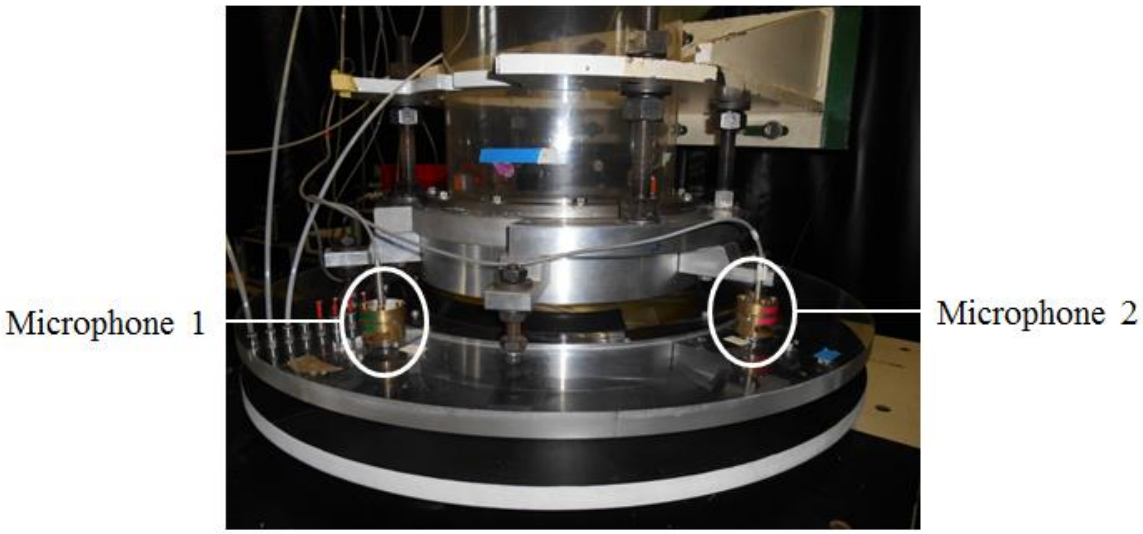

Figure 2.5 Brüel & Kjaer condenser microphone (Type 4135)

Vaneless diffuser rotating stall is characterized by periodical pressure fluctuations. Therefore, two Brüel & Kjaer condenser microphones (Type 4135) are used to capture the unsteady pressure fluctuations. They are placed on the diffuser upper wall at the same radius (r = 320 mm) but with an angle difference of $\Delta\theta$ =75°. The spectrum analysis is processed by LMS. Test Xpress. The acquisition time and sampling frequency are 600 seconds and 4096Hz, respectively.

2.3 Impeller and diffuser performance

2.3.1 Pressure measurements

To determine the effect of rotating stall, the measurements of the impeller and the vaneless diffuser performances are performed. For the impeller, the static pressure variation between the suction pipe (P_s) and impeller outlet are measured to determine the performance. The pressure of the suction pipe is averaged by 4 positions, as shown in Figure 2.6.

$$P_S = \frac{P_{S1} + P_{S2} + P_{S3} + P_{S4}}{4} \tag{2.1}$$

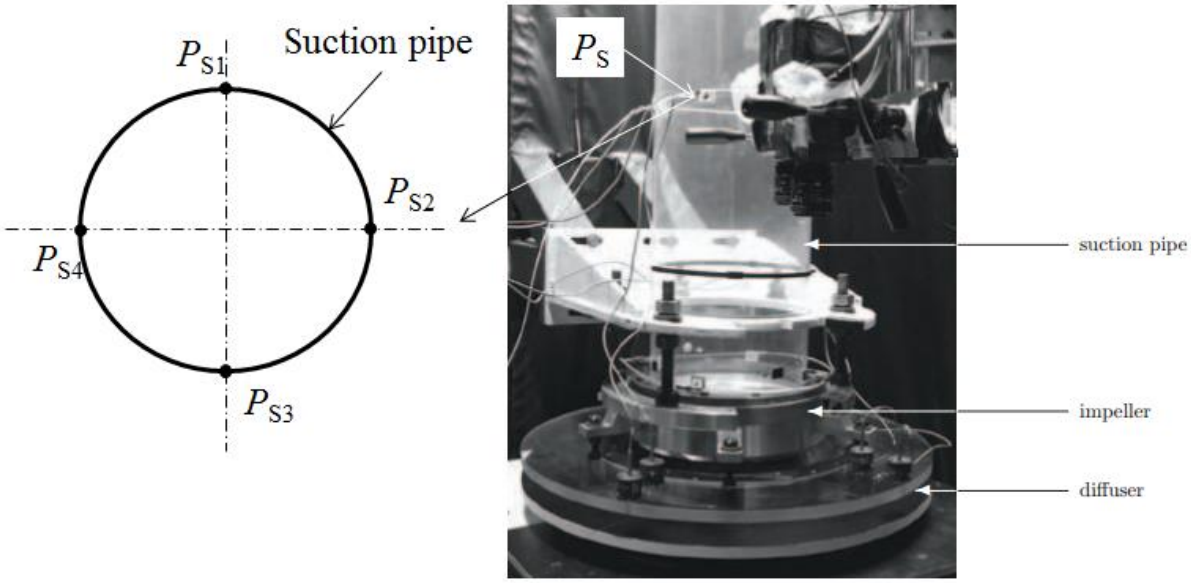

Figure 2.6 Pressure measurement in suction pipe

Because of the clearance between the impeller outlet and diffuser inlet is small enough (= 0.5 mm), the diffuser inlet pressure ($P_{①}$) is used to represent the static pressure at impeller outlet, then the impeller static pressure rise is defined as follows:

$$\Delta P_I = \frac{P_{①} - P_S}{\frac{1}{2}\rho U_2^2} \tag{2.2}$$

where U_2 is the impeller tip speed.

The diffuser inlet pressure recovery is measured with the help of the pressure taps on the diffuser upper wall. 9 pressure taps are mounted in one radial line (Figure 2.7), and are equally spaced from diffuser inlet to outlet, the radii are given in Table 2.3.

Table 2.3 The radii of 9 pressure taps

Location	①	②	③	④	⑤	⑥	⑦	⑧	⑨
Radius (mm)	264	279	294	309	324	339	354	369	384

then the diffuser static pressure variation is defined as

$$\Delta P_D = \frac{P_{⑨} - P_{①}}{\frac{1}{2}\rho U_2^2} \tag{2.3}$$

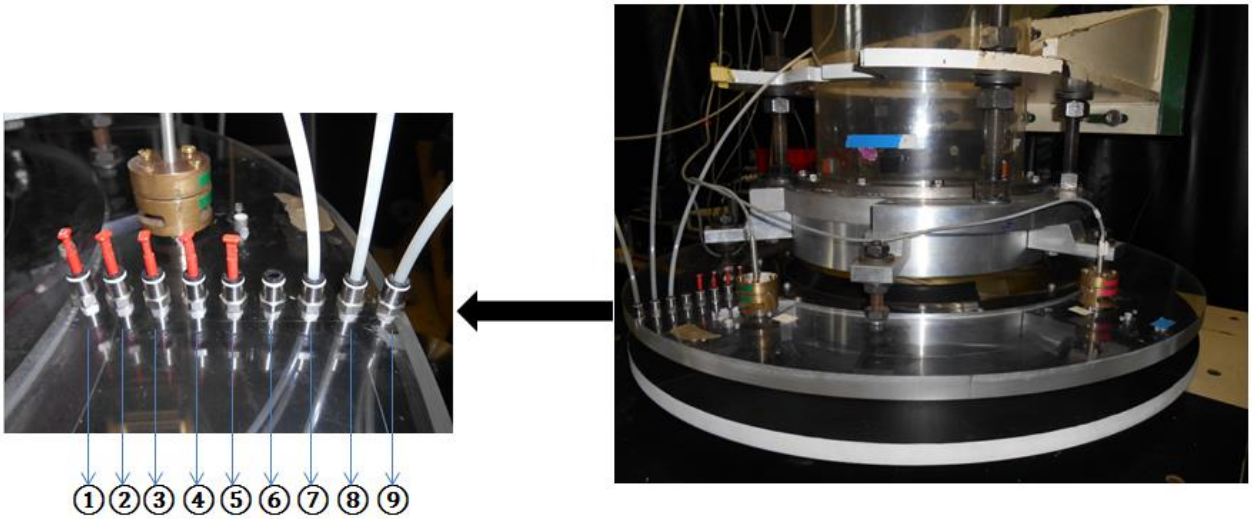

Figure 2.7 Pressure taps on the diffuser

The above static pressure measurements are realized by a Sélecteur BEXHILL, connected with a YEW digital manometer (Type 2654), the accuracy is 0 ± 0.1 mmH_2O. The atmospheric pressure is given by a mercury manometer which ranging from 580 mmHg to 810 mmHg, and the accuracy is ± 0.1 mmHg. The apparatus are shown in Figure 2.8. To calibrate the pressure, the local temperature and humidity are obtained by a thermo-hygrometer – DOSTMANN T870, and the parameters are given in Table 2.4.

Table 2.4 Technical data of the thermo-hygrometer – DOSTMANN T870

	Humidity	Temperature
Range	0% – 98% Hr	–200 ºC – +800 ºC
Precision	± 0.1 Hr	± 0.1 ºC for – +100 ºC – +200 ºC, ± 0.2 ºC for other range
Resolution	0.1 Hr	0.1 ºC

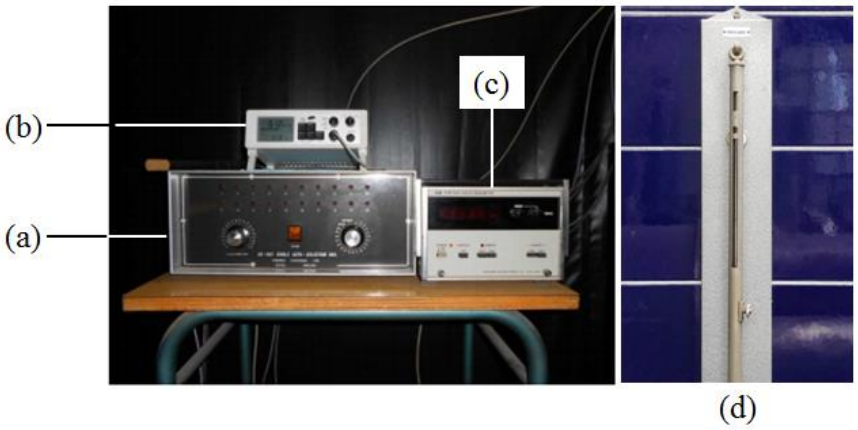

Figure 2.8 (a) The Sélecteur BEXHILL: 20 pneumatic channels. (b) Thermo – hygrometer: DOSTMANN T870. (c) YEW digital manometer (Type 2654). (d) Mercury manometer

2.3.2 Flow rate calibration

To obtain the impeller and vaneless diffuser performance curves, the flow rates need to be determined with calibrations. In the experiment system, two clearances exist between: (1) the suction pipe and the impeller; (2) the vaneless diffuser and the impeller. Consequently, in addition to the main flow from the tank inlet, there are two leakage flows in the two gaps, as shown in Figure 2.9. For the impeller performance, the flow rate Q is

$$Q = Q_T + Q_{L1} \tag{2.4}$$

where Q_T is the flow rate from the tank, and Q_{L1} represents the first leakage between the suction pipe and the impeller.

The second leakage flow Q_{L2} could be positive or negative depending on the diffuser inner relative pressure:

$$Q_D = Q + Q_{L2} \text{ if } P_D < P_{atm} \tag{2.5}$$

$$Q_D = Q - Q_{L2} \text{ if } P_D > P_{atm} \tag{2.6}$$

The detail flow rate estimations have been presented in a previous experimental study presented by Cherdieu (2013), and will be briefly reminded in this section.

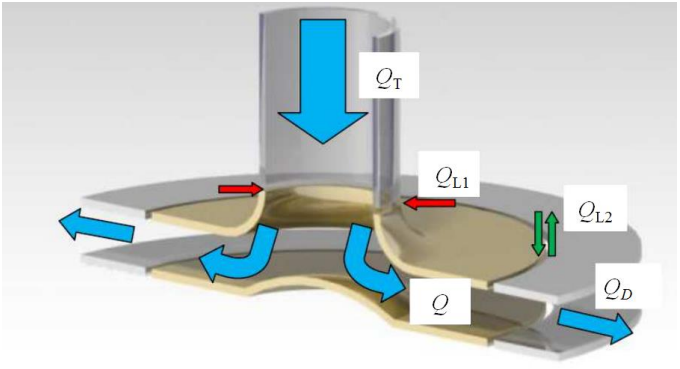

Figure 2.9 Leakage flow in the system

2.3.2.1 Flow rate from the tank Q_T

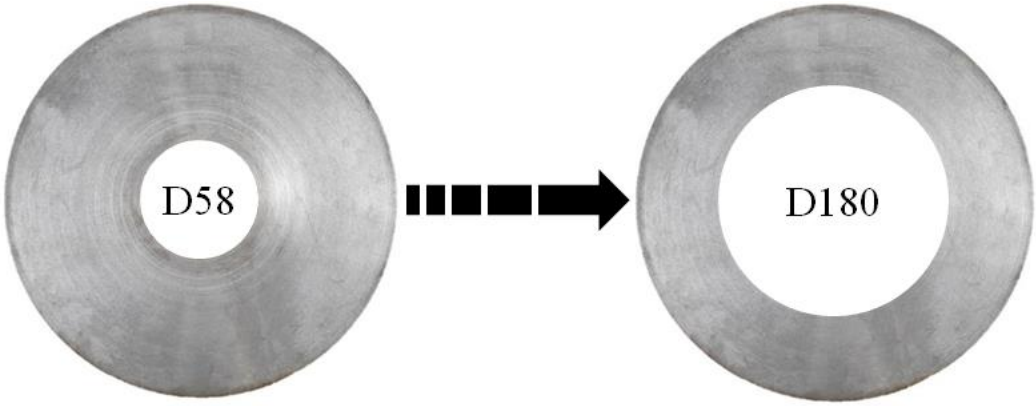

Figure 2.10 Diaphragm on the inlet tank

The flow from the tank inlet is the main part of the total flow rate, it is limited by the inner diameter of the selected diaphragm (Figure 2.10). This flow rate can be estimated by the following expression,

$$Q_T = \alpha_1 S_D \sqrt{\frac{2|\Delta P_T|}{\rho}} \tag{2.7}$$

where

– α_1 is the flow rate coefficient which is given by Figure 2.11.

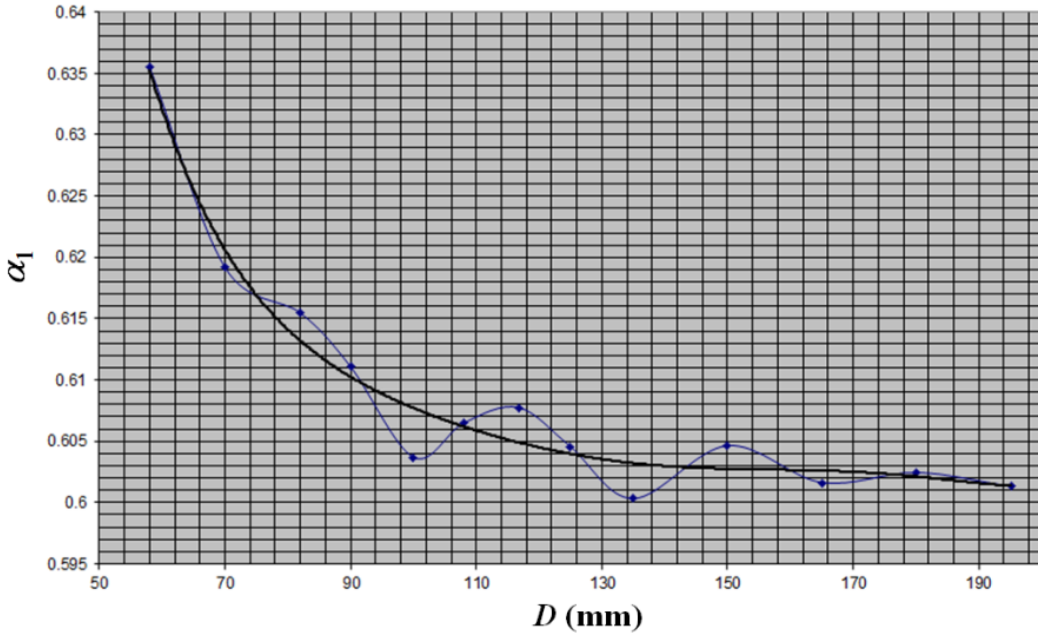

Figure 2.11 Flow rate coefficient versus the inner diameter of the diaphragm

– S_D is the inlet area of the selected diaphragm (m^2): $S_D = \frac{\pi D^2}{4}$

– ΔP_T is the relative static pressure difference between the upstream and downstream of the diaphragm (Pa).

– ρ is the density (kg/m^3), and is calibrated by the following expression

$$\rho = 0.003485 \frac{(P_T - \frac{3}{8} P_{VT})}{T + 273.15} \tag{2.8}$$

– P_T is the absolute pressure at the tank inlet (Pa).

– T is the temperature (℃).

– P_{VT} is the partial pressure of the water vapor in the tank (Pa):

$$P_{VT} = \frac{P_{VE} P_T}{P_E} \tag{2.9}$$

– P_E is the external pressure (Pa), and equal to the atmosphere pressure: $P_E = P_{atm}$

– P_{VE} is the external partial pressure of the water vapor (Pa):

$$P_{VE} = \frac{Hr}{100} P_{VSE} \tag{2.10}$$

– P_{VSE} is the external saturated water vapor pressure (Pa):

$$P_{VSE} = e^{\frac{17.438T}{(T+273.15)-33.37}+6.415} \tag{2.11}$$

– H_r is the humidity, which is measured by the thermo-hygrometer – DOSTMANN T870.

The above quantities are shown in Figure 2.12,

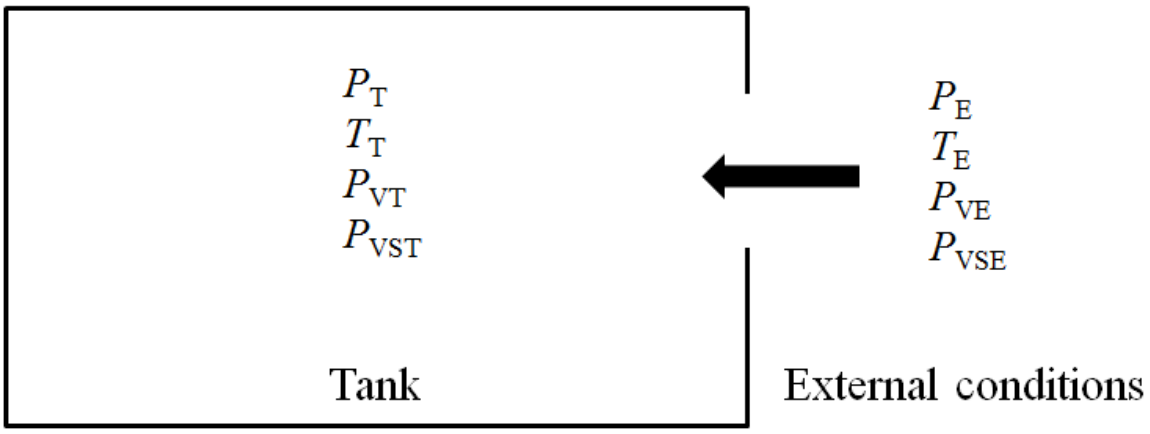

Figure 2.12 Local quantities in the tank and atmosphere

2.3.2.2 Leakage flow Q_{L1}

At the gap between the suction pipe and the impeller, the inner pressure of the suction pipe is lower than the atmosphere, and the external air will be sucked into the pipe. This leakage flow can be estimated by

$$Q_{L1} = 5.449 \times 10^{-3} \sqrt{\frac{|\Delta P_S|}{202\rho}} \tag{2.12}$$

– ΔP_S is the relative static pressure difference between the suction pipe and the atmosphere pressure (Pa): $\Delta P_S = P_S - P_{atm}$, P_S is given in (2.1).

2.3.2.3 Leakage flow Q_{L2}

It should be noticed that the joint shapes between the impeller and diffuser at upper and lower side are different, as shown in Figure 2.13. Therefore, the leakage flows at upper and lower side are calculated in different ways,

$$Q_{L2} = Q_{L2U} + Q_{L2L} \tag{2.13}$$

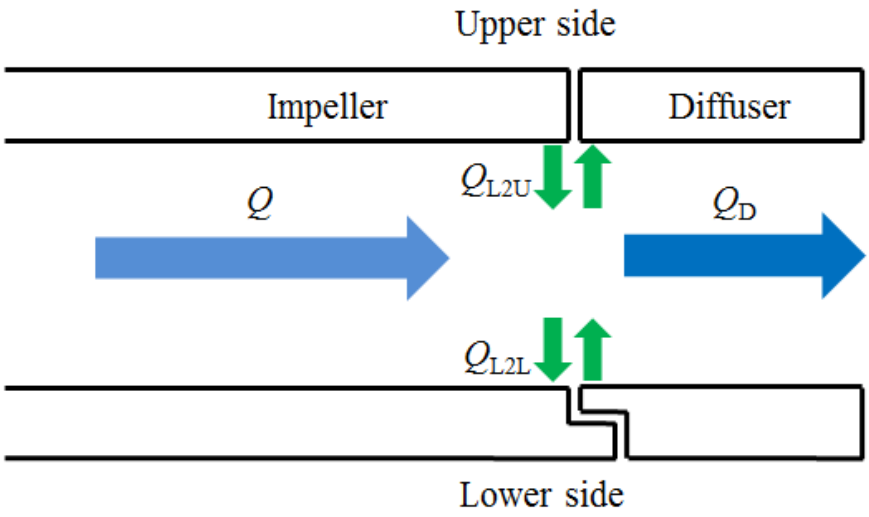

Figure 2.13 The joint shapes between impeller and diffuser at upper and lower side

More detailed about calculations of Q_{L2U} and Q_{L2L} are given in Appendix A. As a result, the performances of the machine and of the vaneless diffuser expressed in terms of static pressure rise are plotted in Figure 2.14. The discussion of the effect of rotating stall, based on these performance curves, will be presented in the later part.

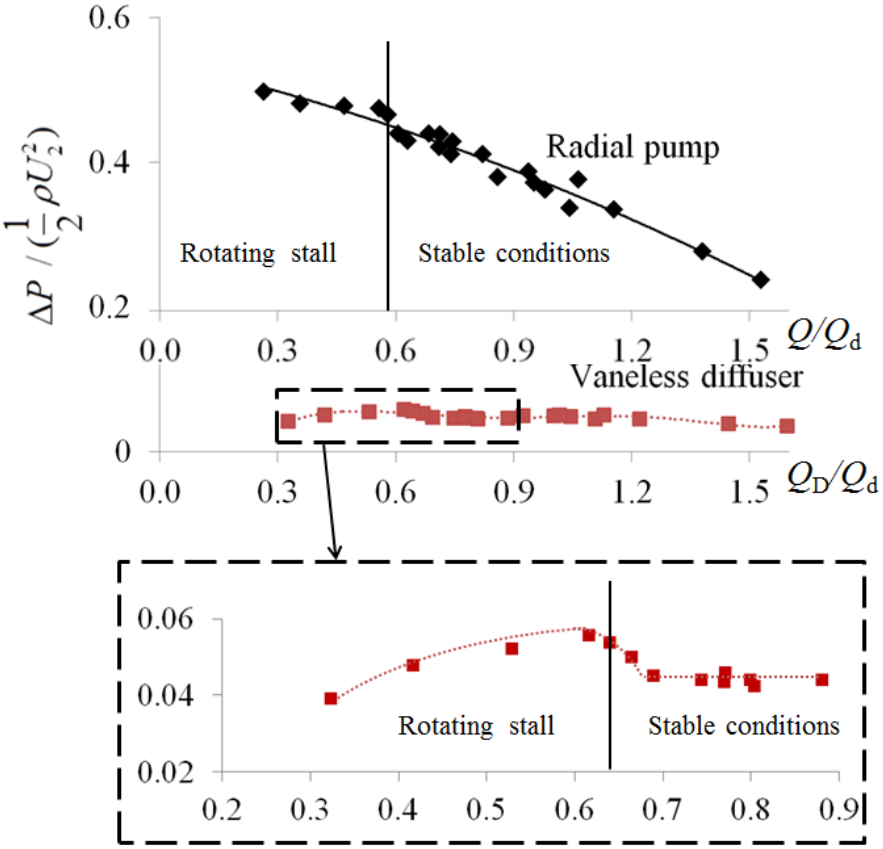

Figure 2.14 Pump and diffuser performance curves (Static pressure rise, the x-axis for the pump and diffuser performance is respectively the impeller flow rate Q and the diffuser flow rate Q_D)

2.4 Vaneless diffuser rotating stall

As it has been reported (for example Abdelhamid and Bertrand, 1979; Abidogun and Ahmed, 2000), rotating stall always occurs within the vaneless diffuser when critical flow conditions are reached. Generally, this critical condition of rotating stall is represented by the critical flow angle in the vaneless diffuser, and the critical flow angle is linked with the flow rate. Therefore, vaneless diffuser rotating stall is triggered by the gradual decrease of the flow rate in present experiment. The flow rate is reduced from large flow rates to low flow rates, which represents stable conditions to unstable conditions. 22 flow rates (Q/Q_d = 1.53 → 0.26) were tested for two rotating speeds: 1200 RPM and 1800 RPM.

2.4.1 Spectrum analysis

The pressure fluctuations are obtained by the two Brüel & Kjaer condenser microphones Type 4135 (see chapter 2.2.3). With the help of spectrum analysis, it is possible to detect the occurrence of rotating stall in the vaneless diffuser and to analyze its characteristics. The spectra for flow rates varying from Q/Q_d = 0.74 down to 0.26 are summarized in Figure 2.15 (For more details, see Appendix B), where ψ was defined as:

$$\psi = \frac{P_m}{\rho U_2^2} \tag{2.14}$$

In which P_m is the microphone pressure signal,

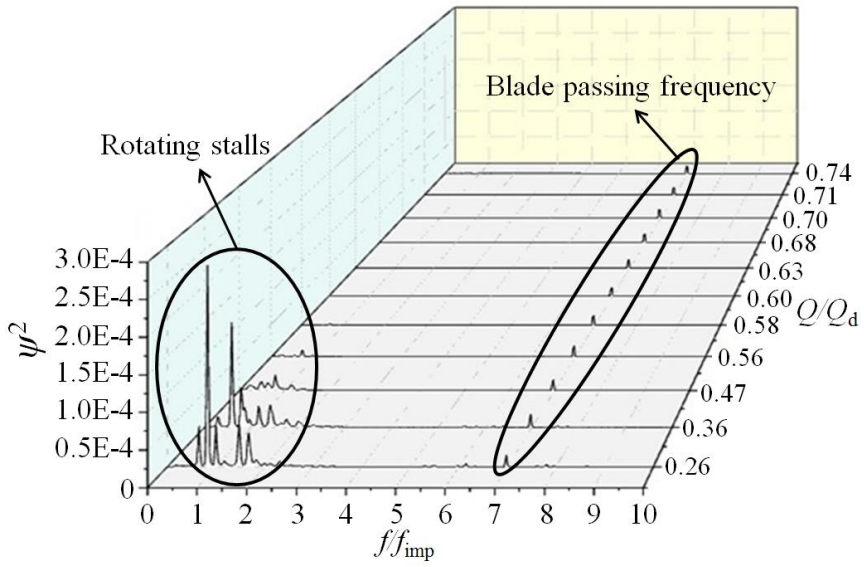

(a) 1200 RPM

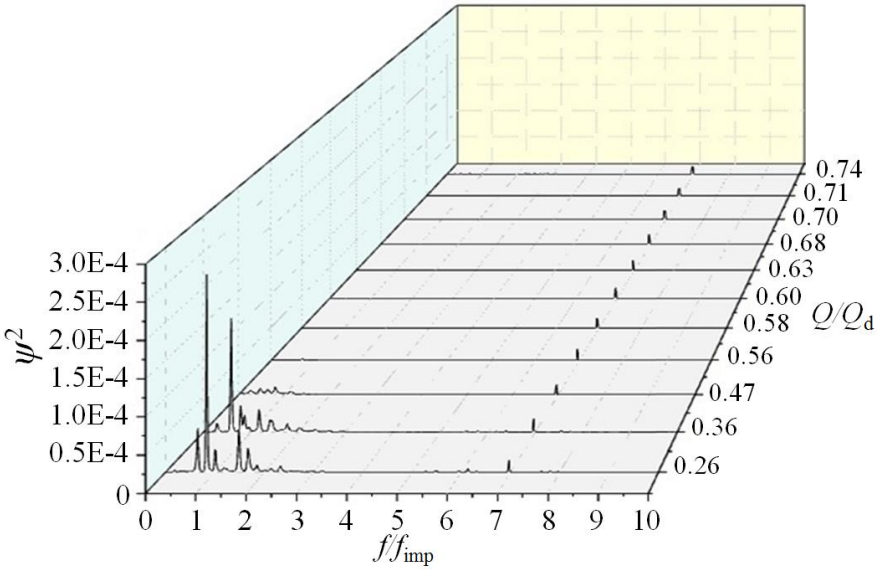

(b) 1800 RPM

Figure 2.15 Cross-power spectra at two impeller angular velocities

It can be seen that the spectra for two rotation speed are similar at all non-dimensional flow rates, and several tendencies can be drawn as follows:

(1) At large flow rate, the highest pressure fluctuation appears at BPF (blade passing frequency), and no other strong fluctuations can be identified.

(2) With the decrease of the flow rate, several low frequency peaks arise and dominate the spectrum. These peaks are generated by the instabilities, and will be classified in the later spectrum analysis.

(3) The instability occurs at the same flow rate regardless the impeller speed. This clearly shows that the occurrence of rotating stall is independent on the impeller speed.

The spectrum at design flow rate Q/Q_d = 1.0 is given in Figure 2.16(a) to represent the typical spectrum at stable conditions (Q/Q_d > 0.6). Contrary to Figure 2.15, the spectrum amplitude is plotted in a long scale. As already pointed out, it is clear that the dominant frequency is the blade passing frequency.

According to the spectrum analysis, rotating stall was identified at the five partial flow rates investigated experimentally: Q/Q_d = 0.26, 0.36, 0.47, 0.56, 0.58, and cannot be observed when the flow rate is higher than 0.6. The spectra of the five flow rates with rotating stall are given in Figure 2.16 (b), (c), (d), (e) and (f) to show the typical spectrum at unstable condition. At Q/Q_d = 0.47, 0.56 and 0.58, the blade passing frequency is still the dominant frequency, but the low frequency peaks amplitude is of the same order of magnitude. At Q/Q_d = 0.26 and 0.36, the dominant frequency is no longer the blade passing frequency. It can be seen that the amplitude of the low frequency peaks become stronger than the blade passing frequency and dominate the spectra.

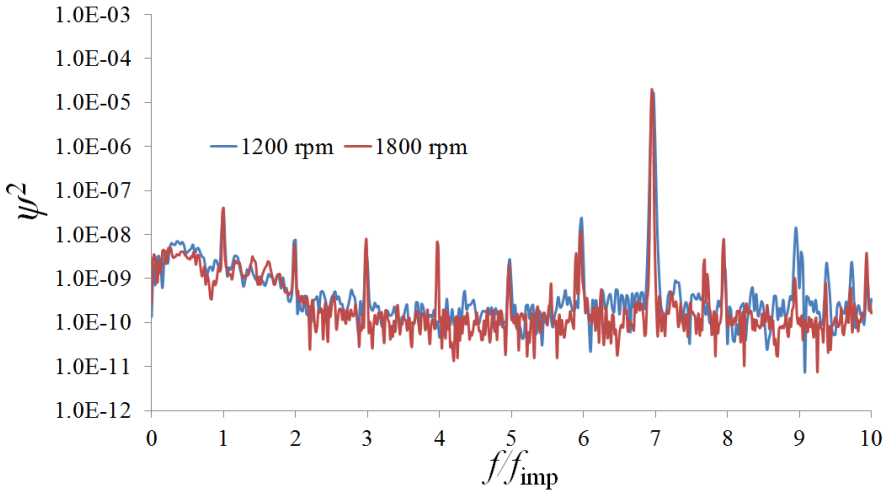

(a) Q/Q_d = 1.0

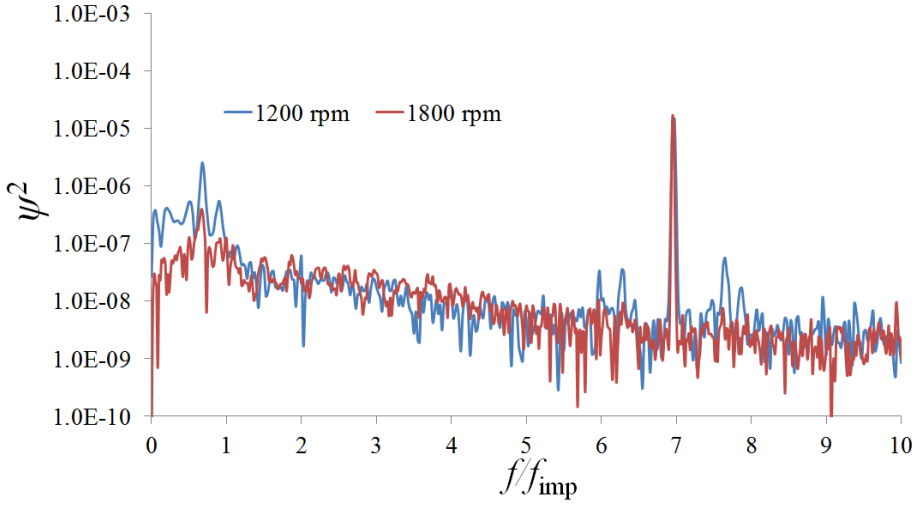

(b) Q/Q_d = 0.58

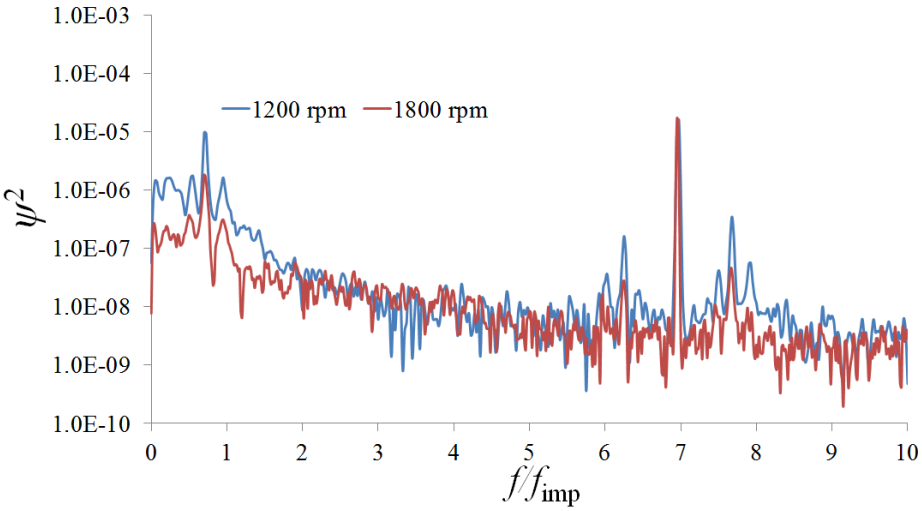

(c) Q/Q_d = 0.56

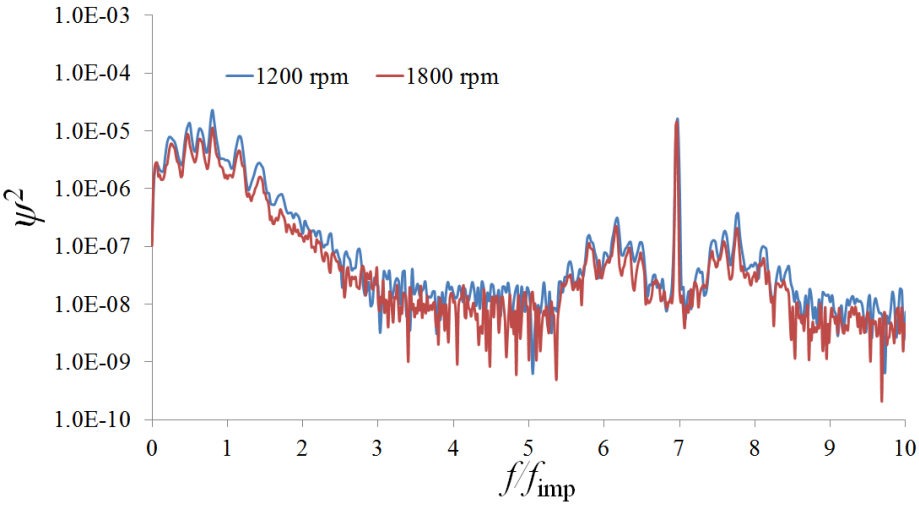

(d) Q/Q_d = 0.47

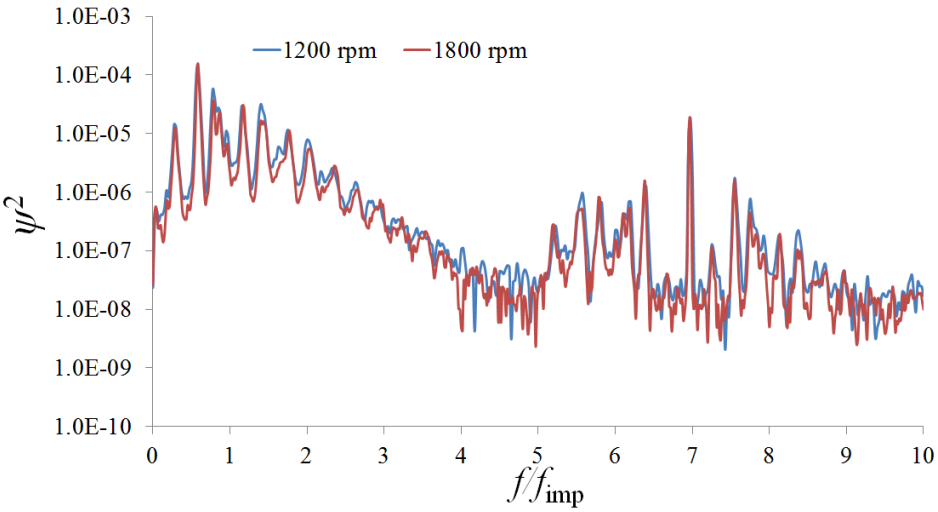

(e) Q/Q_d = 0.36

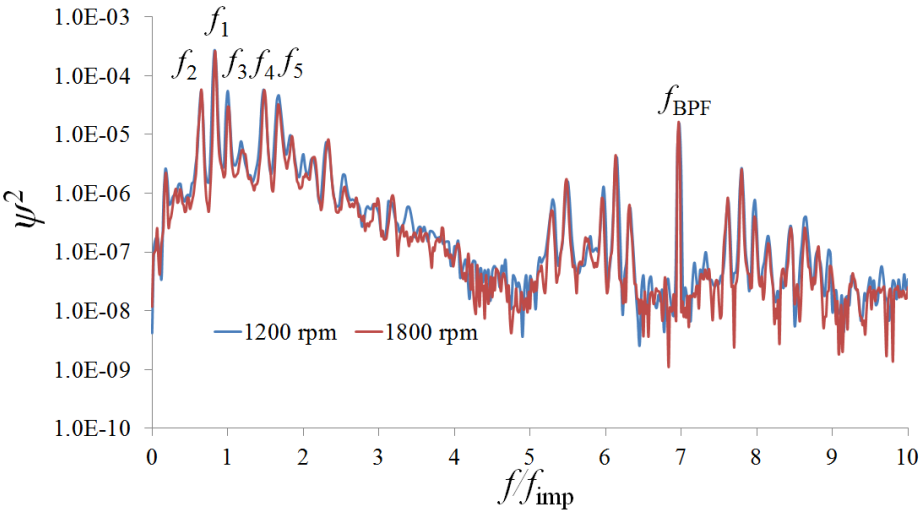

(f) $Q/Q_d = 0.26$

Figure 2.16 Cross-power spectra at different flow rates

2.4.2 Characteristics of rotating stall

The presence of rotating stall in the vaneless diffuser is confirmed through the spectrum analysis. In this section, the study will be extended to the analysis of the characteristics of the vaneless diffuser rotating stall: the number of stall cells, the amplitude and the propagation velocity associated with each mode will be determined.

2.4.2.1 Number of stall cells

Most of low frequency peaks are the result of the occurrence of instabilities in the vaneless diffuser: they may correspond to rotating stall, or to harmonics or nonlinear interaction of fundamental phenomena. Therefore, a dedicated spectrum analysis is applied to identify which peaks are corresponding to rotating stall modes, and discriminate the others.

As the microphone pressure fluctuation signal associated with one stall mode n is assumed to be:

$$\tilde{p}_m = p_0(r)\cos[n(\omega t - \theta)] \tag{2.15}$$

The determination of number of stall cells n depends on the measured phase difference between the two microphones $\Delta phase$ and the angular difference $\Delta\theta$,

$$n = |\Delta phase|/\Delta\theta \tag{2.16}$$

The phase difference was directly measured by the two microphones, and the angular difference $\Delta\theta = 75^o$, as shown in Figure 2.17 and 2.18.

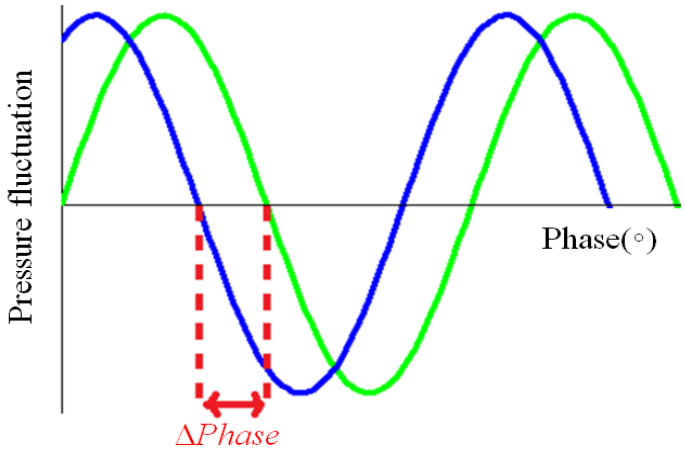

Figure 2.17 Phase difference in the spectrum

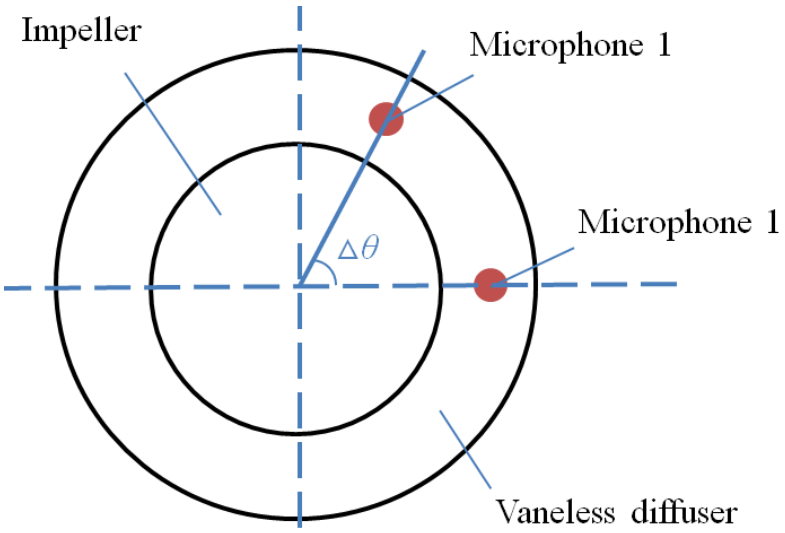

Figure 2.18 Angle difference between two microphones

Finally, a synthesis of the unstable modes that can be evidenced for each flow rates is proposed in Table 2.5. More details about the identification of rotating stall can be seen in Appendix C.

Table 2.5 Different modes of rotating stall

Q/Q_d	Dominant	Second	Third	Fourth
0.26	$n = 3$	$n = 2$	no	no
0.36	$n = 2$	$n = 3$	no	no
0.47	$n = 4$	$n = 2$	$n = 3$	no
0.56	$n = 4$	no	no	no
0.58	$n = 4$	no	no	no

At the five unstable conditions, the dominant stall modes are determined based on the amplitude. It can be seen that with the flow rate decrease, the dominant stall mode starts from 4 cells mode (Q/Q_d = 0.47, 0.56, 0.58), then becomes 2 cells mode (Q/Q_d = 0.36), and changes to 3 cells mode (Q/Q_d = 0.26) at last. Actually, a similar evolution of the dominant stall mode has been reported in a previous experimental study with a similar configuration (Dazin et al., 2008), as shown in Figure 2.19. However, a shift can be observed in the critical in the critical angle observed by Dazin et al (2008) and in the present experiments. This point is attributed to some modifications in the experimental configuration and will be discussed in chapter 2.6.

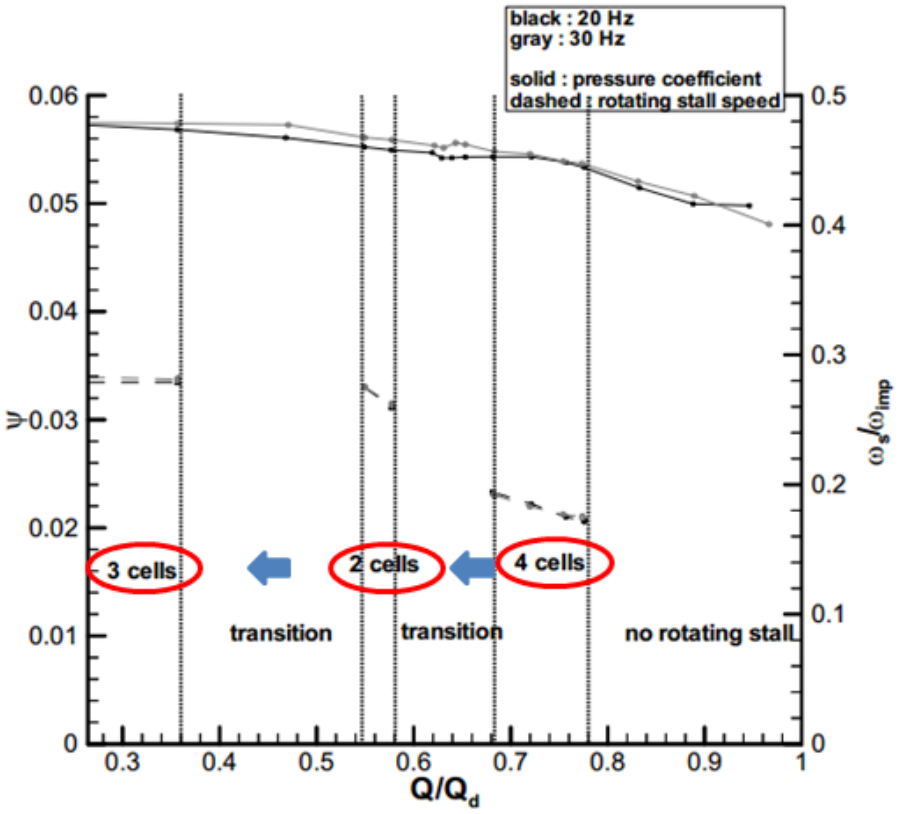

Figure 2.19 Dominant stall mode at Q/Q_d = 0.26 (Dazin et al., 2008)

2.4.2.2 Propagation velocity of stall cells

Once the number of cells of the stall mode is confirmed, and the corresponding frequency is given by the spectrum, then the circumferential propagation velocity of the stall cells ω, can be estimated as follow:

$$\omega = 2\pi \bullet f_{rs} / n \tag{2.17}$$

The amplitude and dimensionless circumferential velocity of stall cells versus flow rate are drawn in Figure 2.20, for different values of stall cell numbers. Concerning the amplitude, the general tendency is an increase of the intensity of the unstable flow with the flow rate decrease. On the other hand, the propagation velocity of stall cells is increasing with the decrease of flow rate. This can be linked with the increased circumferential velocity of the main flow at impeller outlet (diffuser inlet), as shown in Figure 2.21: the decrease of flow rate results in the decrease of the radial velocity component ($V_r \rightarrow V_r'$), meanwhile the

circumferential velocity of the main flow increase from $V_\theta \rightarrow V_\theta'$. Consequently, the propagation velocity of stall cells (involved in the diffuser main flow) is then increased. The evolution of the circumferential velocity at diffuser inlet is also plotted in Figure 2.20(b). Besides, another mechanism is proposed by Ljevar (2007), who indicated that the increase of flow rate results in a further distance of the cells from the impeller, and then to a lower propagation velocity of rotating stall cells.

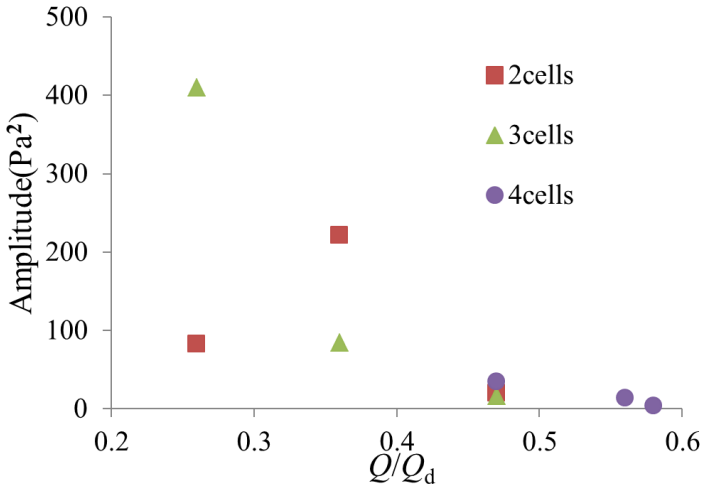

(a)

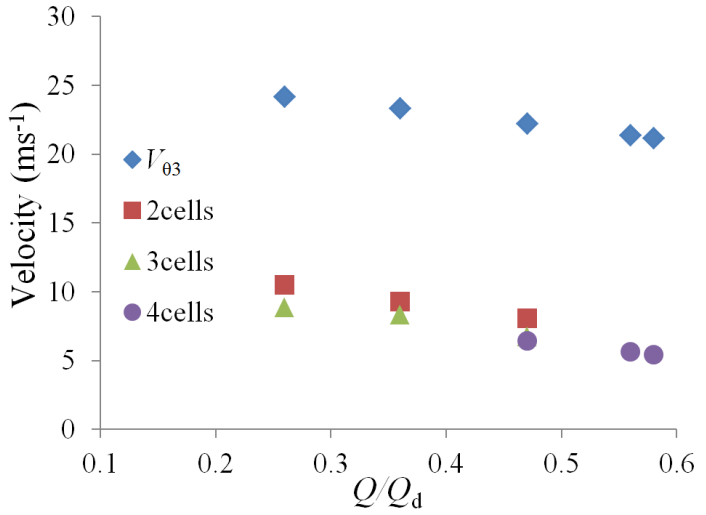

(b)

Figure 2.20 The amplitude (a) and circumferential velocity (b) of stall cells for 1200 RPM

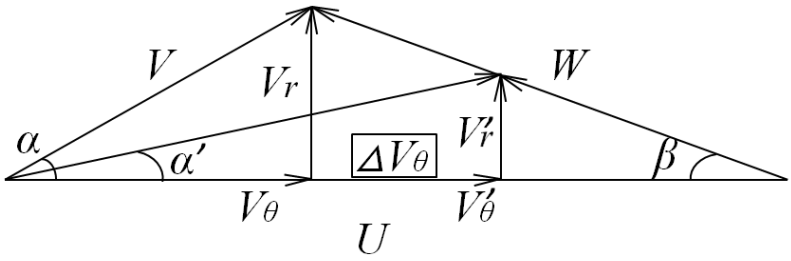

Figure 2.21 Velocity triangles at impeller outlet (diffuser inlet)

2.5 Effect of rotating stall on the diffuser performance

The performance curve plotted in Figure 2.14 presents a clear effect of rotating stall on the diffuser performance: a sudden performance increase appears when the flow rate decreases to the critical value, which leads to the onset of rotating stall.

With such an observation, the following study will discuss how the vaneless diffuser performance is affected by the arising rotating stall. To focus the effect on the diffuser performance, the pressure recovery in the vaneless diffuser, scaled by the kinetic energy at the diffuser inlet is plotted in Figure 2.22.

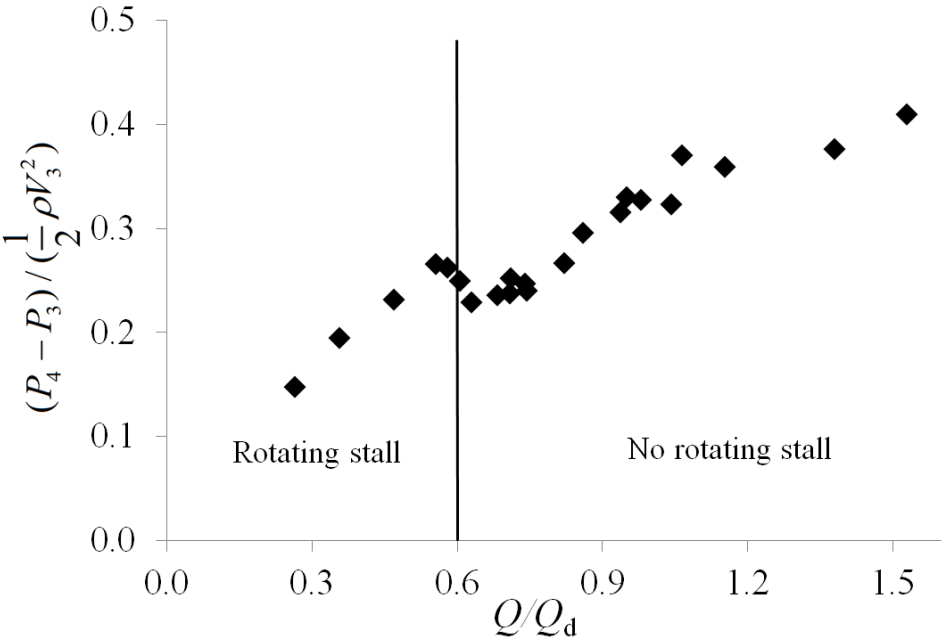

Figure 2.22 Diffuser static pressure recovery versus flow rate ratio (P_4 – Diffuser outlet pressure, P_3 – Diffuser inlet pressure)

The absolute velocity at diffuser inlet V_3 has been evaluated by the determination of the velocity triangle at impeller outlet (V_2, V_{2r}, $V_{2\theta}$), as follows

$$V_3 = \sqrt{V_{3r}^2 + V_{3\theta}^2} \tag{2.18}$$

From continuity equation : $$V_{3r} r_3 = V_{2r} r_2 \tag{2.19}$$

From momentum equation : $$V_{3\theta} r_3 = V_{2\theta} r_2 \tag{2.20}$$

In stable conditions (without rotating stall), it can be seen that the pressure recovery is decreasing with the decrease of flow rate, but shortly increased at the onset of rotating stall, and then decreased again when rotating stall is fully developed.

To have a deeper understanding of this result, an analysis of the losses in the diffuser is proposed: the isentropic increase of pressure due to the gradually velocity decrease in the diffuser has been calculated and compared to the experimental pressure recovery (Figure 2.23): more precisely, at the diffuser outlet, the pressure difference between the isentropic

theoretical estimation and the experimental result is then defined as experimental losses, and an experimental loss coefficient can be defined as:

$$\varepsilon = Losses / (\rho \frac{V_3^2}{2}) \tag{2.21}$$

In which: $Losses = P_{4is} - P_4$

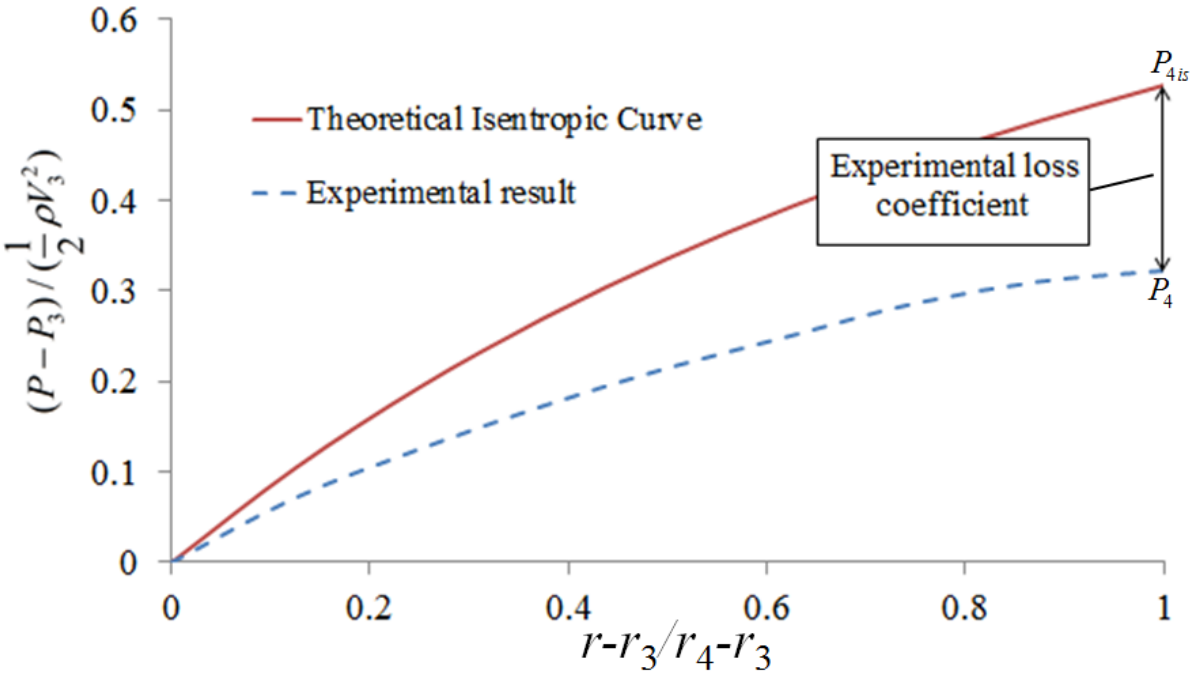

Figure 2.23 Pressure recovery curve at design flow rate $Q/Q_d = 1.0$

The losses in a vaneless diffuser, in stable operations, are usually divided into three terms:

(1) Losses due to friction that can be modeled by a friction factor derived from the ones obtained in duct flows.

(2) Additional losses due to the adverse pressure gradient. These losses are commonly called diffusion losses.

(3) Losses due to the mixing of the jet wake pattern coming out from the impeller.

The present study is neglecting the two last losses sources because:

For (2): The diffusion losses could be neglected if the streamline in the diffuser is sufficiently long (Aungier, 1993; Dou, 1991). Dou (1991) showed that the diffusion losses could be neglected for diffuser width of the same order of magnitude compared to the one used in the present study ($B_3/r_2 = 0.15$) if the absolute flow angle at diffuser inlet is lower than 25°. In the present study, the diffuser inlet flow angle varies from 2.3° to 24.6°, depending on the tested flow rate.

For (3): The mixing losses are concentrated in the region close to the impeller outlet ($1.00 < r/r_2 < 1.06$) (Dou, 1989 and 1991). In the present study, the pressure taps are located in the range of $1.03 < r/r_2 < 1.5$. Therefore, the mixing losses have contributions at $1.03 < r/r_2 < 1.06$ which is a small part of the whole diffuser, and will not affect the growing losses in the rest part ($1.06 < r/r_2 < 1.5$) of the vaneless diffuser.

Consequently, if the vaneless diffuser is on stable operation, the losses analyzed in the present study are supposed to be mainly due to friction losses along the length L of a streamline:

$$Losses = \frac{\lambda}{D_{\mathrm{H}}} \rho \frac{V_3^2}{2} L \tag{2.22}$$

Where

– D_{H} is the hydraulic diameter, and in the present vaneless diffuser,

$$D_H = \frac{4S}{C_P} \tag{2.23}$$

In which S is the cross sectional area which is equal to $2\pi r \bullet B_3$, and C_{P} is the perimeter of the cross-section which is equal to $4\pi r$.

– λ is the friction factor, which relies on the relative wall roughness: R_a/D_{H} and Reynolds number: Re, then the value of λ can be obtained from the Moody diagram, as shown in Figure 2.24. In present experiment, with the varying flow rate, the Reynolds number varies from $0.69 \times 10^5 \sim 1.27 \times 10^5$.

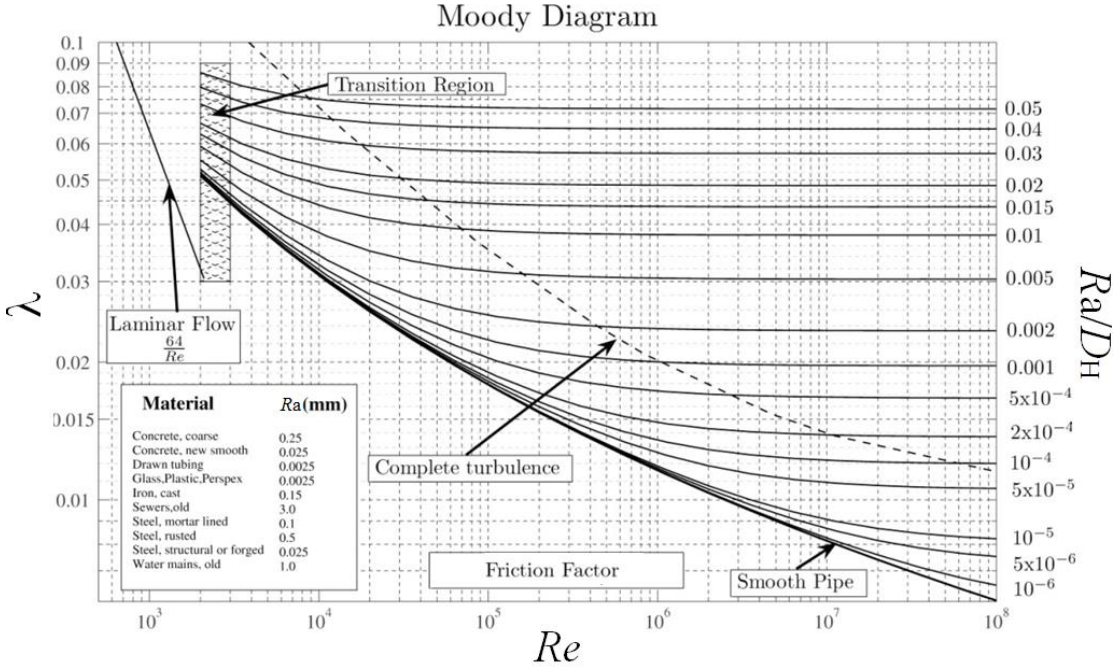

Figure 2.24 Moody diagram

According to the definition of loss coefficient in expression (2.21), and making the assumption that the friction loss is the main part of the losses in the vaneless diffuser, the diffuser loss coefficient at stable conditions is then obtained:

$$\varepsilon_S = Losses / (\rho \frac{V_3^2}{2}) = \frac{\lambda}{D_H} \bullet L \tag{2.24}$$

which is a linear function of the length of streamline *L*, with the slope: $\frac{\lambda}{D_H}$.

The expressions (2.19) and (2.20), which have shown that for any two locations on the streamline in the vaneless diffuser (For example, position *C* and *D* in Figure 2.25), we have the following relation

$$\frac{V_{Cr}}{V_{C\theta}} = \frac{V_{Dr}}{V_{D\theta}} \tag{2.25}$$

which means that the flow angle of the streamline keeps constant. This kind of curve is known as a logarithmic spiral. The length of the streamline *L*, can be determined by equation (2.26),

$$L = r_3 \sec(\alpha + \frac{\pi}{2})(e^{\theta \cot(\alpha + \frac{\pi}{2})} - 1) \tag{2.26}$$

where $\theta = \frac{\ln r_4 - \ln r_3}{\cot(\alpha + \frac{\pi}{2})}$, in which α is the diffuser inlet flow angle, and was estimated from the calculation of the velocity triangle at impeller outlet (corrected by the Stodola slip factor):

$$\alpha = \arctan \frac{V_{2r}}{V_{2\theta}} \tag{2.27}$$

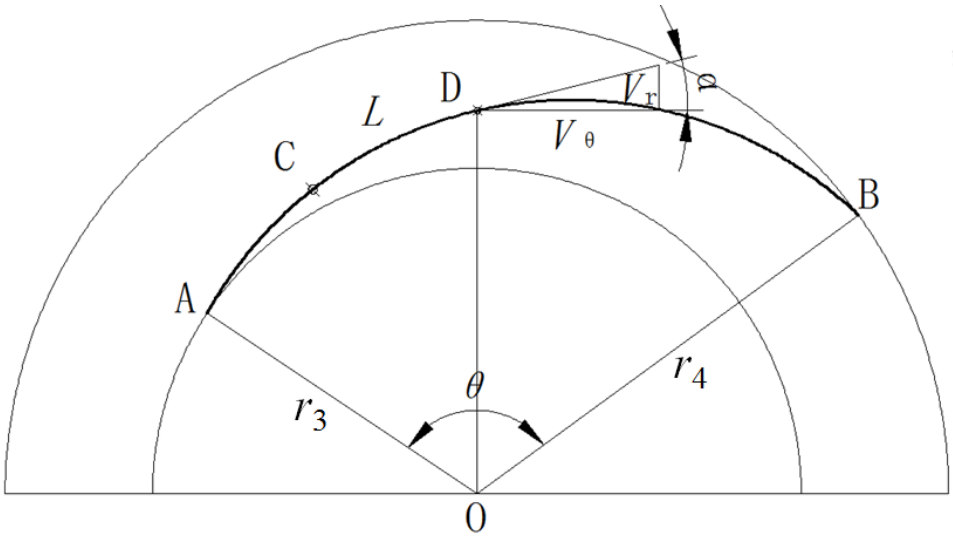

Figure 2.25 Streamline in the vaneless diffuser

It can be seen that the length of streamline is depending only on the value of the absolute flow angle α at diffuser inlet and is thus increasing with the flow rate decrease, the results are given in Figure 2.26.

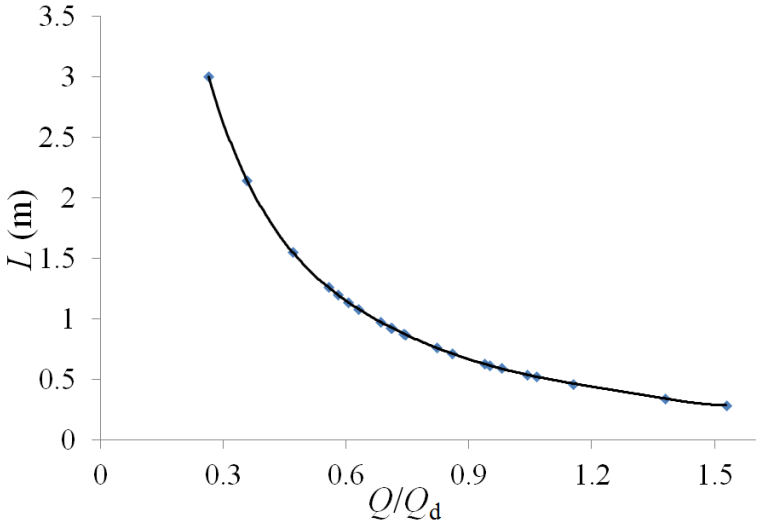

Figure 2.26 Length of streamline versus the flow rate

With the definition of loss coefficient in Figure 2.23 and the length of streamline in Figure 2.26, the loss coefficients versus the length of streamline are plotted in Figure 2.27 (the detailed values of the loss coefficient at each flow rate are given in Appendix D). It can be seen that the loss coefficient increases linearly with the streamline length for small value of L, that is, for operating conditions without rotating stall (stable conditions). Moreover, it is noticeable that the experimental slope (≈ 0.32) is close to the theoretical one λ/D_H (= 0.28 which is defined in equation (2.24). As a first conclusion, this result confirmed the assumption of equation (2.24): the friction loss coefficient at stable condition is a linear function of the streamline, and thus the friction losses are the main part of the total losses in the vaneless diffuser.

What is particularly notable in Figure 2.27 is that the arising of rotating stall is corresponding to a clear drop of the losses. This is confirmed again in Figure 2.28, presenting the evolution of the loss coefficient as a function of the flow rate. In this figure, the loss coefficient drop at the arising of rotating stall is also obvious. After this drop, the losses are increasing again with the decrease of the flow rate, but this time with a clear much smaller slope than the one (ε_S) calculated based on the length of logarithmic spiral which represents the conditions without rotating stall. According to such a result, it seems that the occurrence of rotating stall decreased the losses in the vaneless diffuser, and results in a diffuser performance higher than the one we would have if the machine keeps working at stable conditions.

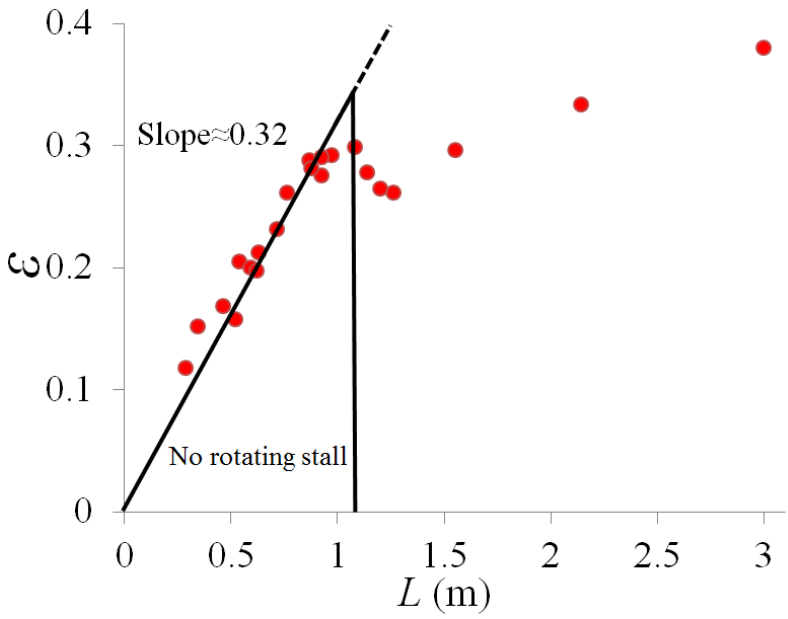

Figure 2.27 Experimental Diffuser loss coefficient at diffuser outlet versus length of streamline

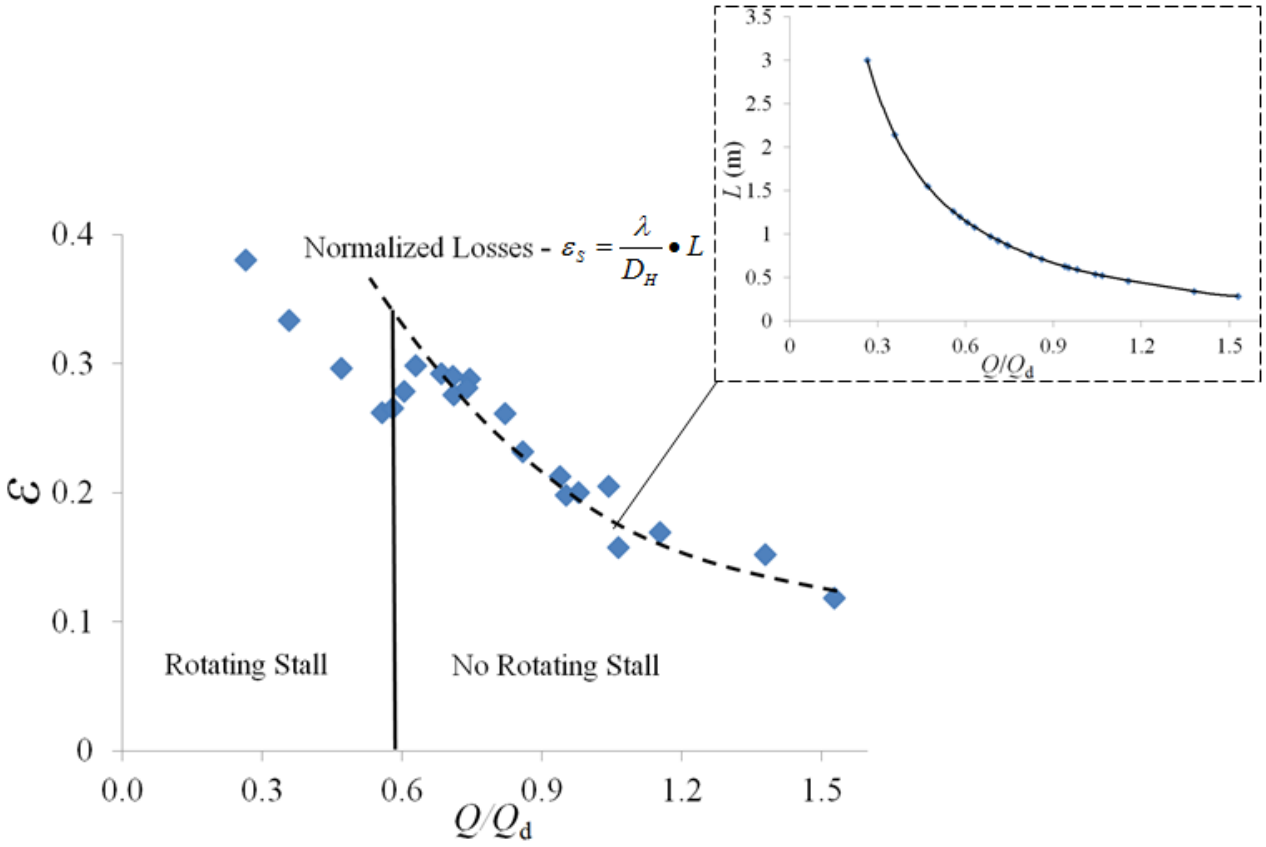

Figure 2.28 Losses at diffuser outlet versus flow rate ratio Q/Q_d

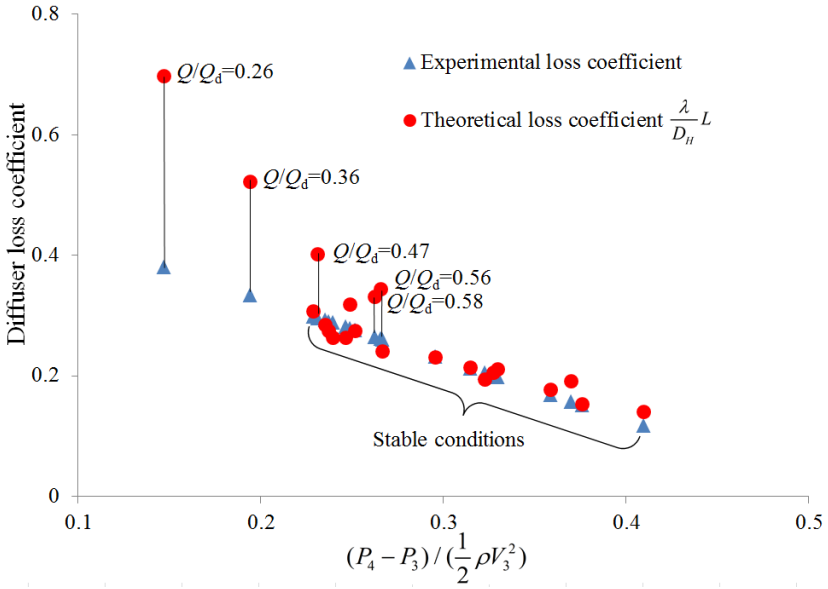

Figure 2.29 Diffuser losses coefficient versus static pressure recovery coefficient

Figure 2.29 gives the diffuser experimental and theoretical losses coefficient versus the static pressure recovery coefficient. The experimental loss coefficient is a straight line. This is due to the definition of the experimental losses which are defined as the difference between the isentropic pressure recovery and the experimental pressure recovery. In another form,

$$\varepsilon = \frac{(P_{4is} - P_3) - (P_4 - P_3)}{0.5\rho V_3^2} \tag{2.28}$$

Then it can be written as follow

$$\varepsilon = (1 - \frac{r_3^2}{r_4^2}) - \frac{(P_4 - P_3)}{0.5\rho V_3^2} \tag{2.29}$$

The theoretical loss coefficient is calculated based on equation (2.24) which assumes that the diffuser flow is stable (without rotating stall). It can be seen that the experimental loss coefficient agrees well with the theoretical one while the diffuser flow is stable. However, with the occurrence of rotating stall ($Q/Q_d < 0.58$), the experimental loss coefficient is not as large as the theoretical prediction, which confirm the effect of rotating stall on the diffuser performance. As a conclusion, it seems that the arising of the instability could be a way, for the flow, to reduce its losses when the flow angle is very low at diffuser inlet.

Two possible reasons may explain why the pressure recovery is increased in presence of rotating stall: First, Figure 2.30, from previous experimental study with the same configuration (Dazin et al., 2011), gives the PIV results of the radial velocity in the vaneless diffuser (at $Q/Q_d = 0.26$). Three rotating cells can be identified and each cell is composed of two cores with inward and outward radial velocity. Therefore, one can consider that the rotating cells generate a blockage region due to the inward radial velocity near the diffuser outlet. Consequently, the flow in the regions outside of rotating cells is characterized by

higher radial velocities than what we would have without rotating cells. Therefore, the real streamline could become shorter than the one we would have without rotating stall, and then the shorter streamline leads to smaller friction losses.

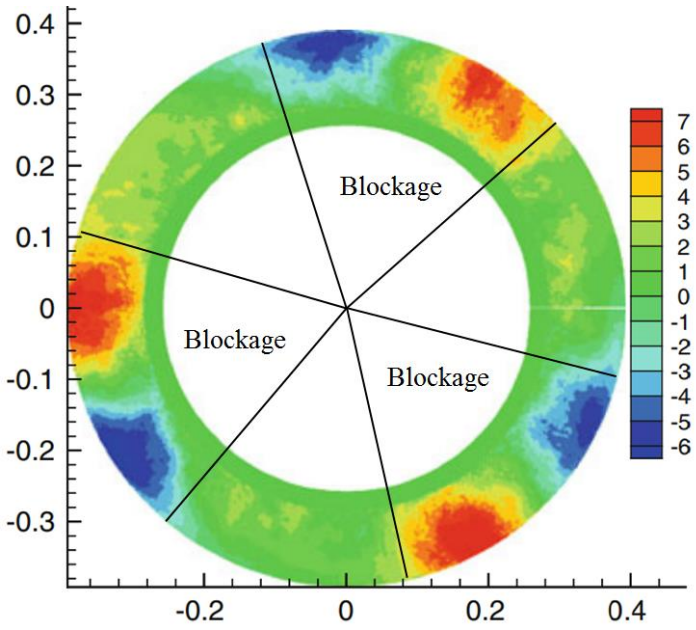

Figure 2.30 Radial velocity in the vaneless diffuser at Q/Q_d = 0.26 (Dazin et al., 2011)

To estimate the streamline, previous PIV results were used to estimate the blockage induced by the rotating cells. Then, the space of the vaneless diffuser can be divided into two parts, as shown in Figure 2.31:

(1) Part 1: Before the streamline reaches to the boundary of cells, it can be assumed that the streamline is not affected by the presence of rotating stall.
(2) Part 2: After the streamline reaches to the stall zone, the effect of blockage due to stall cells has to be taken into account.

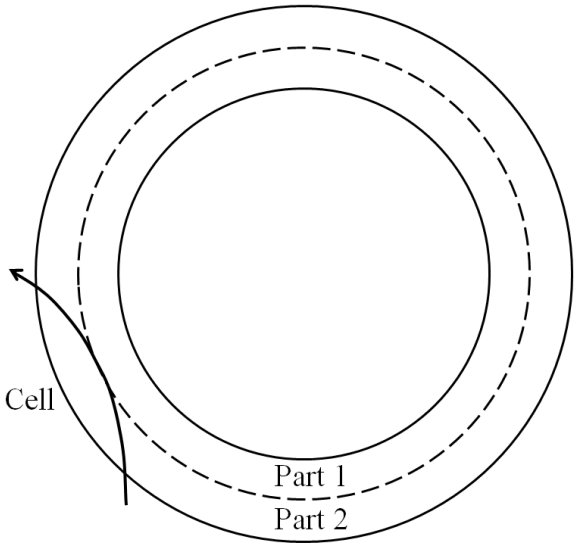

Figure 2.31 Two assumed regions in the vaneless diffuser

Therefore, in Figure 2.32, the length of streamline 1 has been calculated as before (without rotating stall). For streamline 2, the new radial velocity has been calculated taking into account the blockage area identified from PIV results. Then, a new flow angle and a new length of streamline 2 have been estimated. Finally, the new estimation of friction losses based on the new length of streamline has been calculated (with the same value of λ / D_H used before) and compared with experimental results, as shown in Figure 2.33.

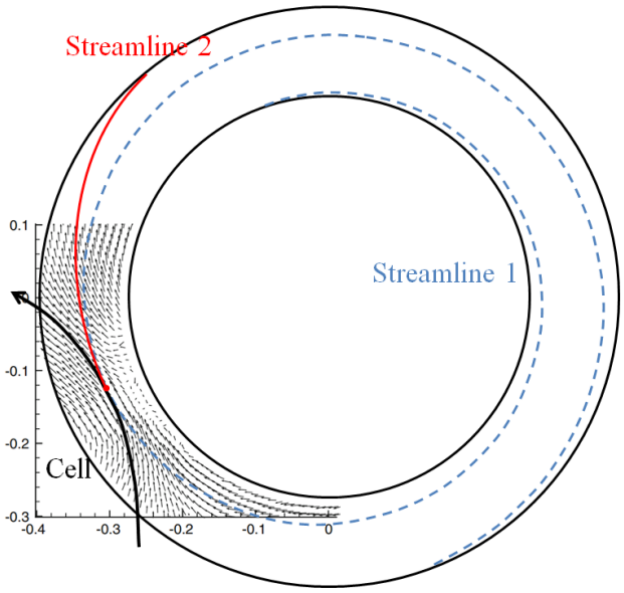

Figure 2.32 Assumption of the real streamline

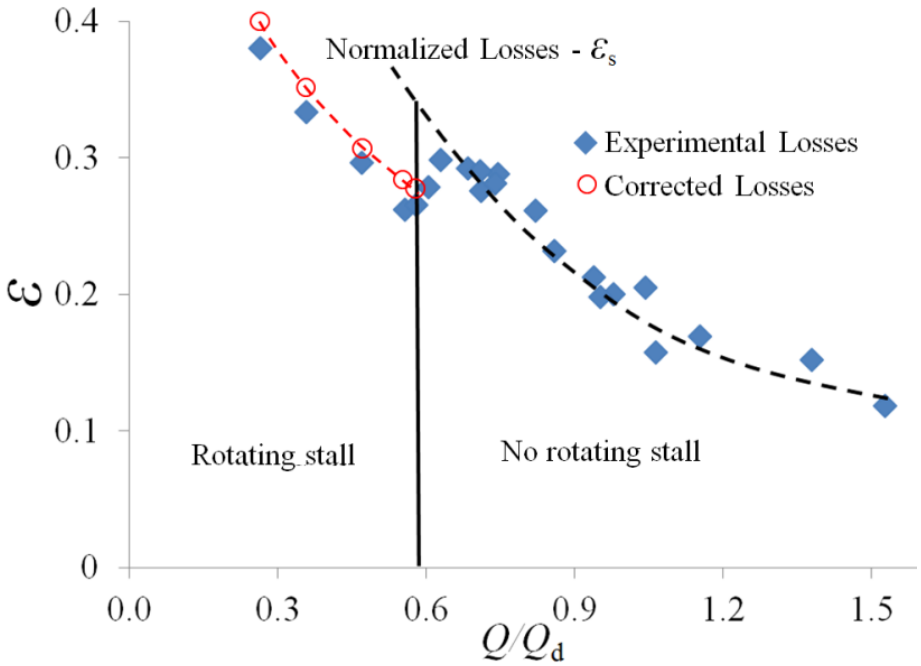

Figure 2.33 Comparison between experimental losses and corrected losses

In spite of the simplicity of the model, a good agreement is obtained between the corrected loss coefficient and the experimental results, which means that the blockage due to rotating

stall cells must be the major cause of the reduction of the losses in unstable operation of the diffuser.

One can nevertheless notice that the corrected losses are a little bit higher than the experimental losses. Therefore, a second explanation has also to be considered: the pressure which is measured at the diffuser outlet is a time averaged value and considering the topology of cells, it can be seen that they are characterized by regions of inward radial velocity. Consequently, some high pressure flow coming from downstream of the diffuser (the ambient air at atmospheric pressure) is convected in the diffuser (Figure 2.34), then the measured time averaged pressure is actually increased.

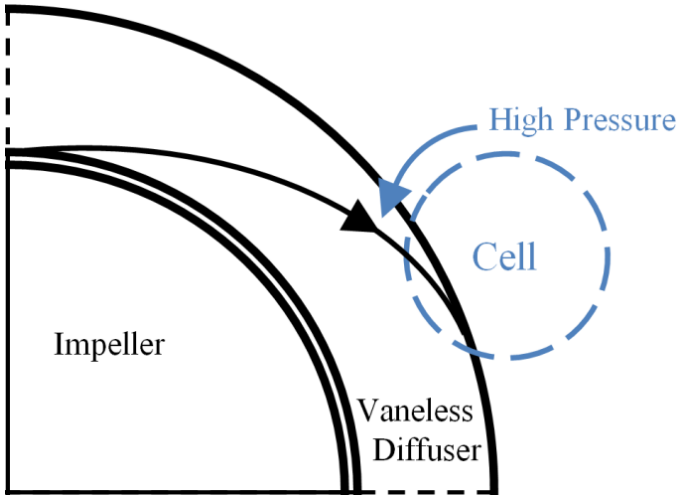

Figure 2.34 Convection at the diffuser outlet

2.6 Effect of the geometrical configuration

In Table 2.5, all the identified stall modes have been listed at each flow condition. Comparing the dominant stall mode to previous experimental results (Figure 2.19), a similar evolution is observed: the dominant stall mode changes with the decrease of flow rate: 4 cells (Q/Q_d = 0.47, 0.56, and 0.58) → 2 cells (Q/Q_d = 0.36) → 3 cells (Q/Q_d = 0.26). However, a clear shift of the critical flow condition for each dominant stall modes can be observed in Figure 2.35. For example, mode n = 4 appeared at Q/Q_d = 0.78 in previous study, and the critical flow rate for mode n = 4 moves to Q/Q_d = 0.58 in the present experiment.

The first difference between the present and previous experiment is the diffuser width which has been decreased from 40 mm (previous) to 38.5 mm (present). As a result, the comparison shows the flow in a narrow diffuser is more stable than in a wide one, the critical stall condition for each stall mode moves to a lower flow rate. The same conclusion has also been reported by Jansen (1964a), Senoo et al (1977), Ligrani et al (1982), Ötügen et al (1988), Moore (1991) and Ljevar (2007), they reported that the narrower vaneless diffusers have a wider operating range than the wider ones. The mechanism can be explained with the help of the linear stability analysis proposed by Tsujimoto et al (1996), who indicated that the critical flow angle of rotating stall in the wide vaneless diffuser, is only the function of the diffuser radius ratio and the number of stall cells, and independent on the diffuser width.

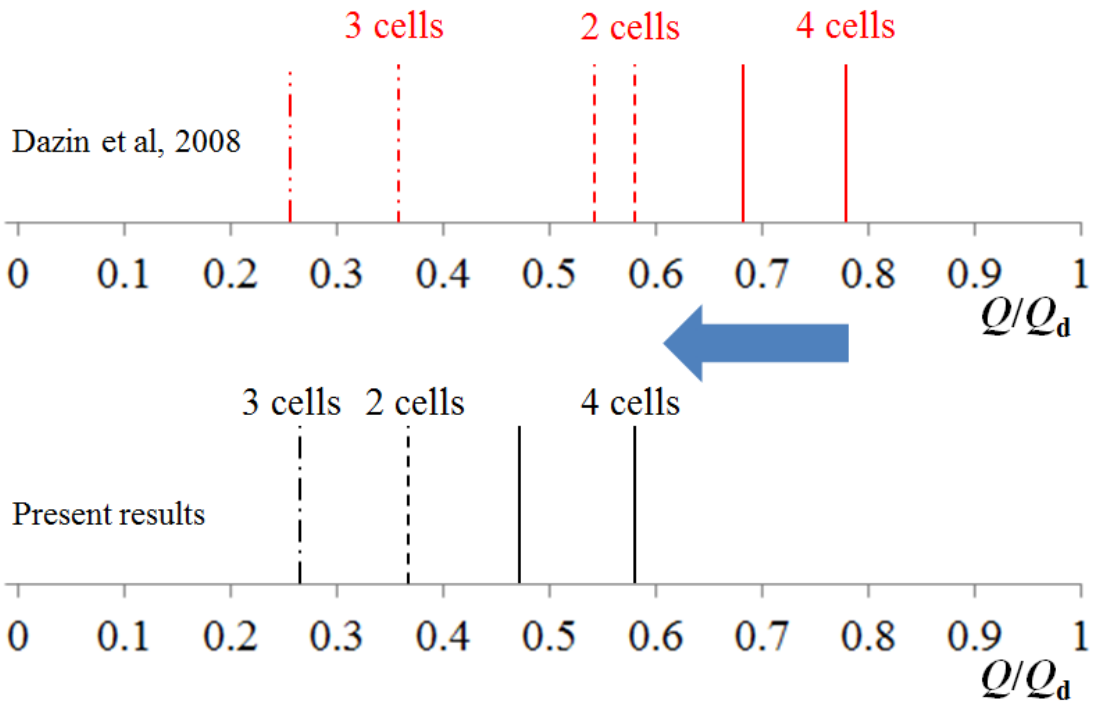

Figure 2.35 Comparison of the critical flow rate for the dominant stall modes

Therefore, if the critical flow angle is fixed for a given vaneless diffuser, for a given flow rate, one can imagine that the radial velocity component is larger in a small width diffuser than in a large width diffuser. Consequently, the decrease of the diffuser width ratio results in an increase of flow angle, and rotating stall will not occur if the increased flow angle is higher than the critical value. For example, the critical flow angle of mode $n = 4$ is reached at $Q/Q_d = 0.78$ in previous experiment, but in the present experiment, the real flow angle at the same flow condition $Q/Q_d = 0.78$ is actually higher than the critical value, then the same stall mode cannot be observed.

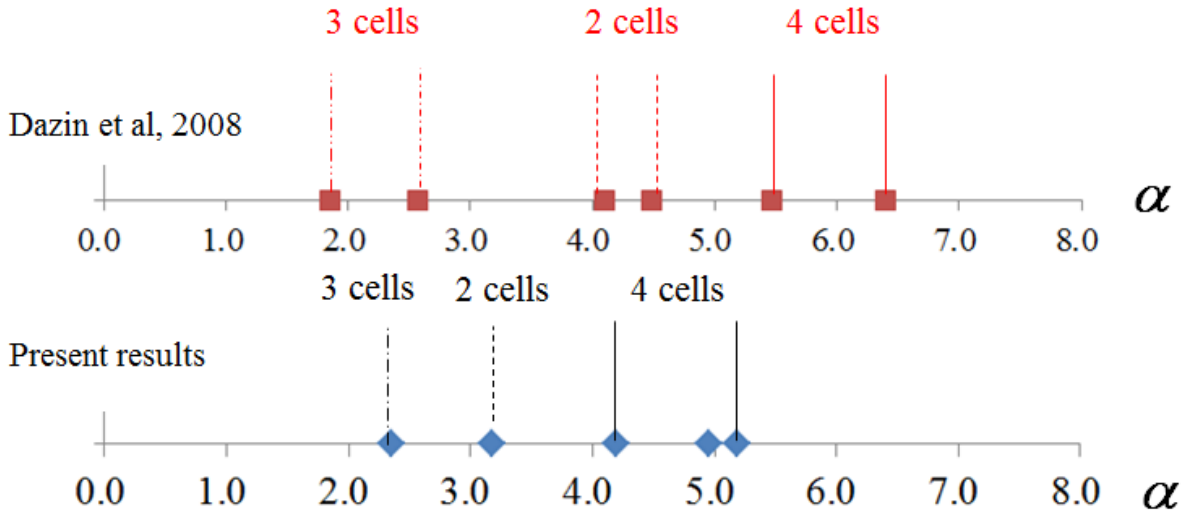

Figure 2.36 Comparison of the critical flow angle for the dominant stall modes

In Figure 2.36, the observed dominant stall modes are plotted as a function of the flow angle in order to take the effect of the diffuser width into account. Comparing the critical flow

angle for n = 4 in present study (Q/Q_d = 0.58) to previous result (Q/Q_d = 0.78), it can be seen that the critical flow angle in the present study is still smaller than previous study. This may be due to the second geometrical difference: the gap between the impeller and the diffuser in present experiment is slightly larger than before.

On the one hand, this larger gap will increase the leakage flow. Consequently, the diffuser inlet flow angle will be increased. Then, closer results for the critical flow angle in Figure 2.36 can be expected. On the other hand, the result presented by Pavesi et al (2011) in Figure 2.37 shows a clear interaction between the leakage flow and the diffuser core flow, and this effect is stronger at shroud side than at hub side due to the different joint shapes (Figure 2.13). Therefore, the stability of the diffuser flow is possibly affected by this interaction effect.

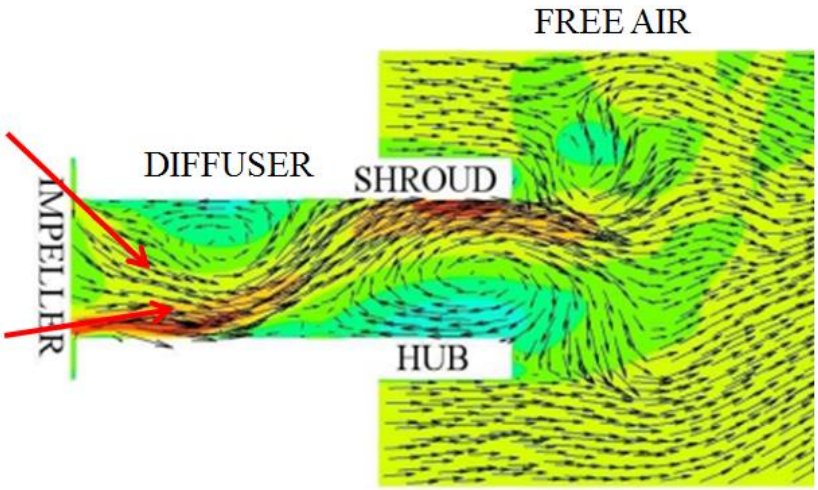

Figure 2.37 Flow field in the vaneless diffuser (Pavesi et al, 2011)

2.7 Conclusions

In this chapter, the experiment performed to study rotating stall in the vaneless diffuser has been presented. The presence of rotating stall is detected by the spectrum analysis: at stable conditions, the dominant frequency in the spectrum is the blade passing frequency, the impeller frequency and its harmonics are also significant; at unstable conditions, several low frequency peaks dominate the spectrum instead of the blade passing frequency. These low frequencies, are then classified to be rotating stall, impeller frequency, or harmonics by a dedicated spectrum analysis.

Since the presence of rotating stall is confirmed, the characteristics of rotating stall are then obtained based on the experimental results.

(1) The number of stall cells, is determined by the signal phase difference delivered by the two microphones.

(2) The propagation velocity of stall cells, is determined by the frequency of the peak and the number of stall cells.

(3) The critical flow angle, is directly linked with the corresponding flow rate.

The effect of rotating stall on the vaneless diffuser performance was also analyzed. The result shows that, for operating points with no rotating stall, the losses increase linearly with the length of streamline in the diffuser. But, it has also been observed that the development of rotating stall is corresponding to a decrease of the losses. The arising of instability has thus a positive effect on the diffuser performance. Two possible reasons were offered:

(1) The blockage due to the occurrence of the rotating instability induces shorter lengths of streamline which decreases the friction losses.

(2) The convection at the diffuser outlet makes the measured pressure higher than the one we would have without rotating stall.

The evolution of the dominant stall modes in present study is the same as previous study, but each dominant stall mode occurs at a lower flow rate than before. Two explanations were proposed:

(1) The smaller diffuser width in present experiment increased the flow angle of the diffuser core flow.

(2) The larger gap in present study not only increased the flow angle in the vaneless diffuser, but also interacts with the core flow which affects the stability of the diffuser flow.

Chapter 3 Linear stability analysis

3.1 Introduction

In this chapter, a theoretical study of rotating stall in a radial vaneless diffuser is presented. With several assumptions (two dimensional, axisymmetric, inviscid and incompressible), a linear stability model is constructed. The critical stability problem of the flow in the vaneless diffuser is then represented by two groups of solution: One group of solution is for the stable flow, which can be directly solved by specifying the boundary flow condition; another group of solution is for the perturbations, which can be solved with specified boundary conditions. With the constructed linear stability model, the characteristics of rotating stall in the vaneless diffuser are calculated and compared to the experimental results and the linear stability analysis presented by Tsujimoto et al (1996). Moreover, the velocity and pressure fluctuations predicted by present study also have been compared to previous PIV experiment and similar results found in literature. Whereas Tsujimoto et al (1996) work, the present analysis is not focused only on the critical conditions of rotating stall, but extended also to the study of unstable conditions. Then, the growth rate of stall mode is calculated to determine the dominant stall mode (that is, the one with maximum growth rate) at unstable conditions. The results are discussed and compared with the experimental results.

A discussion of the cause of the instability is proposed and the growth rate of the perturbation is calculated. The analysis shows that the growth rate can be expressed into three parts, and the contribution of each part is then discussed. Based on the characteristics time in radial and tangential, an analysis is proposed to explain why the instability is developing in the experiment (different modes exist intermittently), and the condition for the developing of stall modes is also proposed.

Through the comparisons and discussions, the abilities and limits of this kind of linear stability analysis are discussed at the end.

3.2 Hypotheses

To simplify the theoretical model, and according to the experiment setup in chapter 2, several assumptions are made in this part. In the experiment study, the width ratio of the vaneless diffuser is: $B_3/r_2 = 0.15$, which is a typical wide vaneless diffuser. Therefore, as it is stated before, a two dimensional core flow is able to represent the main flow in the vaneless diffuser, a first assumption is proposed: the flow is supposed to be two dimensional.

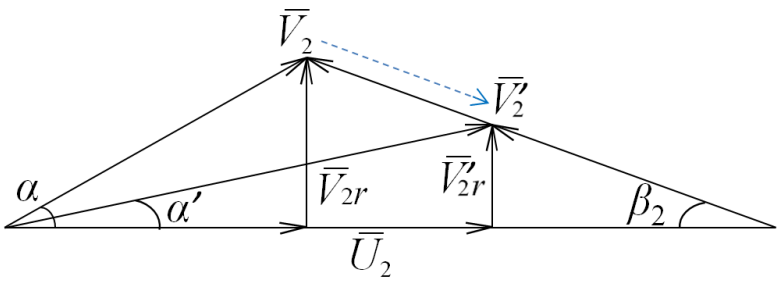

Figure 3.1 Velocity triangle at impeller outlet

The velocity triangle at impeller outlet (Figure 3.1) explained that for the fixed impeller blade angle β_2 and rotational speed U_2, the decrease of the flow rate results in the decrease of the radial component V_{2r}. Consequently, the absolute velocity at impeller outlet V_2 increased. Therefore, the maximum velocity in the vaneless diffuser appeared at the lowest flow rate Q/Q_d = 0.26, which is nearly equal to 24 m/s. Then, the corresponding maximum Mach number is then calculated: Ma = 0.07, which means the flow in present study is a subsonic and incompressible flow. In addition, the diffuser inlet flow is assumed to be axisymmetric, and as the problem is focusing on the core flow behavior, the viscosity will not be taken into account.

All the hypotheses are summarized below,

(1) The vaneless diffuser flow is two dimensional and the boundary conditions are axisymmetric, with uniform static pressure at diffuser outlet (atmosphere pressure) and imposed velocity magnitude and angle at inlet.

(2) The fluid is incompressible and inviscid.

3.3 Linear model

3.3.1 Dimensional equations and basic solutions

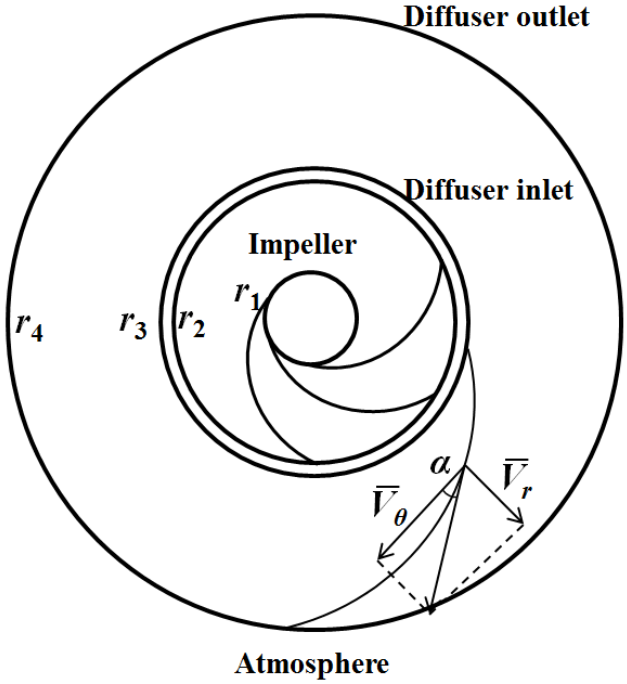

Figure 3.2 Flow in the vaneless Diffuser

At first, the linear stability analysis is started from dimensional form (the quantities with overbar). Some of the parameters used in the analysis are summarized in Figure 3.2. The continuity equation in cylindrical coordinate system is then,

$$\frac{\partial \bar{\rho}}{\partial \bar{t}} + \frac{1}{\bar{r}} \frac{\partial (\bar{r}\, \bar{\rho} \bar{V}_r)}{\partial \bar{r}} + \frac{1}{\bar{r}} \frac{\partial (\bar{\rho} \bar{V}_\theta)}{\partial \theta} + \frac{\partial (\bar{\rho} \bar{V}_z)}{\partial z} = 0 \tag{3.1}$$

Because the flow is two dimensional and the fluid is incompressible , one get:

$$\frac{\partial \bar{\rho}}{\partial \bar{t}} = 0 \text{ , and } \frac{\partial \bar{V}_z}{\partial z} = 0 \tag{3.2}$$

Therefore, the continuity equation becomes

$$\frac{\partial (\bar{r}\bar{V}_r)}{\partial \bar{r}} + \frac{\partial \bar{V}_\theta}{\partial \theta} = 0 \tag{3.3}$$

As it is usually done for machine working with air, the effect of gravity are neglected and the momentum equation is

$$\bar{\rho}[\frac{\partial \vec{\bar{V}}}{\partial \bar{t}} + (\vec{\bar{V}} \cdot \vec{\nabla})\vec{\bar{V}}] = -\vec{\nabla} P \tag{3.4}$$

Since the flow is two dimensional, we have, in the radial direction:

$$\bar{\rho}\left[\frac{\partial \bar{V}_r}{\partial \bar{t}} + \bar{V}_r \frac{\partial \bar{V}_r}{\partial \bar{r}} + \frac{\bar{V}_\theta}{\bar{r}} \frac{\partial \bar{V}_r}{\partial \theta} - \frac{\bar{V}_\theta^2}{\bar{r}}\right] = -\frac{\partial \bar{P}}{\partial \bar{r}} \tag{3.5}$$

and in the tangential direction

$$\bar{\rho}\left[\frac{\partial \bar{V}_\theta}{\partial \bar{t}} + \bar{V}_r \frac{\partial \bar{V}_\theta}{\partial \bar{r}} + \frac{\bar{V}_\theta}{\bar{r}} \frac{\partial \bar{V}_\theta}{\partial \theta} + \frac{\bar{V}_r \bar{V}_\theta}{\bar{r}}\right] = -\frac{1}{\bar{r}} \frac{\partial \bar{P}}{\partial \theta} \tag{3.6}$$

where $\bar{V}_r$ is the radial velocity, $\bar{V}_\theta$ is the tangential velocity.

The vorticity is defined as $\vec{\bar{\zeta}} = rot(\vec{\bar{V}})$, and applying the curl operator to equation (3.4), one obtained

$$\bar{\rho}[\frac{\partial \vec{\bar{\zeta}}}{\partial \bar{t}} + rot(\vec{\bar{V}} \cdot \vec{\nabla}\vec{\bar{V}})] = -rot(\vec{\nabla} P) \tag{3.7}$$

with

$$\vec{\bar{V}} \cdot \vec{\nabla}\vec{\bar{V}} = \frac{1}{2}\vec{\nabla}\left|\vec{\bar{V}}\right|^2 + rot(\vec{\bar{V}}) \wedge \vec{\bar{V}} = \frac{1}{2}\vec{\nabla}\left|\vec{\bar{V}}\right|^2 + \vec{\bar{\zeta}} \wedge \vec{\bar{V}}$$

and it is known that the curl of the gradient is 0, then the two terms

$$\begin{cases} rot(\frac{1}{2}\vec{\nabla}\left|\vec{\bar{V}}\right|^2) = 0 \\ rot(\vec{\nabla} P) = 0 \end{cases}$$

Finally, equation (3.7) becomes

$$\frac{\partial \vec{\bar{\zeta}}}{\partial \bar{t}} + rot(\vec{\bar{\zeta}} \wedge \vec{\bar{V}}) = 0 \tag{3.8}$$

and:

$$rot(\vec{\vec{\zeta}} \wedge \vec{\vec{V}}) = (\vec{\vec{V}} \cdot \vec{\nabla})\vec{\vec{\zeta}} - (\vec{\vec{\zeta}} \cdot \vec{\nabla})\vec{\vec{V}} + \vec{\vec{\zeta}}(\vec{\nabla} \cdot \vec{\vec{V}}) - \vec{\vec{V}}(\vec{\nabla} \cdot \vec{\vec{\zeta}}) \tag{3.9}$$

Because of the fluid is incompressible, from equation (3.3), we have

$$\vec{\nabla} \cdot \vec{\vec{V}} = 0$$

and it is known that the divergence of the curl is 0, then

$$\vec{\nabla} \cdot \vec{\vec{\zeta}} = \vec{\nabla} \cdot (\vec{\nabla} \times \vec{\vec{V}}) = 0$$

Therefore, expression (3.9) now becomes

$$\frac{\partial \vec{\vec{\zeta}}}{\partial \bar{t}} + (\vec{\vec{V}} \cdot \vec{\nabla})\vec{\vec{\zeta}} - (\vec{\vec{\zeta}} \cdot \vec{\nabla})\vec{\vec{V}} = 0 \tag{3.10}$$

For the two dimensional flow, one have

$$\begin{cases} \vec{\vec{V}} = \bar{V}_r \vec{e}_r + \bar{V}_\theta \vec{e}_\theta \\ \vec{\vec{\zeta}} = \bar{\zeta}(\bar{r}, \theta)\vec{z} \end{cases}$$

Then the equation (3.10) can be expanded as

$$\begin{pmatrix} 0 \\ 0 \\ \dfrac{\partial \bar{\zeta}(\bar{r}, \theta)}{\partial \bar{t}} \end{pmatrix} + \left(\bar{V}_r \frac{\partial}{\partial \bar{r}} + \frac{\bar{V}_\theta}{\bar{r}} \frac{\partial}{\partial \theta} \right) \begin{pmatrix} 0 \\ 0 \\ \bar{\zeta}(\bar{r}, \theta) \end{pmatrix} - \frac{\partial \bar{\zeta}(\bar{r}, \theta)}{\partial \bar{z}} \begin{pmatrix} \bar{V}_r \\ \bar{V}_\theta \\ 0 \end{pmatrix} = \begin{pmatrix} 0 \\ 0 \\ 0 \end{pmatrix} \tag{3.11}$$

As the flow is two dimensional, the only equation component of interest in equation (3.11) is the axial direction and the equation can be expressed in the form:

$$\frac{\partial \bar{\zeta}(\bar{r}, \theta)}{\partial \bar{t}} + \bar{V}_r \frac{\partial \bar{\zeta}(\bar{r}, \theta)}{\partial \bar{r}} + \frac{\bar{V}_\theta}{\bar{r}} \frac{\partial \bar{\zeta}(\bar{r}, \theta)}{\partial \theta} = 0 \tag{3.12}$$

One can also note that:

$$\bar{\zeta} = \nabla \times \vec{\vec{V}} = \frac{1}{\bar{r}} \frac{\partial (\bar{r} \bar{V}_\theta)}{\partial \bar{r}} - \frac{1}{\bar{r}} \frac{\partial \bar{V}_r}{\partial \theta} \tag{3.13}$$

Collecting equations (3.3), (3.5), (3.6), (3.12) and (3.13), a set of basic equation is then proposed:

$$\frac{\partial (\bar{r} \bar{V}_r)}{\partial \bar{r}} + \frac{\partial \bar{V}_\theta}{\partial \theta} = 0 \tag{3.14a}$$

$$\bar{\rho} \left[\frac{\partial \bar{V}_r}{\partial \bar{t}} + \bar{V}_r \frac{\partial \bar{V}_r}{\partial \bar{r}} + \frac{\bar{V}_\theta}{\bar{r}} \frac{\partial \bar{V}_r}{\partial \theta} - \frac{\bar{V}_\theta^2}{\bar{r}} \right] = -\frac{\partial \bar{P}}{\partial \bar{r}} \tag{3.14b}$$

$$\bar{\rho} \left[\frac{\partial \bar{V}_\theta}{\partial \bar{t}} + \bar{V}_r \frac{\partial \bar{V}_\theta}{\partial \bar{r}} + \frac{\bar{V}_\theta}{\bar{r}} \frac{\partial \bar{V}_\theta}{\partial \theta} + \frac{\bar{V}_r \bar{V}_\theta}{\bar{r}} \right] = -\frac{1}{\bar{r}} \frac{\partial \bar{P}}{\partial \theta} \tag{3.14c}$$

$$\frac{\partial \bar{\zeta}(\bar{r},\theta)}{\partial \bar{t}} + \bar{V}_r \frac{\partial \bar{\zeta}(\bar{r},\theta)}{\partial \bar{r}} + \frac{\bar{V}_\theta}{\bar{r}} \frac{\partial \bar{\zeta}(\bar{r},\theta)}{\partial \theta} = 0 \tag{3.14d}$$

$$\bar{\zeta} = \frac{1}{\bar{r}} \frac{\partial (\bar{r}\bar{V}_\theta)}{\partial \bar{r}} - \frac{1}{\bar{r}} \frac{\partial \bar{V}_r}{\partial \theta} \tag{3.14e}$$

The basic solutions of equations (3.14a – 3.14e), for a steady flow, are associated with the assigned flow condition:

$$\bar{V}_r = \frac{\bar{Q}}{2\pi\bar{r}}, \bar{V}_\theta = \frac{\bar{\Gamma}}{2\pi\bar{r}},\ \bar{\zeta}_B = 0 \text{ and } \bar{P}_B = -\frac{\bar{\rho}}{8\pi^2}(\bar{Q}^2 + \bar{\Gamma}^2)(\frac{1}{\bar{r}^2} - \frac{1}{\bar{r}_4^2})$$

where $\bar{\Gamma}$ is the circulation of the upstream impeller, which is defined as

$$\bar{\Gamma} = \oint \bar{V}_\theta \, d\vec{S} = 2\pi \bar{r} \bar{V}_\theta \tag{3.15}$$

According to the velocity triangle at the impeller outlet

$$\bar{V}_{2\theta} = \bar{U}_2 - \frac{\bar{Q}}{2\pi\bar{r}_2}\cot\beta_2 \tag{3.16}$$

Therefore, the circulation from impeller outlet is

$$\bar{\Gamma} = 2\pi\bar{r}_2(\bar{U}_2 - \frac{\bar{Q}}{2\pi\bar{r}_2}\cot\beta_2)$$

3.3.2 Dimensionless form

To obtain the linear analysis in dimensionless form, the quantities $\bar{r}_3$, $\frac{2\pi\bar{r}_3^2}{Q}$, $\frac{Q}{2\pi\bar{r}_3}$, $\frac{Q}{2\pi\bar{r}_3^2}$, and $\frac{\bar{\rho}Q^2}{(2\pi\bar{r}_3)^2}$ are introduced to scale the quantities of length, time, velocity, vorticity and pressure respectively, and then the following dimensionless quantities are obtained: $r = \frac{\bar{r}}{\bar{r}_3}$, $t = \frac{Q}{2\pi\bar{r}_3^2}$, $\vec{V} = \frac{2\pi\bar{r}_3}{Q}\vec{\bar{V}}$, $\zeta = \frac{2\pi\bar{r}_3^2}{Q}\bar{\zeta}$, $P = \frac{(2\pi\bar{r}_3)^2}{\bar{\rho}Q^2}\bar{P}$, and the basic equation set (3.14a-3.14e) becomes :

$$\frac{\partial (rV_r)}{\partial r} + \frac{\partial V_\theta}{\partial \theta} = 0 \tag{3.17a}$$

$$\frac{\partial V_r}{\partial t} + V_r \frac{\partial V_r}{\partial r} + \frac{V_\theta}{r}\frac{\partial V_r}{\partial \theta} - \frac{V_\theta^2}{r} = -\frac{\partial P}{\partial r} \tag{3.17b}$$

$$\frac{\partial V_\theta}{\partial t} + V_r \frac{\partial V_\theta}{\partial r} + \frac{V_\theta}{r}\frac{\partial V_\theta}{\partial \theta} + \frac{V_r V_\theta}{r} = -\frac{1}{r}\frac{\partial P}{\partial \theta} \tag{3.17c}$$

$$\frac{\partial \zeta}{\partial t} + V_r \frac{\partial \zeta}{\partial r} + \frac{V_\theta}{r}\frac{\partial \zeta}{\partial \theta} = 0 \tag{3.17d}$$

$$\zeta = \frac{1}{r}\frac{\partial (rV_\theta)}{\partial r} - \frac{1}{r}\frac{\partial V_r}{\partial \theta} \tag{3.17e}$$

where $1 \le r \le R = \frac{\bar{r}_4}{\bar{r}_3}$, and the corresponding dimensionless solutions for steady flow are: $V_r = \frac{1}{r}$, $V_\theta = \frac{\Gamma}{Q}\frac{1}{r}$, $\zeta_B = 0$ and $P_B = -\frac{1}{2}\left(1+\frac{\Gamma^2}{Q^2}\right)\left(\frac{1}{r^2}-\frac{1}{R^2}\right)$. We then define $\mu = \frac{\Gamma}{Q}$ to represent $\frac{1}{\tan\alpha}$ in the following, where α is the absolute flow angle in the vaneless diffuser, as shown in Figure 3.2.

3.3.3 Linearization

As it is classically done in linear stability analysis, the perturbed flow will be represented as a superposition of steady and unsteady flow. Therefore, the flow in the vaneless diffuser will be now represented by the sum of the steady flow (the basic solutions) and a small unsteady disturbance, as shown in the following,

$$\begin{cases} V_r = \dfrac{1}{r} + \varepsilon u_r(r,\theta,t) \\ V_\theta = \dfrac{\mu}{r} + \varepsilon u_\theta(r,\theta,t) \\ \zeta = 0 + \varepsilon\zeta(r,\theta,t) \\ P = P_B + \varepsilon p(r,\theta,t) \end{cases}$$

where $\varepsilon << 1$.

Introducing the above expressions into the equation set (3.17a-3.17e) and keeping only the terms with first order of ε, the linear equations for the small perturbation (u_r, u_θ, ζ and p) are obtained

$$\frac{\partial (ru_r)}{\partial r} + \frac{\partial u_\theta}{\partial \theta} = 0 \tag{3.18a}$$

$$\frac{\partial u_r}{\partial t} - \frac{u_r}{r^2} + \frac{1}{r}\frac{\partial u_r}{\partial r} + \frac{\mu}{r^2}\frac{\partial u_r}{\partial \theta} - \frac{2\mu}{r^2}u_\theta = -\frac{\partial p}{\partial r} \tag{3.18b}$$

$$\frac{\partial u_\theta}{\partial t} + \frac{1}{r}\frac{\partial u_\theta}{\partial r} + \frac{1}{r^2}u_\theta + \frac{\mu}{r^2}\frac{\partial u_\theta}{\partial \theta} = -\frac{1}{r}\frac{\partial p}{\partial \theta} \tag{3.18c}$$

$$\frac{\partial \zeta}{\partial t} + \frac{1}{r}\frac{\partial \zeta}{\partial r} + \frac{\mu}{r^2}\frac{\partial \zeta}{\partial \theta} = 0 \tag{3.18d}$$

$$\zeta = \frac{1}{r}\frac{\partial (ru_\theta)}{\partial r} - \frac{1}{r}\frac{\partial u_r}{\partial \theta} \tag{3.18e}$$

3.3.4 Normal Modes Analysis

The quantities of the perturbation in the form of normal modes can be written as:

$$\{u_r, u_\theta, \zeta, p\}(r,\theta,t) = A\{\tilde{u}_r, \tilde{u}_\theta, \tilde{\zeta}, \tilde{p}\}(r)e^{i\omega t - in\theta} \tag{3.19}$$

Where n is the number of modes, which represents the number of rotating stall cells in the experiment, A is a constant which represents the amplitude of the linear mode. The complex pulsation ω could be divided in a real and complex part $\omega = \omega_{real} - i\sigma$. Physically, the real part ω_{real} is the angular velocity and σ is the growth rate of the instability which determines if the mode is stable, or not.

$$\begin{cases} \sigma > 0 \text{, the flow is unstable} \\ \sigma = 0 \text{, the flow is at neutral stability} \\ \sigma < 0 \text{, the flow is stable} \end{cases}$$

Therefore, the neutral stability state can be obtained by setting $\sigma = 0$ to have the characteristics of the rotating instability at the critical condition. Introducing the normal mode expressions (3.19) into equations (3.18a – 3.18e), the following equations are obtained:

$$\frac{\partial(r\tilde{u}_r)}{\partial r} - in\tilde{u}_\theta = 0 \tag{3.20a}$$

$$i\omega\tilde{u}_r - \frac{1}{r^2}\tilde{u}_r + \frac{1}{r}\frac{\partial\tilde{u}_r}{\partial r} - \frac{in\mu}{r^2}\tilde{u}_r - \frac{2\mu}{r^2}\tilde{u}_\theta = -\frac{\partial\tilde{p}}{\partial r} \tag{3.20b}$$

$$i\omega\tilde{u}_\theta + \frac{1}{r}\frac{\partial\tilde{u}_\theta}{\partial r} + \frac{1}{r^2}\tilde{u}_\theta - in\frac{\mu}{r^2}\tilde{u}_\theta = \frac{1}{r}in\tilde{p} \tag{3.20c}$$

$$i\omega\tilde{\zeta} + \frac{1}{r}\frac{\partial\tilde{\zeta}}{\partial r} - in\frac{\mu}{r^2}\tilde{\zeta} = 0 \tag{3.20d}$$

$$\tilde{\zeta} = \frac{1}{r}\frac{\partial(r\tilde{u}_\theta)}{\partial r} + \frac{in}{r}\tilde{u}_r \tag{3.20e}$$

3.3.5 Solutions of linear stability analysis

From equation (3.20d), it becomes

$$\frac{\partial\tilde{\zeta}}{\partial r} = \tilde{\zeta}\left(\frac{in\mu}{r} - i\omega r\right) \tag{3.21}$$

Then the general solution of equation (3.21) is

$$\tilde{\zeta}(r) = Ce^{-\frac{i\omega}{2}(r^2-1)+in\mu\ln r} \tag{3.22}$$

where C is a constant given by

$$\hat{\zeta}(r=1,\theta,t) = \tilde{\zeta}(1)e^{i\omega t - in\theta} = Ce^{i\omega t - in\theta} \Rightarrow C = \tilde{\zeta}(1) \tag{3.23}$$

If the solution (3.22) is used in equation (3.20e), that is

$$Ce^{-\frac{i\omega}{2}(r^2-1)+in\mu\ln r}=\frac{1}{r}\frac{\partial(r\tilde{u}_\theta)}{\partial r}+\frac{in}{r}\tilde{u}_r \tag{3.24}$$

with equation (3.24) and equation (3.20a), a solution represented by the two following equations can be proposed:

$$\begin{cases}\tilde{u}_r=a_1F+a_2G\\ \tilde{u}_\theta=b_1F+b_2G\end{cases} \tag{3.25}$$

where F and G are two arbitrary functions, and a_1, a_2, b_1, b_2 are the constants which need to be determined. One then obtained

$$\begin{cases} a_1\dfrac{\partial(rF)}{\partial r}+a_2\dfrac{\partial(rG)}{\partial r}-inb_1F-inb_2G=0\\ b_1\dfrac{\partial(rF)}{\partial r}+b_2\dfrac{\partial(rG)}{\partial r}+ina_1F+ina_2G=Cre^{-\frac{i\omega}{2}(r^2-1)+in\mu\ln r}\end{cases} \tag{3.26}$$

The first equation in (3.26) can be rewritten as

$$\frac{\partial(rF)}{\partial r}=-\frac{a_2}{a_1}\frac{\partial(rG)}{\partial r}+in\frac{b_1}{a_1}F+in\frac{b_2}{a_1}G \tag{3.27}$$

The term $\dfrac{\partial(rF)}{\partial r}$ is replaced in the second equation of (3.26) by using the expression (3.27), then we have

$$\frac{\partial(rG)}{\partial r}(b_2-\frac{b_1a_2}{a_1})+inG(a_2+\frac{b_1b_2}{a_1})+inF(a_1+\frac{b_1^2}{a_1})=Cre^{-\frac{i\omega}{2}(r^2-1)+in\mu\ln r} \tag{3.28}$$

in the same manner, one can get

$$\frac{\partial(rG)}{\partial r}=-\frac{a_1}{a_2}\frac{\partial(rF)}{\partial r}+in\frac{b_1}{a_2}F+in\frac{b_2}{a_2}G \tag{3.29}$$

$$\frac{\partial(rF)}{\partial r}(b_1-\frac{b_2a_1}{a_2})+inF(a_1+\frac{b_1b_2}{a_2})+inG(a_2+\frac{b_2^2}{a_2})=Cre^{-\frac{i\omega}{2}(r^2-1)+in\mu\ln r} \tag{3.30}$$

The orthogonality condition of equations (3.27) and (3.29) leads to

$$\begin{cases}a_1+\dfrac{b_1^2}{a_1}=0\\ a_2+\dfrac{b_2^2}{a_2}=0\end{cases}\rightarrow\begin{cases}a_1^2+b_1^2=0\\ a_2^2+b_2^2=0\end{cases} \tag{3.31}$$

One of the solutions of these equations is proposed:

$$\begin{cases} a_1 = -i, b_1 = 1 \\ a_2 = -i, b_2 = -1 \end{cases} \tag{3.32}$$

and equations (3.28) and (3.30) become

$$\begin{cases} -2\dfrac{\partial(rG)}{\partial r} + 2nG = Cre^{-\frac{i\omega}{2}(r^2-1)+in\mu\ln r} \\ 2\dfrac{\partial(rF)}{\partial r} + 2nF = Cre^{-\frac{i\omega}{2}(r^2-1)+in\mu\ln r} \end{cases} \tag{3.33}$$

The general solutions of F and G are the sum of a particular solution for the nonhomogeneous equation and a solution for the homogeneous equation. Therefore, the solutions can be written as

$$\begin{cases} F = F_p(r) + F_h(r) \\ G = G_p(r) + G_h(r) \end{cases} \tag{3.34}$$

where the subscript p represents particular solution and h represents the solution for the homogeneous equation. For the particular solution, we propose the following solution,

$$\begin{cases} F_p(r) = \dfrac{1}{2}C\int_1^r e^{-\frac{i\omega}{2}(r_0^2-1)+in\mu\ln r_0}\left(\dfrac{r_0}{r}\right)^{n+1}dr_0 \\ G_p(r) = \dfrac{1}{2}C\int_r^R e^{-\frac{i\omega}{2}(r_0^2-1)+in\mu\ln r_0}\left(\dfrac{r}{r_0}\right)^{n-1}dr_0 \end{cases} \tag{3.35}$$

For another solution, the corresponding homogeneous equations are,

$$\begin{cases} -\dfrac{\partial(rG)}{\partial r} + nG = 0 \\ \dfrac{\partial(rF)}{\partial r} + nF = 0 \end{cases} \tag{3.36}$$

Then, the solutions can be easily obtained,

$$\begin{cases} F_h(r) = \dfrac{C_1}{r^{n+1}} \\ G_h(r) = C_2 r^{n-1} \end{cases} \tag{3.37}$$

Finally, the solutions of F and G are

$$\begin{cases} F = F_p(r) + F_h(r) = \dfrac{1}{2}C\int_1^r e^{-\frac{i\omega}{2}(r_0^2-1)+in\mu\ln r_0}\left(\dfrac{r_0}{r}\right)^{n+1}dr_0 + \dfrac{C_1}{r^{n+1}} \\ G = G_p(r) + G_h(r) = \dfrac{1}{2}C\int_r^R e^{-\frac{i\omega}{2}(r_0^2-1)+in\mu\ln r_0}\left(\dfrac{r}{r_0}\right)^{n-1}dr_0 + C_2 r^{n-1} \end{cases} \tag{3.38}$$

Then equation (3.25) becomes

$$\begin{cases} \tilde{u}_r = -i\left\{C(F^{\zeta}+G^{\zeta})+\dfrac{C_1}{r^{n+1}}+C_2 r^{n-1}\right\} \\ \tilde{u}_\theta = C(F^{\zeta}-G^{\zeta})+\dfrac{C_1}{r^{n+1}}-C_2 r^{n-1} \end{cases} \tag{3.39}$$

with

$$\begin{cases} F^{\zeta}(r) = \dfrac{1}{2}\displaystyle\int_1^r e^{-\frac{i\omega}{2}(r_0^2-1)+in\mu\ln r_0}\left(\frac{r_0}{r}\right)^{n+1} dr_0 \\ G^{\zeta}(r) = \dfrac{1}{2}\displaystyle\int_r^R e^{-\frac{i\omega}{2}(r_0^2-1)+in\mu\ln r_0}\left(\frac{r}{r_0}\right)^{n-1} dr_0 \end{cases} \tag{3.40}$$

To determine the values of the two constants: C_1 and C_2, the boundary conditions of the disturbance at the diffuser inlet $r = 1$ are used, that is

$$\tilde{u}_r(r=1) = \tilde{u}_\theta(r=1) = 0 \tag{3.41}$$

Therefore:

$$\begin{cases} \tilde{u}_r(r=1) = -i\left\{C(F^{\zeta}(r=1)+G^{\zeta}(r=1))+C_1+C_2\right\} = 0 \\ \tilde{u}_\theta(r=1) = C(F^{\zeta}(r=1)-G^{\zeta}(r=1))+C_1-C_2 = 0 \end{cases} \tag{3.42}$$

and as $F^{\zeta}(r=1) = 0$ from expression (3.40),

$$\begin{cases} C_1 = 0 \\ C_2 = -CG^{\zeta}(r=1) \end{cases} \tag{3.43}$$

Finally, $\tilde{u}_r$ and $\tilde{u}_\theta$ are written as

$$\begin{cases} \tilde{u}_r = -iC\left\{F^{\zeta}+G^{\zeta}-G^{\zeta}(r=1)r^{n-1}\right\} \\ \tilde{u}_\theta = C\left\{F^{\zeta}-G^{\zeta}+G^{\zeta}(r=1)r^{n-1}\right\} \end{cases} \tag{3.44}$$

The outlet of the vaneless diffuser is directly connected with the atmosphere, thus the boundary condition at diffuser outlet: $\tilde{p}(r=R) = 0$ is obtained. The equation (3.20c) becomes,

$$i\omega\tilde{u}_\theta(r=R)+\frac{1}{r}\frac{\partial\tilde{u}_\theta}{\partial r}(r=R)+\frac{1}{r^2}\tilde{u}_\theta(r=R)-in\frac{\mu}{r^2}\tilde{u}_\theta(r=R) = 0 \tag{3.45}$$

The above expression may be simplified by taking into account equation (3.20e) which gives:

$$\frac{1}{R}\frac{\partial\tilde{u}_\theta}{\partial r}(r=R) = \frac{1}{R}\tilde{\zeta}(r=R)-\frac{1}{R^2}\tilde{u}_\theta(r=R)-\frac{in}{R^2}\tilde{u}_r(r=R) \tag{3.46}$$

Expression (3.46) is introduced into (3.45), and the following dispersion equation is obtained.

$$i\omega\tilde{u}_\theta(r=R)+\frac{1}{R}\tilde{\zeta}(r=R)-\frac{in}{R^2}\tilde{u}_r(r=R)-in\mu\frac{\tilde{u}_\theta(r=R)}{R^2} = 0 \tag{3.47}$$

in which $\tilde{u}_r(r=R)$, $\tilde{u}_\theta(r=R)$ and $\tilde{\zeta}(r=R)$ can be determined from equations (3.22), (3.40), and (3.44), which reorganized as follows:

$$\begin{cases} \tilde{\zeta}(r) = Ce^{-\frac{i\omega}{2}(r^2-1)+in\mu\ln r} \\ \tilde{u}_r = -iC\left\{F^\zeta + G^\zeta - G^\zeta(r=1)r^{n-1}\right\} \\ \tilde{u}_\theta = C\left\{F^\zeta - G^\zeta + G^\zeta(r=1)r^{n-1}\right\} \end{cases}$$
$$\begin{cases} F^\zeta(r) = \frac{1}{2}\int_1^r e^{-\frac{i\omega}{2}(r_0^2-1)+in\mu\ln r_0}\left(\frac{r_0}{r}\right)^{n+1}dr_0 \\ G^\zeta(r) = \frac{1}{2}\int_r^R e^{-\frac{i\omega}{2}(r_0^2-1)+in\mu\ln r_0}\left(\frac{r}{r_0}\right)^{n-1}dr_0 \end{cases} \tag{3.48}$$

3.4 Results of linear stability analysis

3.4.1 Critical flow angle and propagation velocity

The dispersion equation (3.47) is the function of *n*, *R*, μ, ω_{real} and σ. To estimate the characteristics of rotating instability at critical condition, $\sigma = 0$ is prescribed, then with the specified stall mode which represented by *n* and vaneless diffuser which represented by *R*, the critical flow angle (represented by μ) and angular frequency (ω_{real}) of rotating stall can be determined by giving proper initial values. The mathematical calculations were realized by the commercial software Mathematica, the processing is given in Figure 3.3. The results are given in Table 3.1 and Table 3.2, in which

$$\alpha = \arctan\frac{1}{\mu}$$

$$\frac{V_p}{V_{\theta 2}} = \frac{\omega_{real}/n}{\mu}$$

Table 3.1 Critical flow angle for different parameters

n	α (°)			
	R = 1.5	*R* = 2	*R* = 2.5	*R* = 3
1	3.62	8.16	11.76	14.55
2	6.60	13.76	18.98	22.89
3	8.66	16.40	21.40	24.80
4	9.84	16.76	19.68	18.20

Table 3.2 Critical propagation velocity for different parameters

n	$V_p/V_{\theta 2}$			
	R = 1.5	R = 2	R = 2.5	R = 3
1	0.20	0.014	– 0.04	– 0.05
2	0.24	0.088	0.042	0.024
3	0.29	0.16	0.11	0.08
4	0.34	0.22	0.17	0.18

$\sigma = 0$, R = 1.5, 2, 2.5 and 3, n = 1, 2, 3 and 4

With initial value of μ and ω_{real}

$$\begin{cases} \tilde{\zeta}(r) = Ce^{\frac{i\omega}{2}(r^2-1)+in\mu\ln r} \\ \tilde{u}_r = -iC\left\{F^{\zeta} + G^{\zeta} - G^{\zeta}(r=1)r^{n-1}\right\} \\ \tilde{u}_\theta = C\left\{F^{\zeta} - G^{\zeta} + G^{\zeta}(r=1)r^{n-1}\right\} \end{cases}$$

$$\begin{cases} F^{\zeta}(r) = \frac{1}{2}\int_1^r e^{-\frac{i\omega}{2}(r_0^2-1)+in\mu\ln r_0}\left(\frac{r_0}{r}\right)^{n+1}dr_0 \\ G^{\zeta}(r) = \frac{1}{2}\int_r^R e^{-\frac{i\omega}{2}(r_0^2-1)+in\mu\ln r_0}\left(\frac{r}{r_0}\right)^{n-1}dr_0 \end{cases}$$

$$i\omega\tilde{u}_\theta(r=R) + \frac{1}{R}\tilde{\zeta}(r=R) - \frac{in}{R^2}\tilde{u}_r(r=R) - in\mu\frac{\tilde{u}_\theta(r=R)}{R^2} = 0$$

$\mu = (\,)$, $\omega_{real} = (\,)$

Figure 3.3 Calculation process of μ and ω_{real} by Mathematica

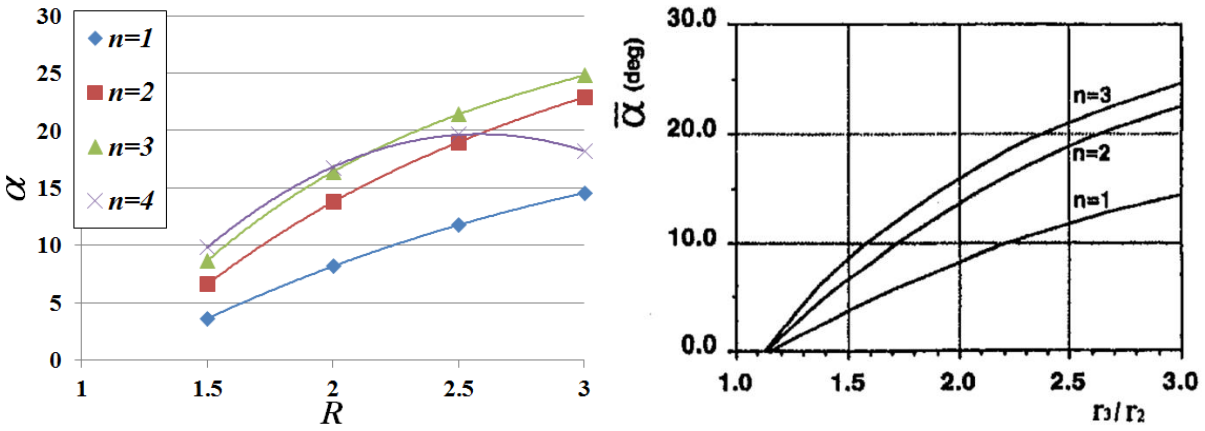

(a) Comparison of the critical flow angle

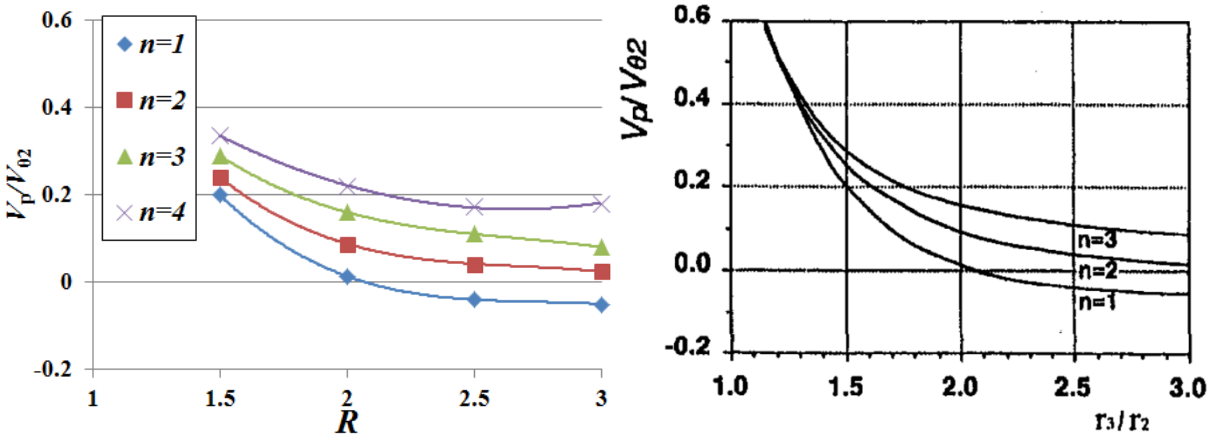

(b) Comparison of the critical propagation velocity

Figure 3.4 Comparisons between present results and Tsujimoto et al (1996)

In order to verify the present linear model, the characteristics of rotating stall are plotted and compared to the results presented by Tsujimoto et al (1996), as shown in Figure 3.4. It can be seen that good agreements obtained for the presented stall modes: n = 1, 2 and 3, and the general tendencies can be concluded as follows

(1) The critical flow angle increases with the increase of diffuser radius ratio.

(2) The propagation velocity decreases with the increase of diffuser radius ratio.

(3) For stall modes n = 1, 2 and 3, the more of the number of stall cells, the larger of the critical flow angle and the higher of the propagation velocity.

The last conclusion is only true for the modes presented in both studies: n = 1, 2 and 3, the different behavior of the critical angle versus diffuser radius ratio, obtained when the number of stall cells is 4, has already been reported by Ljevar (2007), as shown in Figure 3.5.

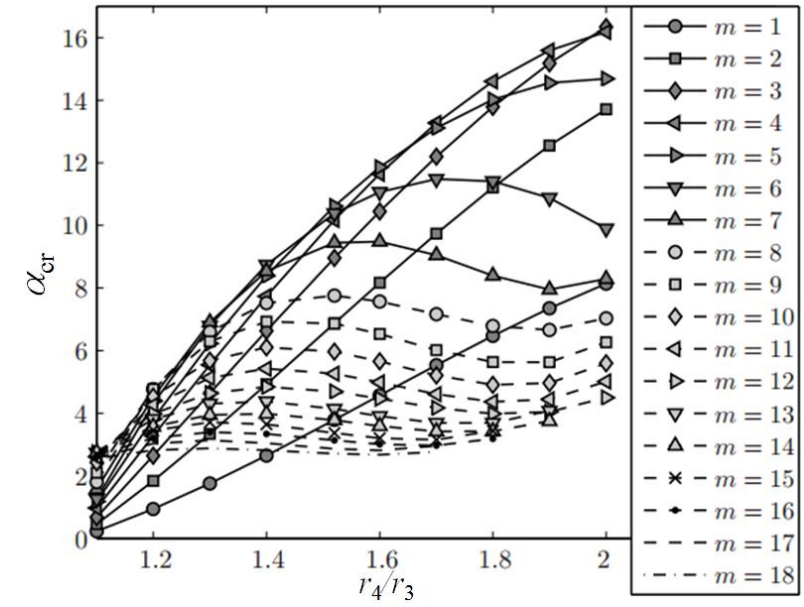

(a)

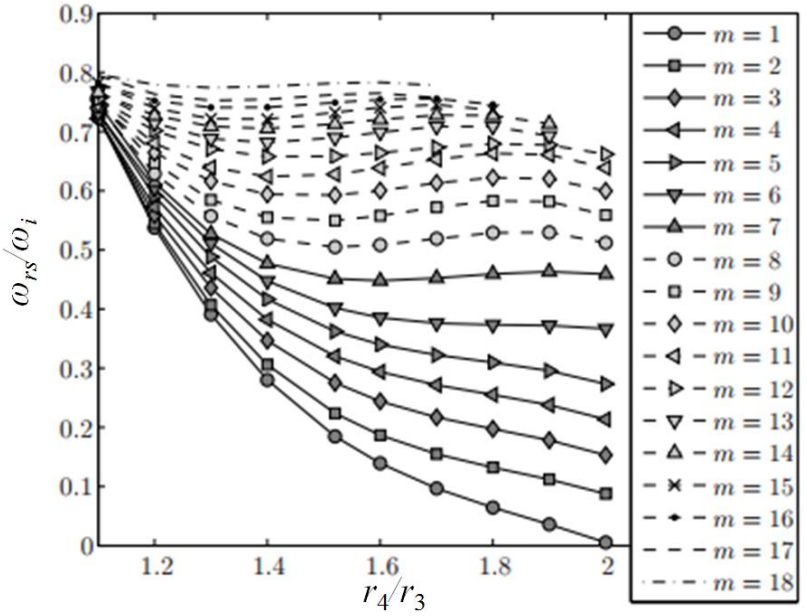

(b)

Figure 3.5 Critical flow angle (a) and propagation velocity (b) versus the diffuser radius ratio (Ljevar, 2007)

3.4.2 The growth rate of stall mode

Although the linear stability analysis presented by Tsujimoto et al (1996) has provided quantitative information on the stability analysis, the theoretical predictions are limited to the neutral stability regime only. For example, Figure 3.6 (Tsujimoto et al, 1996) gives the comparisons of critical flow angle and propagation velocity between the theoretical results and experimental results. It can be seen that for each configuration, it gives only the result at critical point, while the experimental results reported continuous propagation velocity since the flow angle beyond the critical limit of rotating stall. Therefore, the results of Tsujimoto et al (1996) did not show the characteristic of rotating stall at stall conditions.

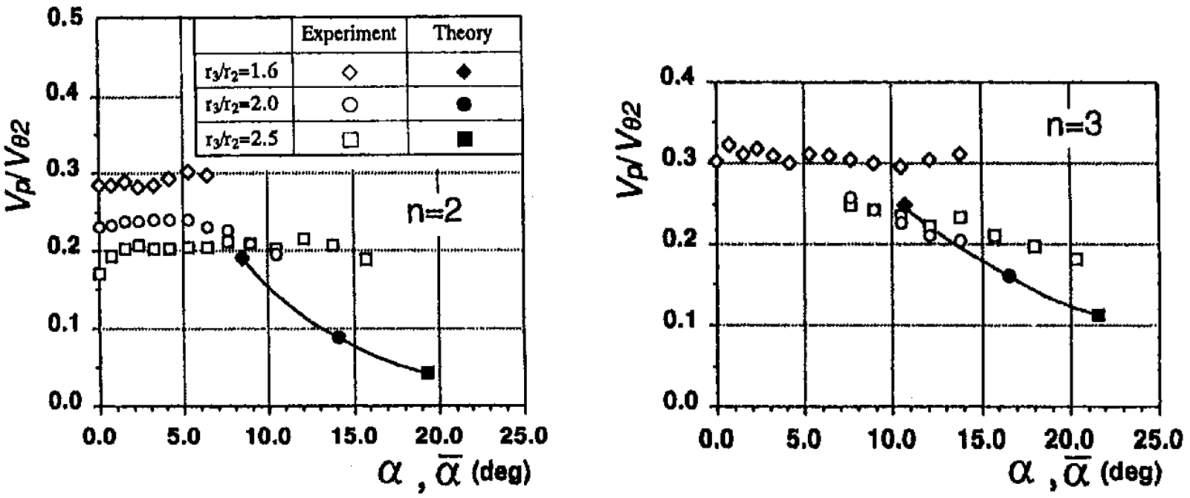

Figure 3.6 Comparisons of critical flow angle and propagation velocity with experiments (Tsujimoto et al, 1996)

Since the comparisons shown in Figure 3.6 are not enough to reveal the characteristics of rotating stall at unstable conditions, the present study extended the analysis to unstable flow conditions (with a positive growth rate of instability). More precisely, the dependence of the propagation velocity and the growth rate on the flow angle will be examined for different fixed diffuser radius ratio R and different fixed number of stall modes n. In addition, as we have observed different stall modes in the experiment, then the growth rate of each stall mode will be compared to determine the dominant stall mode.

In Figure 3.3, we have determined the critical flow angle and propagation velocity for fixed n and R. In the same manner, if we decrease the flow angle ($\mu > \mu_c$) from the critical value, which means the operating condition moves to unstable regime, then the growth rate σ and the corresponding propagation velocity ω_{real} of each stall mode at unstable conditions can be obtained if μ, R and n are given. The processing is described in Figure 3.7.

The computed values of the growth rate σ, for assigned number of modes n and diffuser radius ratio R are reported in Figure 3.8. In this figure, σ is plotted versus α for $R = 2$ and $R = 2.5$ with $n = 1$, $n = 2$, $n = 3$ and $n = 4$. The plots in Figure 3.8 show that the growth rate changes from negative for $\alpha > \alpha_c$ to positive for $\alpha < \alpha_c$, where α_c is the critical angle at the onset of instability. Another information gathered from Figure 3.8 is that, for any given pair (R, α) with $\alpha < \alpha_c$, the comparison of the growth rates associated with different modes of instability indicates that there exists a maximum growth rate σ corresponding to a particular rotating stall mode n.

There is an intrinsic physical interest in determining the fastest growing linear mode for given values of R and α. In fact, with $\sigma_{max} > 0$, the spatial periodicity of this mode, namely $2\pi/n$, likely determines the number of stall cells. Depending on the flow angle α, the number of stall cells corresponding to a maximum growth rate σ_{max} is indicated in Figure 3.8 for two geometric configurations with $R = 2$ and $R = 2.5$. A close inspection of this figure shows that, generally, the growth rate associated with the mode $n = 1$ is always smaller than the nearly similar growth rate of the modes $n = 2$, 3, and 4, this is confirmed by the experiment of that

mode $n = 1$ is the weakest stall mode which can be neglected. With the decrease of flow angle, for the case $R = 2$, the fastest growing (dominant) stall modes are $n = 4 \rightarrow n = 3 \rightarrow n = 4$, while for case $R = 2.5$, they are $n = 3 \rightarrow n = 2 \rightarrow n = 4$.

$\mu > \mu_c$, R=1.5, 2, 2.5 and 3, n=1, 2, 3 and 4

With initial value of σ and ω_{real}

$$\begin{cases} \tilde{\zeta}(r) = Ce^{\frac{i\omega}{2}(r^2-1)+in\mu\ln r} \\ \tilde{u}_r = -iC\left\{F^{\zeta} + G^{\zeta} - G^{\zeta}(r=1)r^{n-1}\right\} \\ \tilde{u}_\theta = C\left\{F^{\zeta} - G^{\zeta} + G^{\zeta}(r=1)r^{n-1}\right\} \end{cases}$$

$$\begin{cases} F^{\zeta}(r) = \frac{1}{2}\int_1^r e^{-\frac{i\omega}{2}(r_0^2-1)+in\mu\ln r_0}\left(\frac{r_0}{r}\right)^{n+1}dr_0 \\ G^{\zeta}(r) = \frac{1}{2}\int_r^R e^{-\frac{i\omega}{2}(r_0^2-1)+in\mu\ln r_0}\left(\frac{r}{r_0}\right)^{n-1}dr_0 \end{cases}$$

$$i\omega\tilde{u}_\theta(r=R) + \frac{1}{R}\tilde{\zeta}(r=R) - \frac{in}{R^2}\tilde{u}_r(r=R) - in\mu\frac{\tilde{u}_\theta(r=R)}{R^2} = 0$$

$\sigma = (\,)$, $\omega_{real} = (\,)$

Figure 3.7 Calculation of σ and ω_{real} by Mathematica

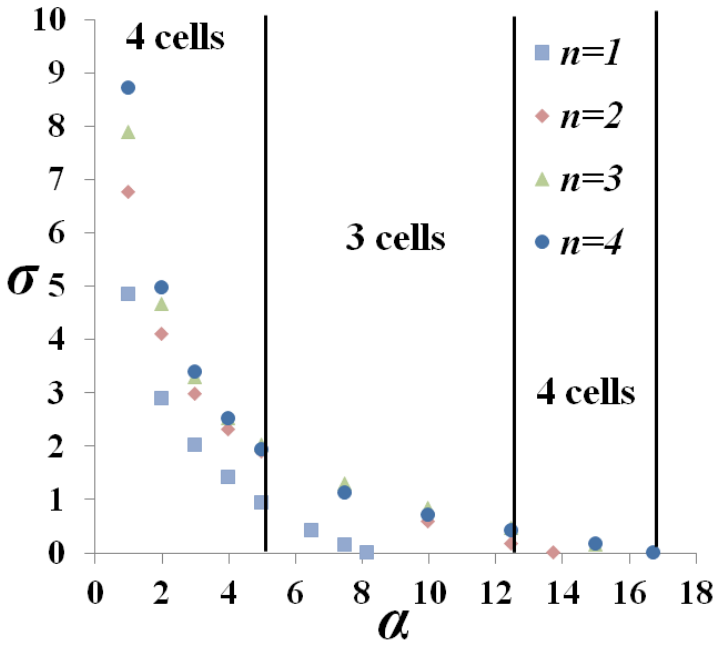

(a) $R = 2$

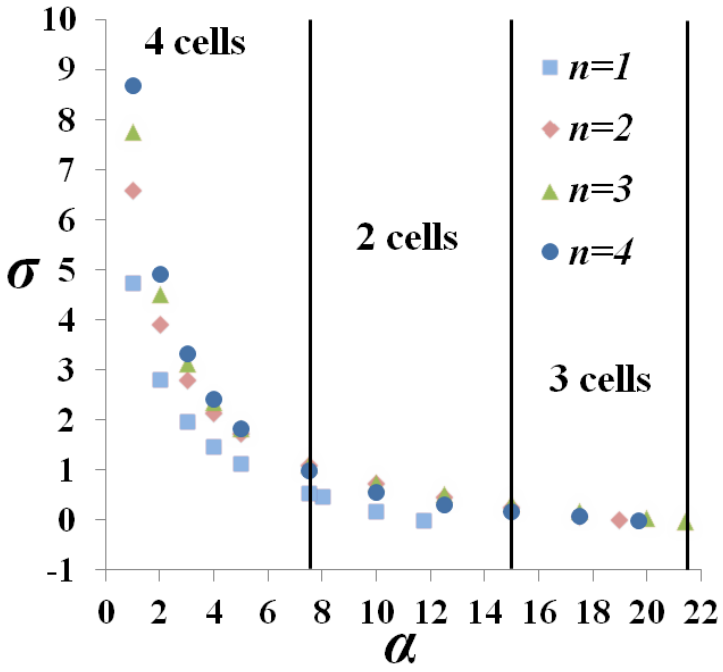

(b) R = 2.5

Figure 3.8 Growth rates of instabilities for different cases

Figure 3.9 depicts the dependence on the flow angle of the propagation velocity $V_p/V_{\theta 2}$ for R = 2 and R = 2.5 at unstable conditions. As it can be seen from this figure, the propagation velocity in the unstable region is a decreasing function of α for a fixed number of stall cells and an increasing function of n for a fixed flow angle.

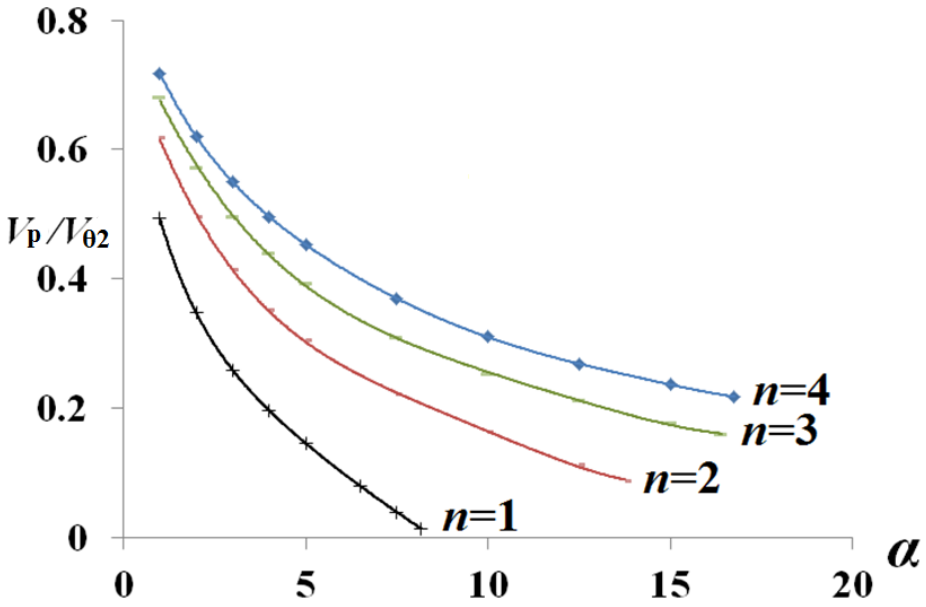

(a) R = 2

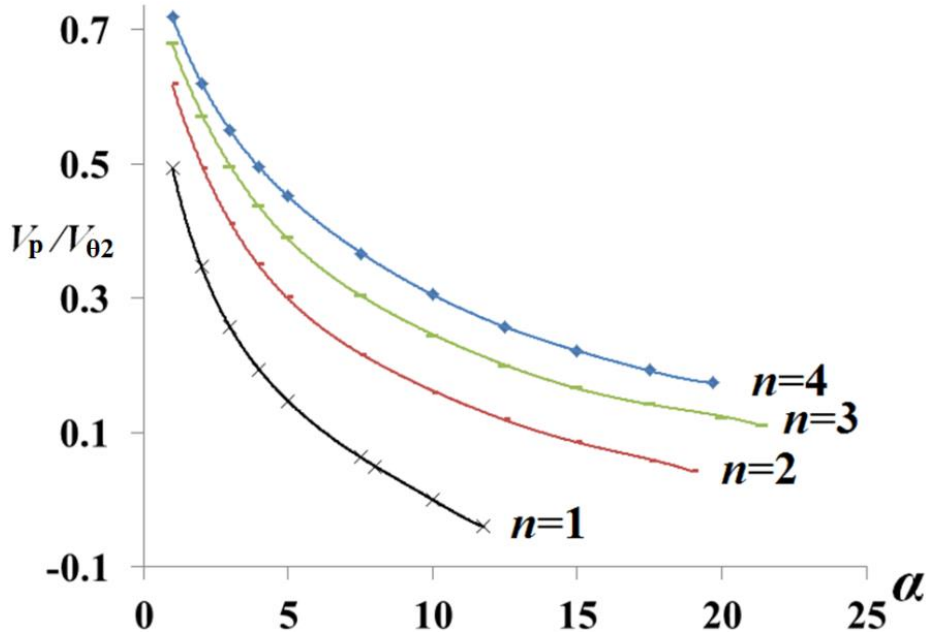

(b) R = 2.5

Figure 3.9 Propagation velocity of cases R = 2 and 2.5

3.4.3 Comparison between theory and experiment for case R = 1.5

Figure 3.10 shows the comparison between the experimental (R = 1.5) and theoretical propagation velocity $V_p/V_{\theta 2}$. The mode n = 1 was eliminated due to its low amplitude which is barely observed in experiments. It can be seen:

(1) The experimental and calculated propagation velocity both increase as the flow rate decreases. This can be explained with the help of the increased circumferential velocity at diffuser inlet.

(2) From the quantitative point of view, the measured propagation velocities agree well with the theoretical predictions, they are of the same order of magnitude. In more details, the theoretical predictions overestimated the propagation velocity for mode n = 3 and 4, and underestimated for n = 2. It also can be seen that the theory predicts larger propagation velocities for stall mode with larger number of cells, but this tendency cannot be observed in the experiments.

In the same manner, for case R = 1.5, the growth rates of different modes are determined as a function of α. The objective is to verify if the dominant stall mode observed in experiment can be predicted by the stall mode with the maximum growth rate. The results are given in Figure 3.11. As it can be seen from this figure, the mode n = 4 has always a maximum growth rate, independently from the angle flow α. This theoretical prediction contrasts with the experimental result for which the observed mode is varying from n = 4 to n = 2 and n = 3 when the diffuser inlet flow angle is decreasing from α = 5.72° to α = 2.29°.

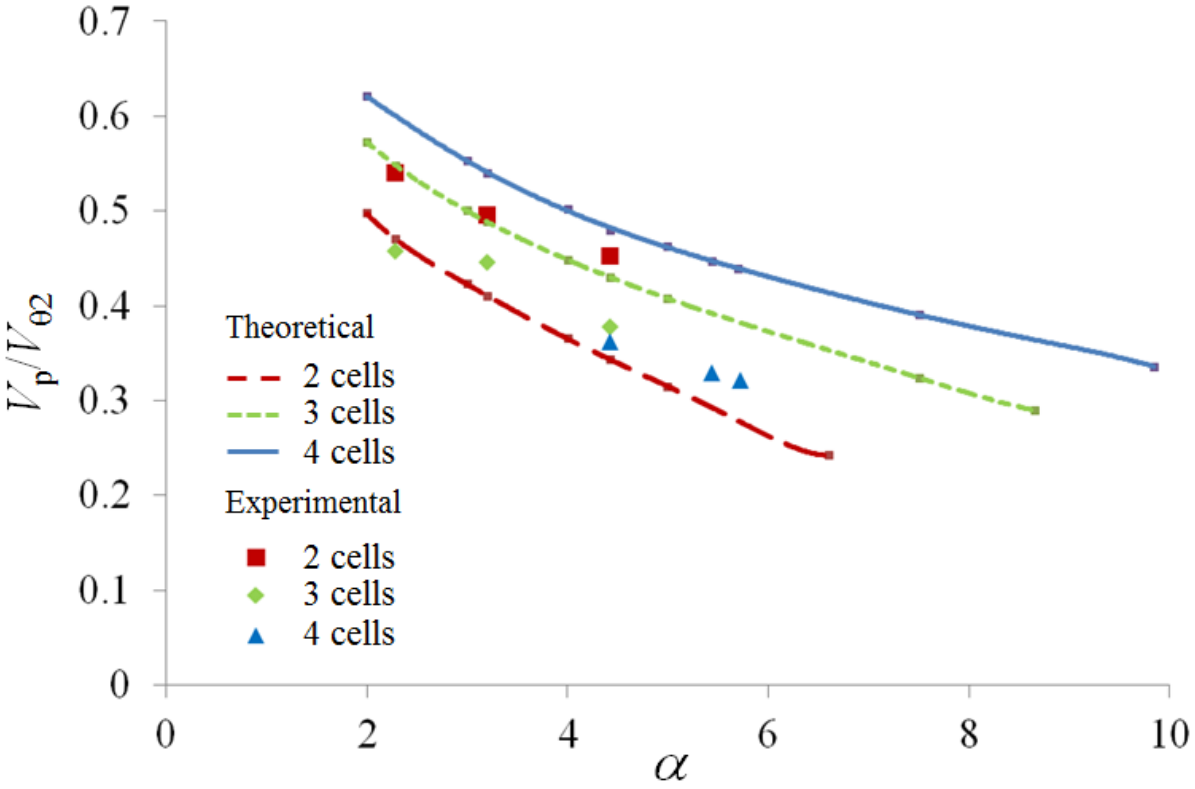

Figure 3.10 Comparison of propagation velocity between experiment and theory (R = 1.5)

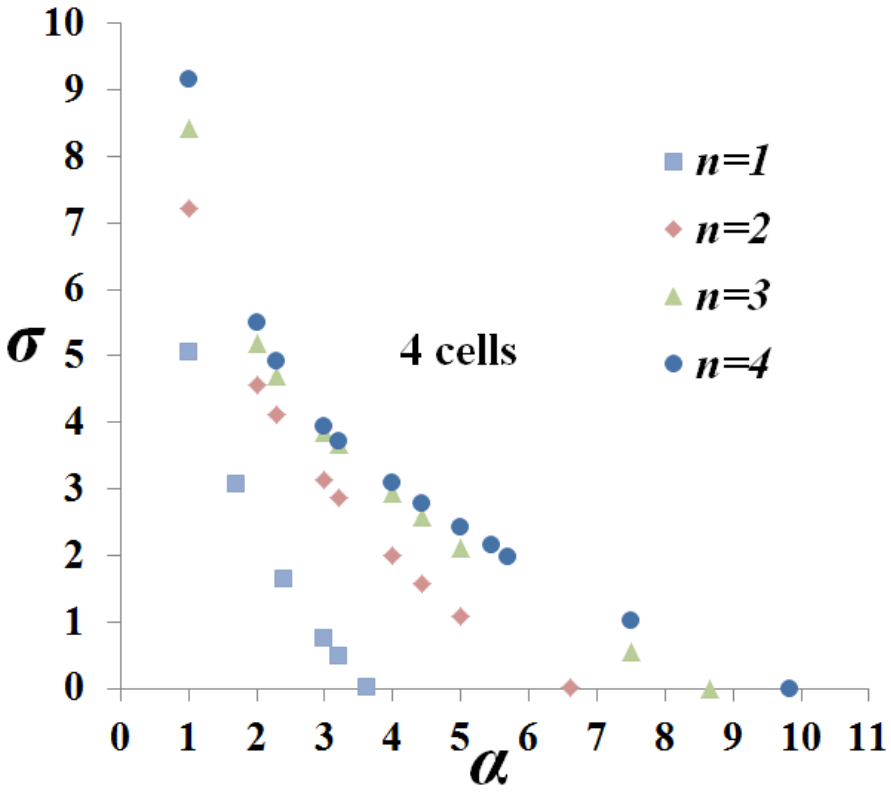

Figure 3.11 The dominant stall mode for R = 1.5

The possible reason is that the linear assumption neglected the effect of non-linear interactions between stall modes. When rotating stall first occurred in the experiment, there was only one mode (n = 4) that can be identified. This is well predicted by the present linear analysis. However, once the flow angle decreased to a certain condition that allows the existence of multi stall modes, the nonlinear interaction could affect the evolution of the dominant mode. In that case, linear approach becomes clearly limited to predict the dominant mode of instability.

Although the theoretical analysis predicted the dominant mode is the one with a larger number of cells for R = 1.5, the same conclusion cannot be drawn for other vaneless diffuser radius ratio R, as shown in Figure 3.8. In fact, the results obtained in the current study indicated that the predicted dominant mode is not always n = 4 but depends on the flow angle α and the radius ratio R. By decreasing α, the dominant mode changes successively from: n = 4 to n = 3 and then to n = 4 cells for case R = 2; from n = 3 to n = 2 and then to n = 4 cells for case R = 2.5. This result is a motivation to perform new experiments with different diffuser radius ratio to get a more comprehensive conclusion.

3.4.4 Velocity vector and pressure distribution

In this section, the characteristics of the shape of the rotating instability mode predicted by the present model will be compared with the results found in literatures.

Firstly, the comparison of the velocity fluctuations associated with a given mode, between the present model and the results given by Tsujimoto et al (1996) is shown in Figure 3.12. In the study of Tsujimoto et al (1996), two stall cells were identified in their experiment when the flow angle $\alpha = 3.3^{o}$ (Figure 3.12(b)). His theory also succeed to predict the two cells stall mode at $\alpha = 13.8^{o}$ (Figure 3.12 (d), which is the critical angle for n = 2). According to that, when flow angle $\alpha = 3.3^{o}$ and 13.8^{o} are specified in present model, we then obtain the corresponding velocity fluctuation using present model, as shown in Figure 3.12 (a) and (c). It can be seen that the stall mode n = 2 also has been well predicted by present model at the two flow conditions. Therefore, the good agreements are obtained between present model and Tsujimoto's theoretical and experimental results, the present analysis is able to predict the velocity fluctuation due to rotating stall in the vaneless diffuser.

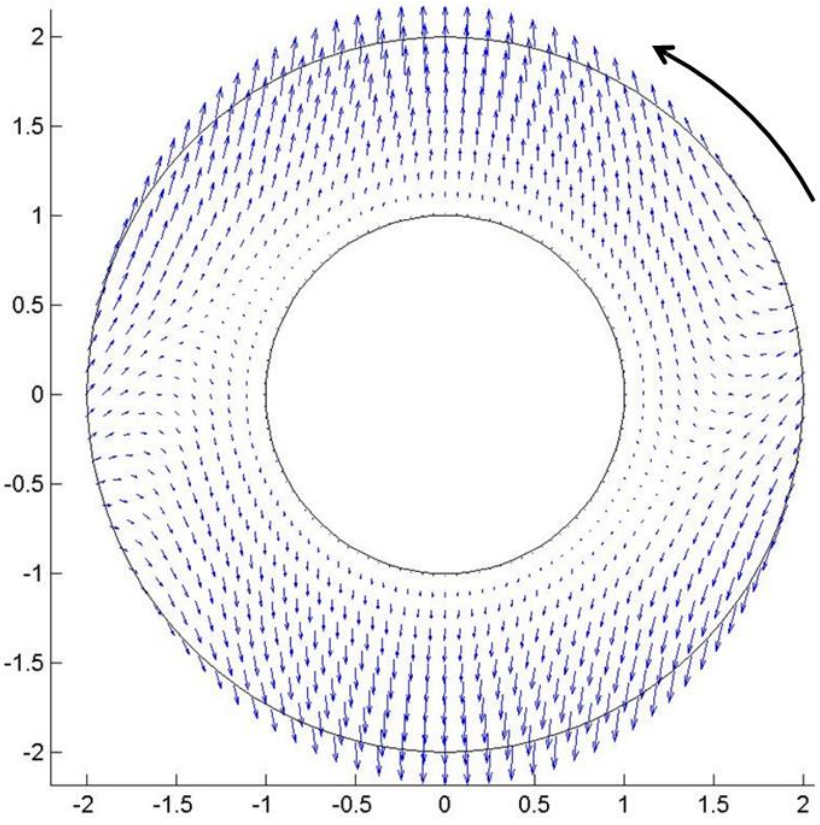

(a) Present model: $R = 2$, $n = 2$, $\alpha = 3.3^{o}$

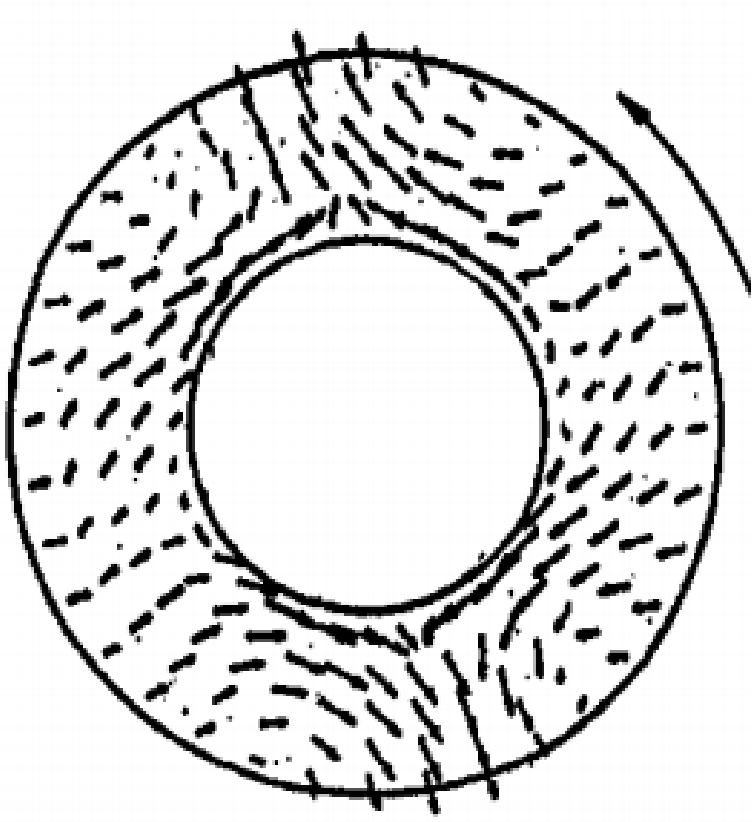

(b) Experimental result of Tsujimoto et al (1996): $R = 2$, $n = 2$, $\alpha = 3.3^{o}$

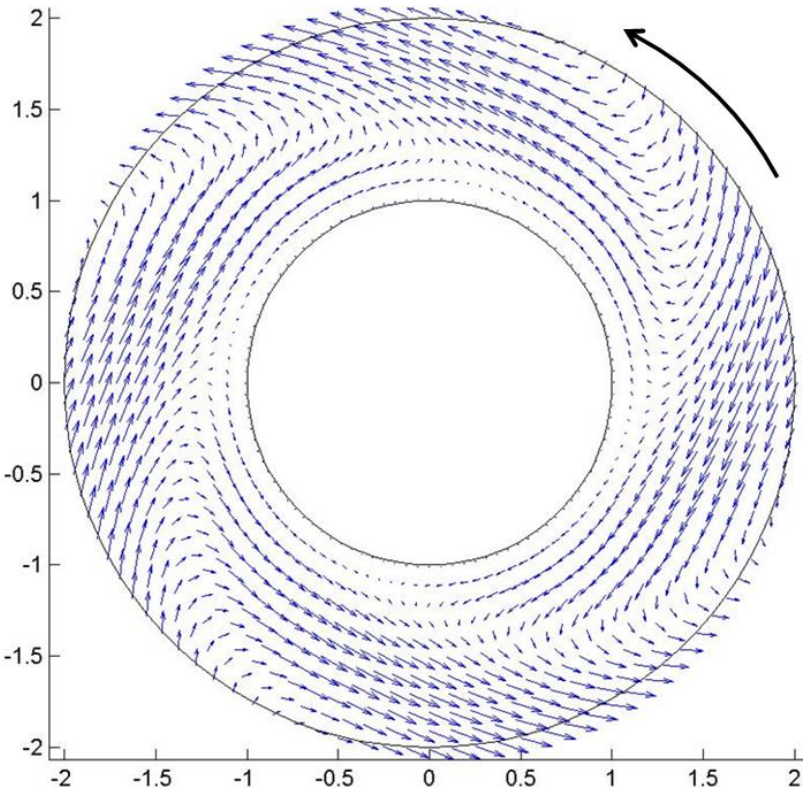

(c) Present model: $R = 2$, $n = 2$, $\alpha = 13.8^{o}$

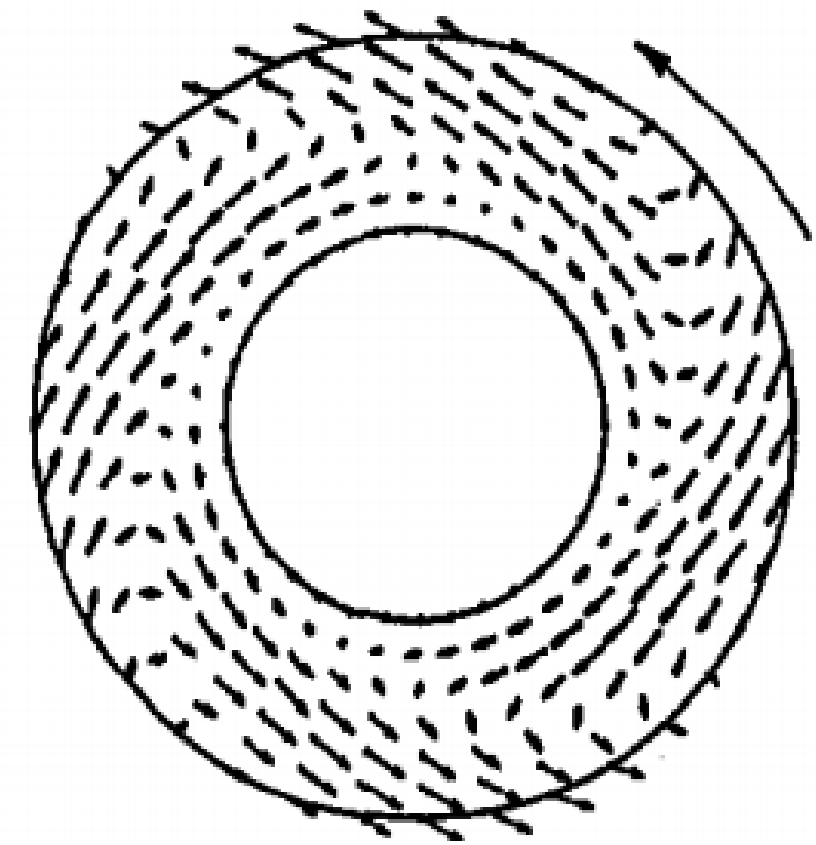

(d) Theoretical result of Tsujimoto et al (1996): $R = 2$, $n = 2$, $\alpha = 13.8^{o}$

Figure 3.12 Comparison of the velocity distribution

The comparison of the radial velocity component between present model and previous PIV result presented by Dazin et al (2011, with the same experimental configuration) is given in Figure 3.13. It should be noticed that the experimental velocities are shown in real values (in m/s), but the values in the theoretical results are only the amplitudes of the corresponding quantities. The PIV result in Figure 3.13 (a) shows a stall mode with 3 cells, and each cell is composed by two cores with inward and outward radial velocity. The similar topology of 3 cells stall is also well predicted by present model in Figure 3.13 (b). For the comparison of tangential velocity between Figure 3.13 (c) and (d), the PIV result shows that three regions are characterized by negative tangential velocity due to the propagation velocity of stall cells is slower than the average tangential velocity, and the present model also predicted those three stall regions with negative tangential velocity.

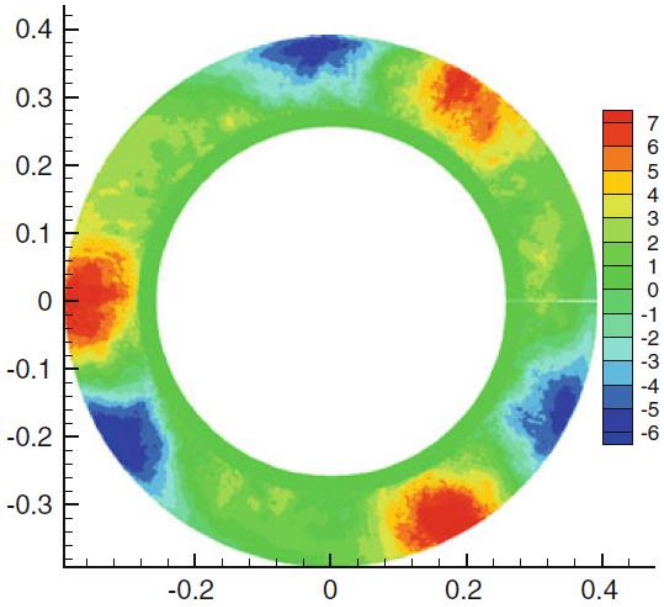

(a) PIV result of Dazin et al (2011): R = 1.5, Q/Q_d = 0.26 (in m/s)

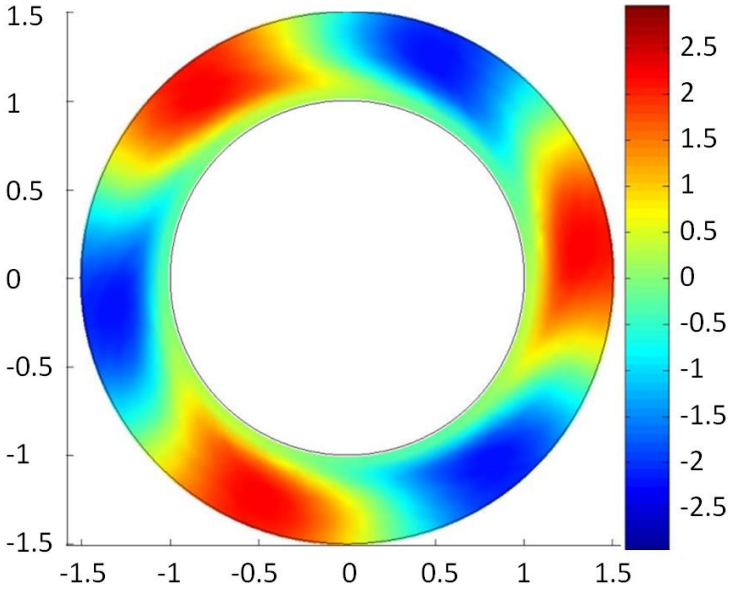

(b) Present model: R = 1.5, n = 3, Q/Q_d = 0.26

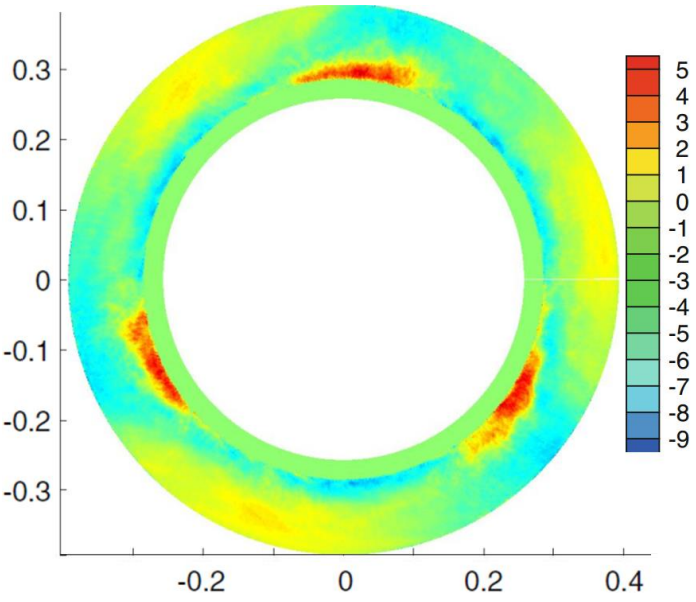

(c) PIV result of Dazin et al (2011): R = 1.5, Q/Q_d = 0.26 (in m/s)

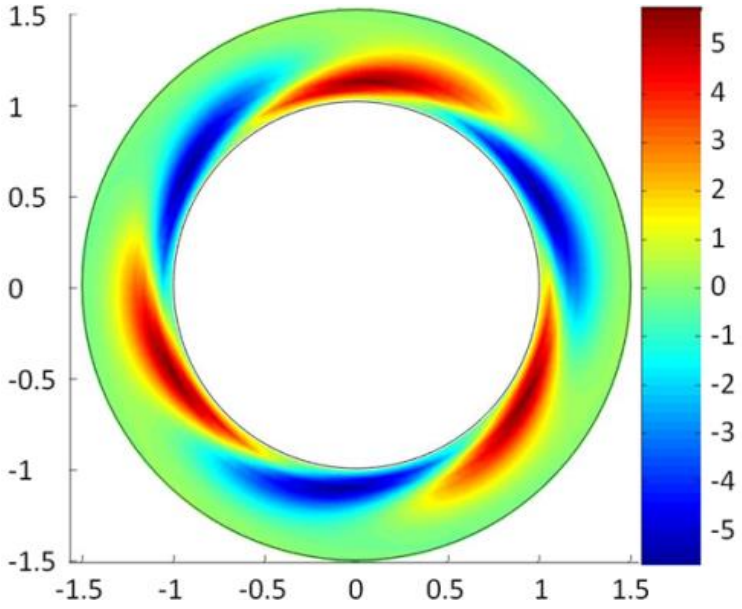

(d) Present model: R = 1.5, n = 3, Q/Q_d = 0.26

Figure 3.13 Comparison of the radial and tangential velocity components

At last, since the velocity fluctuation and radial velocity have been compared, then the comparison of the pressure fluctuation is presented in Figure 3.14. Four cases are compared with present results, they are:

(1) Tsujimoto et al (1996), theory: R = 2, n = 2, α = 13.8º

(2) Tsujimoto et al (1996), experiment: R = 2, n = 2, α = 3.3º

(3) Tsujimoto et al (1996), theory: R = 3, n = 2

(4) Nagashima and Itoh (1989), experiment: R = 3, n = 2

It can be seen that good agreements are obtained when comparing the results calculated by present model to the theoretical or experimental results in literatures. Similar pressure fluctuations are predicted by the present model. Therefore, this study has the capability to describe correctly and qualitatively the shape of the iso-contour of pressure fluctuations due to rotating stall in the vaneless diffuser.

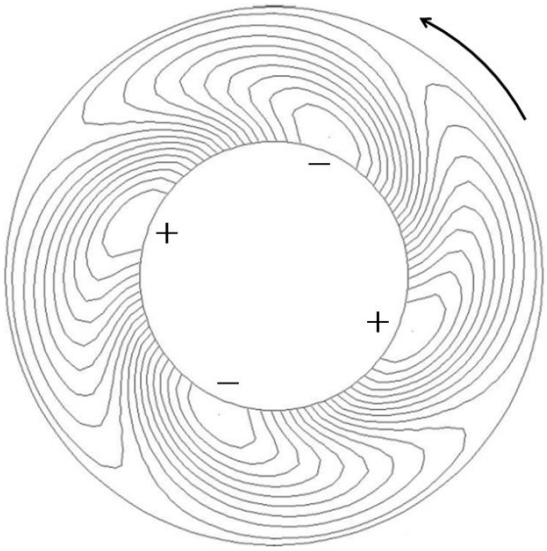

(a) Present model: R = 2, n = 2, α = 13.8º

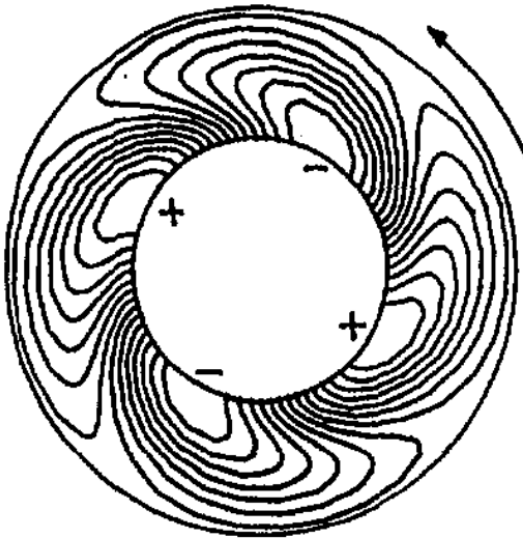

(b) Tsujimoto et al (1996), theory: R = 2, n = 2, α = 13.8º

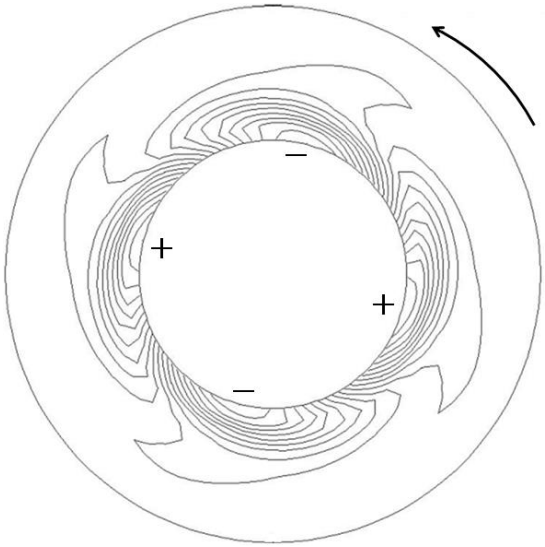

(c) Present model: R = 2, n = 2, α = 3.3º

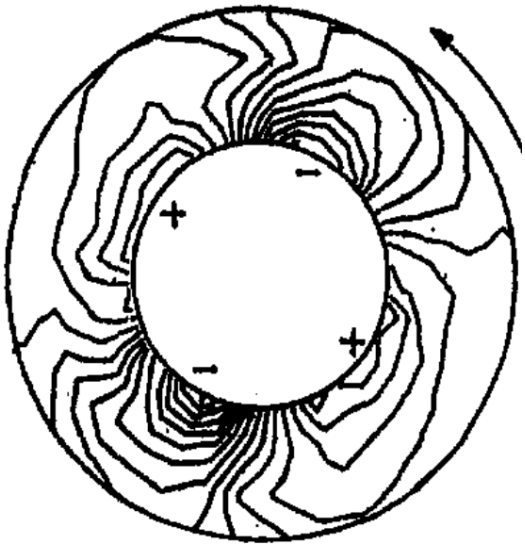

(d) Tsujimoto et al (1996), experiment: R = 2, n = 2, α = 3.3º

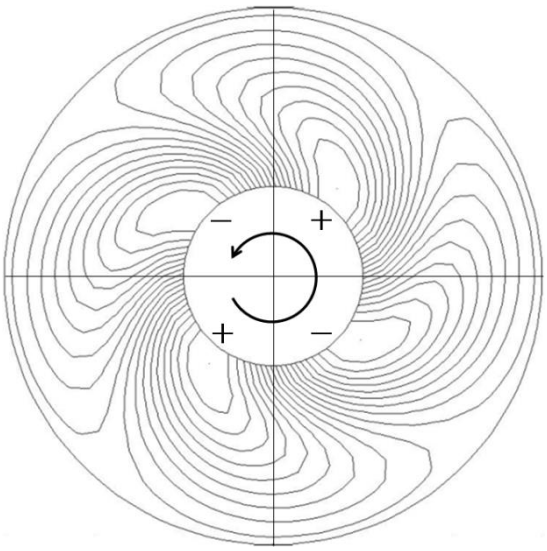

(e) Present model: $R = 3$, $n = 2$

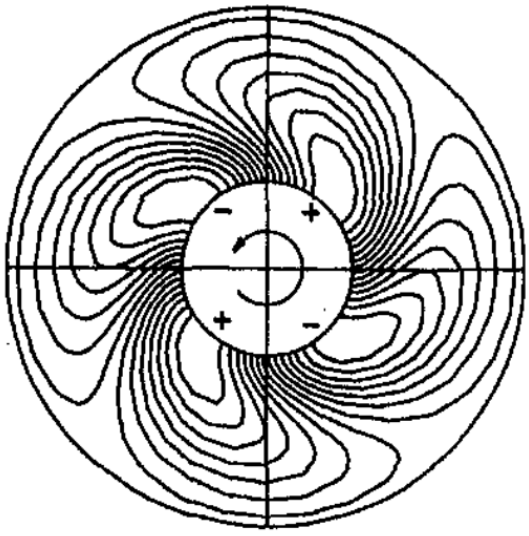

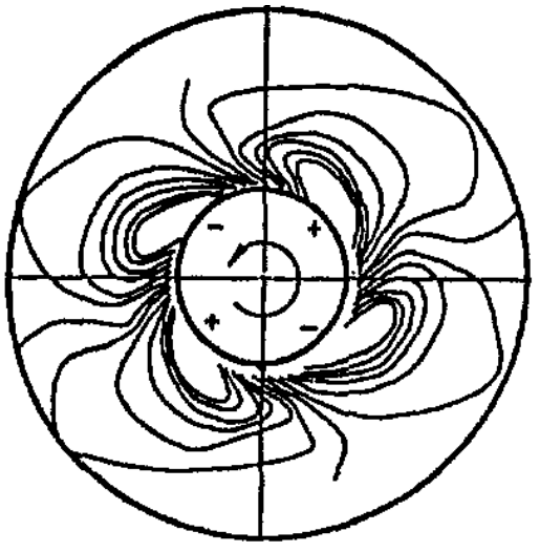

(f) Tsujimoto et al (1996), theory: $R = 3$, $n = 2$ (g) Nagashima and Itoh (1989), experiment: $R = 3$, $n = 2$

Figure 3.14 Comparisons of the pressure fluctuation between present results and literatures

3.4.5 Analysis of the perturbed flow

The linear stability results are now used to try to give some physical explanation to the development of the instability. To do so, an analysis of the kinetic energy of the perturbation is developed in the following to try to identify which term of the equation is the source of the instability.

Applying the complex conjugate of $\tilde{u}_r$ and $\tilde{u}_\theta$ to equations (3.20b) and (3.20c) gives:

$$\bar{\tilde{u}}_r\left(i\omega\tilde{u}_r-\frac{1}{r^2}\tilde{u}_r+\frac{1}{r}\frac{\partial\tilde{u}_r}{\partial r}-\frac{in\mu}{r^2}\tilde{u}_r-\frac{2\mu}{r^2}\tilde{u}_\theta\right)=-\frac{\partial\tilde{p}}{\partial r}\bar{\tilde{u}}_r \tag{3.49}$$

$$\bar{\tilde{u}}_\theta\left(i\omega\tilde{u}_\theta+\frac{1}{r}\frac{\partial\tilde{u}_\theta}{\partial r}+\frac{1}{r^2}\tilde{u}_\theta-in\frac{\mu}{r^2}\tilde{u}_\theta\right)=\frac{1}{r}in\tilde{p}\bar{\tilde{u}}_\theta \tag{3.50}$$

The sum of the two last equations is:

$$i\omega\left(|\tilde{u}_r|^2+|\tilde{u}_\theta|^2\right)-\frac{1}{r^2}|\tilde{u}_r|^2+\frac{1}{r}\frac{\partial\tilde{u}_r}{\partial r}\bar{\tilde{u}}_r+\frac{1}{r}\frac{\partial\tilde{u}_\theta}{\partial r}\bar{\tilde{u}}_\theta+\frac{1}{r^2}|\tilde{u}_\theta|^2-\frac{in\mu}{r^2}\left(|\tilde{u}_r|^2+|\tilde{u}_\theta|^2\right)-\frac{2\mu}{r^2}\bar{\tilde{u}}_r\tilde{u}_\theta$$
$$=-\frac{\partial\tilde{p}}{\partial r}\bar{\tilde{u}}_r+\frac{in\tilde{p}}{r}\bar{\tilde{u}}_\theta \tag{3.51}$$

As $\omega=\omega_{real}-i\sigma$, then the complex conjugate of $i\omega$ is :

$$(\overline{i\omega})=\sigma-i\omega_{real} \tag{3.52}$$

Then the complex conjugate of all equation (3.51) is

$$(\sigma-i\omega_r)\left(|\tilde{u}_r|^2+|\tilde{u}_\theta|^2\right)-\frac{1}{r^2}|\tilde{u}_r|^2+\frac{1}{r}\frac{\partial\bar{\tilde{u}}_r}{\partial r}\tilde{u}_r+\frac{1}{r}\frac{\partial\bar{\tilde{u}}_\theta}{\partial r}\tilde{u}_\theta+\frac{1}{r^2}|\tilde{u}_\theta|^2+\frac{in\mu}{r^2}\left(|\tilde{u}_r|^2+|\tilde{u}_\theta|^2\right)-\frac{2\mu}{r^2}\tilde{u}_r\bar{\tilde{u}}_\theta$$
$$=-\frac{\partial\bar{\tilde{p}}}{\partial r}\tilde{u}_r-\frac{in\bar{\tilde{p}}}{r}\tilde{u}_\theta \tag{3.53}$$

From the linear analysis, the basic solutions are known to be: $V_r=\frac{1}{r}$, $V_\theta=\frac{\mu}{r}$, then the sum of (3.51) and (3.53) is

$$\underbrace{\frac{1}{2}\left(|\tilde{u}_r|^2+|\tilde{u}_\theta|^2\right)\bullet 4\sigma}_{\sigma^*\,4\,E_k}=\underbrace{-2\frac{\partial V_r}{\partial r}|\tilde{u}_r|^2-V_r\frac{\partial}{\partial r}\left(|\tilde{u}_r|^2+|\tilde{u}_\theta|^2\right)-2\frac{V_r}{r}|\tilde{u}_\theta|^2}_{Effect\ of\ V_r}+\underbrace{2\frac{V_\theta}{r}\left(\tilde{u}_r\bar{\tilde{u}}_\theta+\bar{\tilde{u}}_r\tilde{u}_\theta\right)}_{V_\theta}+\underbrace{\left(\frac{in\bar{\tilde{u}}_\theta}{r}\tilde{p}-\bar{\tilde{u}}_r\frac{\partial\tilde{p}}{\partial r}+C.C\right)}_{\tilde{p}} \tag{3.54}$$

where *C.C* is the complex conjugate in the corresponding brackets.

It is interesting to see that the left hand side of equation (3.54) represents the kinetic energy of the perturbation, and the right hand side includes 3 parts which could be associated to three parameters: the radial velocity V_r, tangential velocity V_θ and the pressure fluctuation $\tilde{p}$. It means that the growing of the perturbation is depending on the values of these three components.

The contribution of the pressure fluctuation can be simplified by the continuity equation (3.20a), which gives

$$in\bar{\tilde{u}}_\theta=-\frac{\partial(r\bar{\tilde{u}}_r)}{\partial r} \tag{3.55}$$

then the terms with $\tilde{p}$ in equation (3.54) becomes:

$$\frac{in}{r}\bar{\tilde{u}}_\theta \tilde{p} - \frac{\partial \tilde{p}}{\partial r}\bar{\tilde{u}}_r + C.C = -\frac{1}{r}\frac{\partial (r\bar{\tilde{u}}_r)}{\partial r}\tilde{p} - \frac{\partial \tilde{p}}{\partial r}\bar{\tilde{u}}_r + C.C = -\frac{\tilde{p}\bar{\tilde{u}}_r}{r} - \frac{\partial (\bar{\tilde{u}}_r \tilde{p})}{\partial r} + C.C = -\frac{1}{r}\frac{\partial}{\partial r}(r\bar{\tilde{u}}_r \tilde{p}) + C.C \tag{3.56}$$

Then, both sides of equation (3.54) will be integrated from diffuser inlet to outlet to get:

(1) For the left hand side, the total variation of kinetic energy of the perturbation is obtained.

(2) For the right hand side, the contribution of radial velocity component, tangential velocity component and pressure is obtained.

The integration of the term corresponding to pressure fluctuation in equation (3.54) gives:

$$\int_1^R \left[r \bullet -\frac{1}{r}\frac{\partial}{\partial r}(r\bar{\tilde{u}}_r \tilde{p}) \right] dr = \left[-r\bar{\tilde{u}}_r \tilde{p} \right]_1^R \tag{3.57}$$

The boundary conditions in the present linear analysis are:

$$\bar{\tilde{u}}_r = 0 \text{ when } r = 1; \ \tilde{p} = 0 \text{ when } r = R$$

Therefore, the equation (3.57) is equal to zero, which means that the pressure fluctuation term has no contribution to the occurrence of rotating instability. Then, the growth rate of rotating instability in equation (3.54) can be simply written as follow,

$$\sigma = \tilde{\tilde{E}}_{V_r} + \tilde{\tilde{E}}_{V_\theta} \tag{3.58}$$

where

$$\tilde{E}_{V_r} = \frac{\int_1^R [-2|\tilde{u}_r|^2 \frac{\partial V_r}{\partial r} - \frac{\partial}{\partial r}\left(|\tilde{u}_r|^2 + |\tilde{u}_\theta|^2\right)V_r - \frac{2}{r}|\tilde{u}_\theta|^2 V_r] r dr}{\int_1^R 2\left(|\tilde{u}_r|^2 + |\tilde{u}_\theta|^2\right) r dr}$$

$$\tilde{E}_{V_\theta} = \frac{\int_1^R V_\theta (\tilde{u}_r \bar{\tilde{u}}_\theta + \bar{\tilde{u}}_r \tilde{u}_\theta) dr}{\int_1^R \left(|\tilde{u}_r|^2 + |\tilde{u}_\theta|^2\right) r dr}$$

Equation (3.58) gives a simple expression to show that the growth rate of rotating instability can be expressed simply as the contribution of two terms linked respectively with the radial and tangential velocity components. An example of the two contributions obtained for case: $R = 2$, $n = 4$, from stable condition ($\sigma < 0$) → critical condition ($\sigma = 0$) → unstable condition ($\sigma < 0$), are plotted in Figure 3.15.

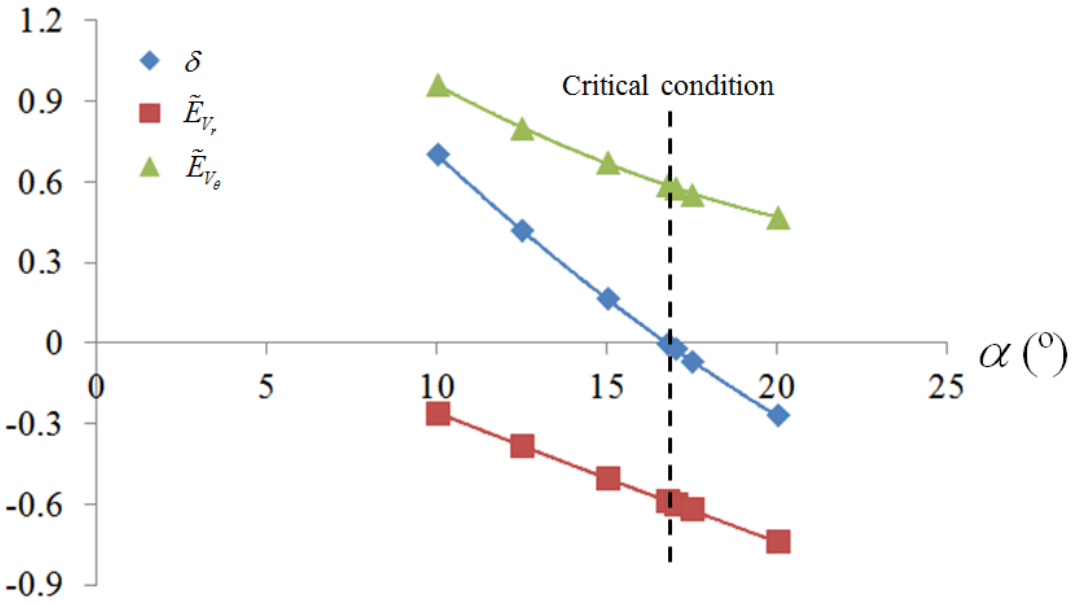

Figure 3.15 Contributions of the two parts on the instability: R = 2, n = 4

In any flow condition, for the whole diffuser space, it can be seen that the radial velocity term $\tilde{E}_{V_r}$ always give a negative contribution (that is a stabilizing effect on the flow) while the tangential velocity one provides always a positive contribution (that is a destabilizing effect on the flow). With the decrease of flow angle, the stabilizing effect from radial component is becoming weaker and weaker, and the destabilizing effect from tangential velocity is getting stronger and stronger which leads to the development of the instability when the destabilizing effect stronger than the stabilizing one. Since the flow angle is directly linked with the radial to tangential velocity components ratio, this analysis confirmed again the importance of the flow angle to the stability of the diffuser flow.

3.4.6 Characteristic times associated with the convection of a perturbation

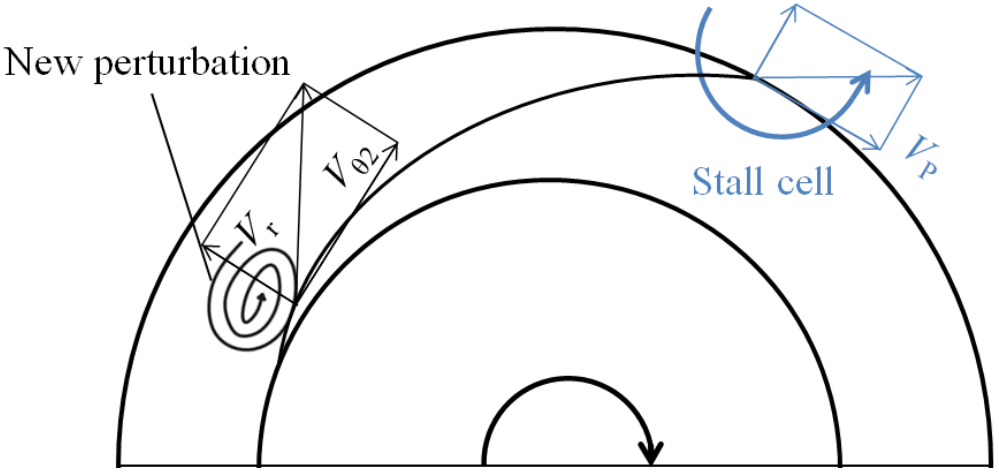

Figure 3.16 New perturbation and the stall cell in the vaneless diffuser

The previous paragraph has clearly shown that the radial velocity component has clearly a stabilizing effect whereas the tangential one has a destabilizing effect on the flow in the

diffuser. A simple model based on the characteristic times associated with the convection of the propagation is proposed below. The idea is to imagine that a perturbation associated with the inception of the unstable mode *n* is created in the diffuser, and then to compare the characteristic time needed for this perturbation to flow out from the diffuser with the characteristic time needed for this perturbation to interact with the perturbed flow.

The order of magnitude of the time needed for the perturbation to flow out of the vaneless diffuser is:

$$t_1 \sim \frac{r_4 - r_3}{V_r} \tag{3.59}$$

Assuming that the perturbation is convected by the steady flow, in the circumferential direction and that the mode is propagate in this direction with a velocity V_p, then the order of magnitude of the time needed for the perturbation to catch the previous unstable cell is:

$$t_2 \sim \frac{2\pi}{n} \frac{r_3}{V_{\theta 2} - V_P} \tag{3.60}$$

If it is supposed that the propagation velocity of the mode is a fraction of the steady tangential velocity:

$$k = \frac{V_P}{V_{\theta 2}} \tag{3.61}$$

we get:

$$t_2 \sim \frac{2\pi}{n} \frac{r_3}{V_{\theta 2}(1-k)} \tag{3.62}$$

Therefore, if $t_2 < t_1$, the perturbation will catch the stall cell before it flows out of the vaneless diffuser, then the mode *n* will develop if the following condition is satisfied:

$$t_2 < t_1 \Rightarrow \frac{2\pi r_3}{n V_{\theta 2}(1-k)} < \frac{r_4 - r_3}{V_r} \Rightarrow \tan\alpha < \frac{n(\frac{r_4}{r_3} - 1)(1-k)}{2\pi} \tag{3.63}$$

To check the validity of this analysis, critical condition given by equation (3.63) are compared to the critical conditions coming from the linear stability analysis (Figure 3.4). To do this, equation (3.63) is calculated with the value of *k* which can be obtained from Figure 3.4(b). The corresponding curves for *n* = 1, 2 and 3 are compared to the linear stability critical conditions in Figure 3.17. Although the analysis is based only on some orders of magnitudes, it gives qualitatively good results, with an increase of the critical angle with the radius ratio and with the number of cells. Moreover, it gives also qualitatively correct results, especially for radius ratio lower than 2.

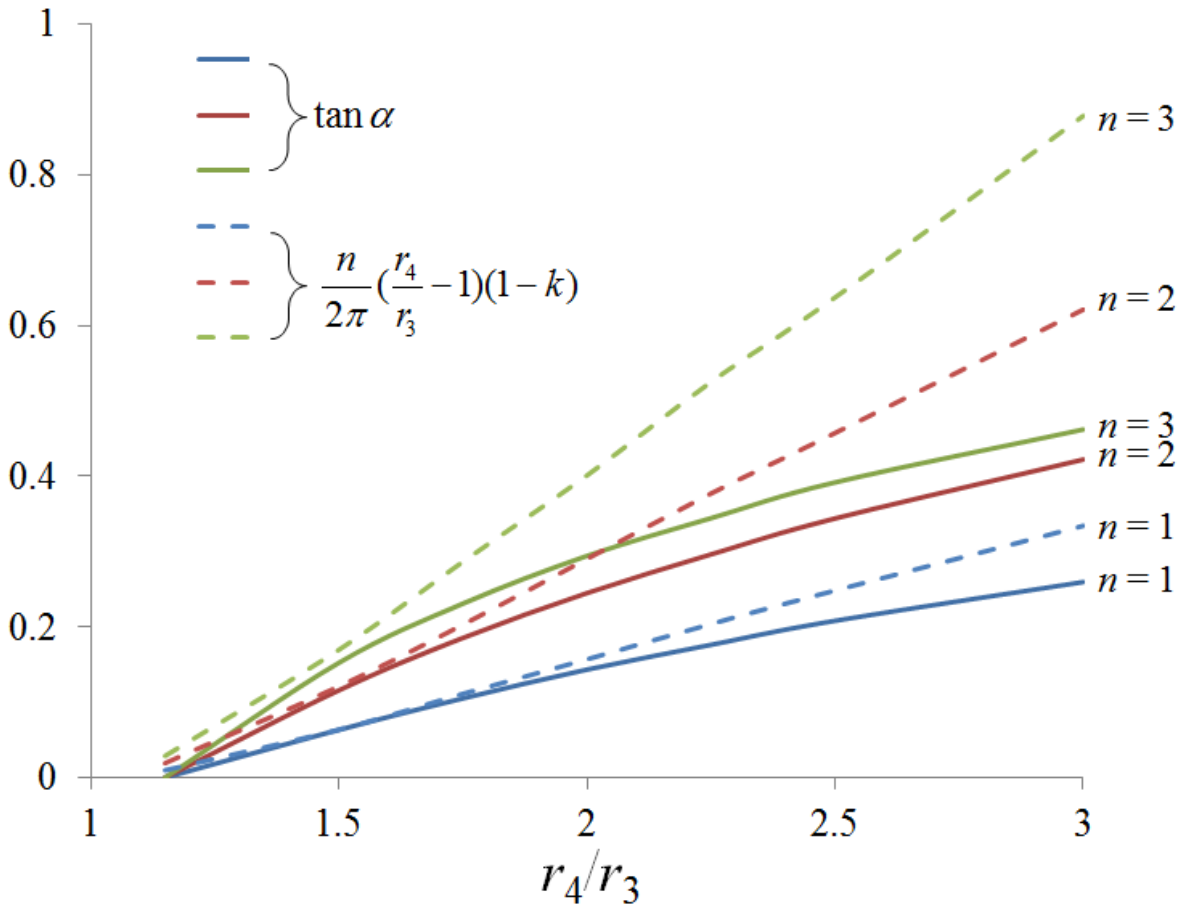

Figure 3.17 Comparison of tan α and $n(r_4/r_3\text{-}1)(1\text{-}k)/2\pi$

At last, several conclusions can be drawn from the analysis proposed in this section about the arising of the rotating instability in the vaneless diffuser.

(1) The instability is developing when the flow angle is below a critical value because when flow angle is small, it will take more time for a perturbation to go out from the diffuser and less time for it to interact with the previous unstable cell. This explains also why the radial velocity component is stabilizing the flow whereas the tangential velocity component has a destabilizing effect on the flow.

(2) The instability is more likely to happen in high radius ratio diffuser because in this case, the time needed for a perturbation to go out from the diffuser is longer.

(3) The instability is developing first for high number of modes because the more is the number of mode, the less is the distance between two cells.

3.5 Discussions and conclusions

In this chapter, a linear stability analysis is presented to study rotating stall in the wide vaneless diffuser. The characteristics of rotating stall are calculated and compared to the results found in literatures, the abilities and limits of such a methodology haven then been discussed.

In section 3.4.1, the propagation velocity and critical flow angle of rotating stall have been calculated. Through the comparison, good agreement were obtained for the stall modes n = 1, 2, and 3, the critical flow angle and propagation velocity for each mode seems only increase or decrease function of the radius ratio. However, the stall mode n = 4 calculated by present model shows that the critical flow angle and propagation velocity are not simply increase or decrease with the radius ratio. It can be seen from Figure 3.4a that the critical flow angle of mode: R = 3, n = 4 is even smaller than modes R = 3, n = 2 and 3, and also smaller than case R = 2.5, n = 4. Similar results also can be observed from Figure 3.4b, the propagation velocity for R = 3, n = 4 is smaller than R = 2.5, n = 4. These results can be verified by the results presented by Ljevar (2007) in Figure 3.5. Therefore, it seems there is no general tendencies can be drawn from the plots of critical flow angle or propagation velocity if stall modes with $n \geq 4$ are taken into account. Nevertheless, this discussion has a limited practical interest as stall modes with $n \geq 5$ have never been observed experimentally.

In the experiment, we have observed several stall modes at one flow condition, and one dominant stall mode can be identified. Therefore, in section 3.4.2, we tried to estimate the growth rate of each stall mode in order to determine the most unstable one (with maximum growth rate). Although the theory failed to determine the dominant stall mode for the configuration used in experiment (R = 1.5), but the predictions for R = 2 and 2.5 shows that the dominant stall mode varies with the flow angle. This motivates us performed an analysis of the growth rate in section 3.4.5. It has been shown that the growth rate of stall mode is the results of three contributions associated respectively with the radial velocity, tangential velocity and pressure. The pressure term has no effect on the flow, the radial velocity term has a stabilizing effect and the tangential one has a destabilizing one. The analysis presented in section 3.4.6 physically explained why the stall mode is developing in the experiment (different stall modes exist intermittently), and also explained why the radial velocity component is stabilizing the flow whereas the tangential velocity component has a destabilizing effect on the flow (in section 3.4.5).

The misprediction of the experimental dominant stall mode could be ascribed to the neglected nonlinear terms in the linear analysis. They may affect the final result of the growth rate for each mode. The limitation of the linear stability model motivates a weakly nonlinear stability analysis which will be presented in the next chapter.

Chapter 4 Weakly nonlinear stability analysis

4.1 Introduction

In the previous chapter it has been demonstrated that for the flow angle in the vaneless diffuser smaller than a critical value α_c the basic state of our model, i.e. a two-dimensional steady flow, is unstable. The linear theory shows that in this case, rotating instability with exponentially growing amplitude will develop. However, the linear stability approach is only valid in the initial growth stage, where the wave amplitude is infinitely small. If we want to describe the nonlinear dynamic behavior and to determine the evolution of the rotating stall, a nonlinear stability approach is needed. A detailed analysis is possible if the flow angle in the vaneless diffuser is only slightly smaller than the critical value α_c. In that case the weakly nonlinear dynamics of the linearly unstable modes can be described by an amplitude equation. In this chapter, the control parameter used is $\mu = \dfrac{1}{\tan\alpha}$ instead of the angle α.

4.2 Governing equations for finite amplitude disturbances

The perturbations of the basic two-dimensional steady flow can be expressed as

$$\begin{cases} V_r = \dfrac{1}{r} + u_r(r,\theta,t) \\ V_\theta = \dfrac{\mu}{r} + u_\theta(r,\theta,t) \\ \zeta = 0 + \zeta(r,\theta,t) \\ P = P_B + p(r,\theta,t) \end{cases} \tag{4.1}$$

We insert above terms into the system (3.17a) – (3.17e) and obtain the nonlinear set of equations for the perturbations (u_r, u_θ, p),

$$\frac{\partial (r u_r)}{\partial r} + \frac{\partial u_\theta}{\partial \theta} = 0 \tag{4.2a}$$

$$\frac{\partial u_r}{\partial t} - \frac{u_r}{r^2} + \frac{1}{r}\frac{\partial u_r}{\partial r} + \frac{\mu}{r^2}\frac{\partial u_r}{\partial \theta} - \frac{2\mu}{r^2}u_\theta + \frac{\partial p}{\partial r} = -u_r\frac{\partial u_r}{\partial r} - \frac{u_\theta}{r}\frac{\partial u_r}{\partial \theta} + \frac{u_\theta^2}{r} \tag{4.2b}$$

$$\frac{\partial u_\theta}{\partial t} + \frac{u_\theta}{r^2} + \frac{1}{r}\frac{\partial u_\theta}{\partial r} + \frac{\mu}{r^2}\frac{\partial u_\theta}{\partial \theta} + \frac{1}{r}\frac{\partial p}{\partial \theta} = -u_r\frac{\partial u_\theta}{\partial r} - \frac{u_\theta}{r}\frac{\partial u_\theta}{\partial \theta} - \frac{u_r u_\theta}{r} \tag{4.2c}$$

The system (4.2a) – (4.2c) must be solved with specific boundary conditions as proposed in linear analysis,

$$u_r = u_\theta = 0 \text{ at } r = 1 \text{ and } p = 0 \text{ at } r = R \tag{4.2d}$$

In the following, we use the same strategy as in the linear stability analysis by adopting the velocity/vorticity formulation. Once the components of the velocity perturbation (u_r, u_θ) are determined, the pressure perturbation is deduced by using either the equation (4.2b) or the equation (4.2c).

The perturbation of vertical component of the vorticity is defined as in the previous chapter,

$$\zeta = \frac{1}{r}\frac{\partial (r u_\theta)}{\partial r} - \frac{1}{r}\frac{\partial u_r}{\partial \theta} \tag{4.2e}$$

and obeys to the nonlinear evolution equation,

$$\frac{\partial \zeta}{\partial t} + \frac{1}{r}\frac{\partial \zeta}{\partial r} + \frac{\mu}{r^2}\frac{\partial \zeta}{\partial \theta} = -u_r \frac{\partial \zeta}{\partial r} - \frac{u_\theta}{r}\frac{\partial \zeta}{\partial \theta} \tag{4.2f}$$

4.3 Derivation of the amplitude equation

In order to derive the amplitude equation, we make use of the perturbation expansion near the critical threshold μ_c. In solving weakly nonlinear hydrodynamic problems with this method for a non-self-adjoint linear operator, we must also use the corresponding adjoint operator. Then we perform inner product using both, the solutions of the homogeneous linear operator and of the adjoint homogeneous linear operator. The corresponding amplitude equation is then obtained from a solvability condition, known as the Fredholm alternative, which states the fact that the inhomogeneity must be orthogonal to the solution of the adjoint problem.

We first introduce a small parameter ε which measures the distance to criticality by setting

$$\mu = \mu_c + \varepsilon^2 \mu_2 \tag{4.3}$$

where μ_2 is of order unity, and μ_c is the threshold at critical condition.

The nonlinear theory described below has been applied to various classical hydrodynamic stability problems (see for instance Newell and Whitehead (1969), Stewartson and Stuart (1971) and has been tested experimentally (see for instance Drazin and Reid (1981) for an overview). In these experiments, it has been found that the predictions based on the weakly nonlinear theory might be valid far from the critical condition, i.e. the theory seems to be valid for ε of an order 1 magnitude.

The temporal scaling may be obtained by expanding the complex frequency ω in a Taylor series near μ_c:

$$\omega = \omega_c + (\tau + i\nu)\ (\mu - \mu_c) + \ldots$$

where

$$\tau + i\nu = \left(\frac{\partial \omega}{\partial \mu}\right)_c$$

Substitution of the Taylor series of ω near μ_c in the linear solutions (3.19) yields

$$\{u_r, u_\theta, \zeta, p\}(r,\theta,t) = A\{\tilde{u}_r, \tilde{u}_\theta, \tilde{\zeta}, \tilde{p}\}(r) e^{i\omega_c t - in\theta} e^{i(\tau + iv)(\mu - \mu_c)t} + \ldots = A(t_2)\{\tilde{u}_r, \tilde{u}_\theta, \tilde{\zeta}, \tilde{p}\}(r) e^{i\omega_c t - in\theta} + \ldots$$

This describes the modulation of the amplitude $A(t_2)$ of the critical wave with frequency ω_c.

As $\mu - \mu_c = O(\varepsilon^2)$, the modulation is at slow temporal scale,

$$t_2 = \varepsilon^2 t \tag{4.4}$$

The temporal derivative is then replaced by

$$\frac{\partial}{\partial t} \to \frac{\partial}{\partial t} + \varepsilon^2 \frac{\partial}{\partial t_2} \tag{4.5}$$

The evolution equations are obtained by expanding the perturbations in power series of ε:

$$\{u_r, u_\theta, \zeta, p\}(r,\theta,t,t_2) = \varepsilon\{u_r^{(1)}, u_\theta^{(1)}, \zeta^{(1)}, p^{(1)}\} + \varepsilon^2\{u_r^{(2)}, u_\theta^{(2)}, \zeta^{(2)}, p^{(2)}\} + \varepsilon^3\{u_r^{(3)}, u_\theta^{(3)}, \zeta^{(3)}, p^{(3)}\} + o(\varepsilon^3) \tag{4.6}$$

The perturbation fields $\{u_r^{(i)}, u_\theta^{(i)}, \zeta^{(i)}, p^{(i)}\}$ depend on the slow variable t_2. By substituting expressions (4.3) – (4.6) in the system (4.2a) – (4.2f), and collecting coefficients of ε, a set of equations is obtained. For example (4.2f) becomes

$$\begin{aligned}
&\left[\left(\frac{\partial}{\partial t} + \varepsilon^2 \frac{\partial}{\partial t_2}\right) + \frac{1}{r}\frac{\partial}{\partial r} + \frac{1}{r^2}\left(\mu_c + \varepsilon^2 \mu_2\right)\frac{\partial}{\partial \theta}\right]\left[\varepsilon\zeta^{(1)} + \varepsilon^2\zeta^{(2)} + \varepsilon^3\zeta^{(3)} + \cdots\right] \\
&= -\left[\varepsilon u_r^{(1)} + \varepsilon^2 u_r^{(2)} + \varepsilon^3 u_r^{(3)} + \cdots\right]\frac{\partial}{\partial r}\left[\varepsilon\zeta^{(1)} + \varepsilon^2\zeta^{(2)} + \varepsilon^3\zeta^{(3)} + \cdots\right] \\
&-\frac{1}{r}\left[\varepsilon u_\theta^{(1)} + \varepsilon^2 u_\theta^{(2)} + \varepsilon^3 u_\theta^{(3)} + \cdots\right]\frac{\partial}{\partial \theta}\left[\varepsilon\zeta^{(1)} + \varepsilon^2\zeta^{(2)} + \varepsilon^3\zeta^{(3)} + \cdots\right]
\end{aligned} \tag{4.7}$$

4.3.1 First order solutions

To the first order in ε, the set of linear homogeneous equations are the same as the linear analysis, which has been solved in chapter 3. At this order the solutions for the components of the velocity field and the vertical vorticity are given by

$$\{u_r, u_\theta, \zeta\}(r,\theta,t) = A(t_2)\{\tilde{u}_r, \tilde{u}_\theta, \tilde{\zeta}\}(r) e^{i\omega_c t - in\theta}$$

with the solutions which have also been given in chapter 3,

$$\begin{cases} \tilde{\zeta}(r) = e^{-\frac{i\omega_c}{2}(r^2-1)+in\mu_c \ln r} \\ \tilde{u}_r = -i\left\{F^\zeta + G^\zeta - G^\zeta(r=1)r^{n-1}\right\} \\ \tilde{u}_\theta = \left\{F^\zeta - G^\zeta + G^\zeta(r=1)r^{n-1}\right\} \end{cases}$$

$$\begin{cases} F^\zeta(r) = \frac{1}{2}\int_1^r e^{-\frac{i\omega_c}{2}(r_0^2-1)+in\mu_c \ln r_0}(\frac{r_0}{r})^{n+1}dr_0 \\ G^\zeta(r) = \frac{1}{2}\int_r^R e^{-\frac{i\omega_c}{2}(r_0^2-1)+in\mu_c \ln r_0}(\frac{r}{r_0})^{n-1}dr_0 \end{cases}$$

4.3.2 Adjoint problem

Proceeding with the higher orders of the expansion requires the determination of the eigen-functions of the adjoint problem. We consider the vector $X = (\tilde{u}_r(r), \tilde{u}_\theta(r), \tilde{\zeta}(r))^T$ (here T is the transpose) containing eigen-functions for the components of the velocity field and the vertical vorticity obtained previously. We define the eigen-functions of the adjoint problem by the vector

$$X^* = (\tilde{u}_r^*(r), \tilde{u}_\theta^*(r), \tilde{\zeta}^*(r))^T \tag{4.8}$$

and we note $L = (L_1(X), L_2(X), L_3(X))^T$ the linear operator defined by

Continuity equation:

$$L_1(X) = \frac{1}{r}[\frac{\partial(r\tilde{u}_r)}{\partial r} - in\tilde{u}_\theta] = 0 \tag{4.9}$$

Vorticity equations:

$$L_2(X) = \tilde{\zeta} - \frac{1}{r}[\frac{\partial(r\tilde{u}_\theta)}{\partial r}] + \frac{in}{r}\tilde{u}_r = 0 \tag{4.10}$$

$$L_3(X) = (i\omega_c + \frac{1}{r}\frac{\partial}{\partial r} - \frac{in\mu_c}{r^2})\tilde{\zeta} = 0 \tag{4.11}$$

and we give the definition of adjoint problem as follow

$$\left\langle X^*, LX \right\rangle = \left\langle L^* X^*, X \right\rangle \tag{4.12}$$

with the appropriate scalar product is

$$\left\langle f, g \right\rangle = \int_1^R (f \bullet \bar{g}) r dr \tag{4.13}$$

Then the left side of (4.12) is

$$\left\langle X^*, LX \right\rangle = \int_1^R \tilde{u}_r^* \frac{1}{r}[\frac{d(r\bar{\tilde{u}}_r)}{dr} + in\bar{\tilde{u}}_\theta]\, rdr + \int_1^R \tilde{u}_\theta^*[\bar{\tilde{\zeta}} - \frac{1}{r}(\frac{d(r\bar{\tilde{u}}_\theta)}{dr}) - \frac{in}{r}\bar{\tilde{u}}_r]\, rdr +$$

$$\int_1^R \tilde{\zeta}^*(-i\omega_c + \frac{1}{r}\frac{d}{dr} + \frac{in\mu_c}{r^2})\bar{\tilde{\zeta}}\, rdr \tag{4.14}$$

meanwhile, the right side of (4.12) is

$$\left\langle L^*X^*, X \right\rangle = \int_1^R (L_1^*X^*)\bar{\tilde{u}}_r rdr + \int_1^R (L_2^*X^*)\bar{\tilde{u}}_\theta rdr + \int_1^R (L_3^*X^*)\bar{\tilde{\zeta}}\, rdr \tag{4.15}$$

We look for a link between the left and right side, therefore, all the terms in (4.14) will be classified as follow:

$$\int_1^R \tilde{u}_r^* \frac{1}{r}\frac{\partial(r\bar{\tilde{u}}_r)}{\partial r} rdr = \left[r\bar{\tilde{u}}_r\tilde{u}_r^* \right]_1^R - \int_1^R r\bar{\tilde{u}}_r \frac{\partial\tilde{u}_r^*}{\partial r} dr \in \int_1^R (L_1^*X^*)\bar{\tilde{u}}_r rdr$$

$$\int_1^R \tilde{u}_r^* \frac{in\bar{\tilde{u}}_\theta}{r} rdr \in \int_1^R (L_2^*X^*)\bar{\tilde{u}}_\theta rdr$$

$$\int_1^R \tilde{u}_\theta^*\bar{\tilde{\zeta}}\, rdr \in \int_1^R (L_3^*X^*)\bar{\tilde{\zeta}}\, rdr$$

$$\int_1^R \tilde{u}_\theta^*[-\frac{1}{r}(\frac{\partial(r\bar{\tilde{u}}_\theta)}{\partial r})]rdr = -\left[r\bar{\tilde{u}}_\theta\tilde{u}_\theta^* \right]_1^R + \int_1^R r\bar{\tilde{u}}_\theta \frac{\partial\tilde{u}_\theta^*}{\partial r} dr \in \int_1^R (L_2^*X^*)\bar{\tilde{u}}_\theta rdr$$

$$\int_1^R \tilde{u}_\theta^*(-\frac{in}{r}\bar{\tilde{u}}_r)rdr \in \int_1^R (L_1^*X^*)\bar{\tilde{u}}_r rdr$$

$$\int_1^R \left[\tilde{\zeta}^*(-i\omega_c + \frac{1}{r}\frac{\partial}{\partial r} + \frac{in\mu_c}{r^2})\bar{\tilde{\zeta}} \right] rdr = \int_1^R \tilde{\zeta}^*(-i\omega_c + \frac{in\mu_c}{r^2})\bar{\tilde{\zeta}}\, rdr + \int_1^R \tilde{\zeta}^* \frac{1}{r}\frac{\partial\bar{\tilde{\zeta}}}{\partial r} rdr \in \int_1^R (L_3^*X^*)\bar{\tilde{\zeta}}\, rdr$$

Collecting the above terms, we then have

$$L_1^*X^* = -\frac{\partial\tilde{u}_r^*}{\partial r} - \frac{in}{r}\tilde{u}_\theta^* = 0 \tag{4.16}$$

$$L_2^*X^* = \frac{in}{r}\tilde{u}_r^* + \frac{\partial\tilde{u}_\theta^*}{\partial r} = 0 \tag{4.17}$$

$$L_3^*X^* = \tilde{u}_\theta^* + (-i\omega_c - \frac{1}{r}\frac{\partial}{\partial r} + in\frac{\mu_c}{r^2})\tilde{\zeta}^* = 0 \tag{4.18}$$

provided that,

$$\left[r\bar{\tilde{u}}_r\tilde{u}_r^* \right]_1^R - \left[r\bar{\tilde{u}}_\theta\tilde{u}_\theta^* \right]_1^R + \left[\bar{\tilde{\zeta}}\tilde{\zeta}^* \right]_1^R = 0 \tag{4.19}$$

when $r = R$, the relation (4.19) gives,

$$R\bar{\tilde{u}}_r(r=R)\tilde{u}_r^*(r=R) - R\bar{\tilde{u}}_\theta(r=R)\tilde{u}_\theta^*(r=R) + \bar{\tilde{\zeta}}(r=R)\tilde{\zeta}^*(r=R) = 0$$

and for $r = 1$, the boundary condition $\tilde{u}_r = \tilde{u}_\theta = 0$, together with relation (4.19) yield

$$\bar{\tilde{\zeta}}(r=1)\ \tilde{\zeta}^*(r=1) = 0$$

in which $\bar{\tilde{\zeta}}(r=1)$ is not zero according to the linear solution. Therefore we obtain:

$$\tilde{\zeta}^*(r=1) = 0$$

Now we proceed to determine the solutions $X^* = (\tilde{u}_r^*(r), \tilde{u}_\theta^*(r), \tilde{\zeta}^*(r))^T$.

The solutions $\tilde{u}_r^*$ and $\tilde{u}_\theta^*$ are obtained by resolving equations (4.16) and (4.17) and read,

$$\tilde{u}_r^* = C_1 e^{in\ln r} + C_2 e^{-in\ln r} \tag{4.20}$$

$$\tilde{u}_\theta^* = -(C_1 e^{in\ln r} - C_2 e^{-in\ln r}) \tag{4.21}$$

where C_1 and C_2 are two non-vanishing constants.

The eigen-function $\tilde{\zeta}^*$ is composed by a homogeneous solution and a particular solution

$$\tilde{\zeta}^* = \tilde{\zeta}_H^* + \tilde{\zeta}_P^* \tag{4.22}$$

Introducing the homogeneous solution into (4.18) lead to,

$$(-i\omega_c - \frac{1}{r}\frac{\partial}{\partial r} + in\frac{\mu_c}{r^2})\tilde{\zeta}_H^* = 0 \tag{4.23}$$

The solution to the equation (4.23) is

$$\tilde{\zeta}_H^* = C_3\tilde{\zeta} \tag{4.24}$$

with

$$\tilde{\zeta}(r) = e^{-\frac{i\omega_c}{2}(r^2-1)+in\mu_c\ln r}$$

and a particular solution is found as

$$\tilde{\zeta}_P^* = \tilde{\zeta}\int_1^r \bar{\tilde{\zeta}}(r_0)\tilde{u}_\theta^*(r_0)r_0 dr_0 \tag{4.25}$$

According to the boundary $\tilde{\zeta}^*(r=1) = 0$, we have $C_3 = 0$, and therefore

$$\tilde{\zeta}^* = \tilde{\zeta}_P^* = \tilde{\zeta}\int_1^r \bar{\tilde{\zeta}}(r_0)\tilde{u}_\theta^*(r_0)r_0 dr_0 \tag{4.26}$$

4.3.3 Second order solutions

At order ε^2, the equation (4.7) leads to the nonhomogeneous problem for the vorticity field $\zeta^{(2)}$,

$$\frac{\partial \zeta^{(2)}}{\partial t}+\frac{1}{r}\frac{\partial \zeta^{(2)}}{\partial r}+\frac{\mu_c}{r^2}\frac{\partial \zeta^{(2)}}{\partial \theta}=-u_r^{(1)}\frac{\partial \zeta^{(1)}}{\partial r}-\frac{u_\theta^{(1)}}{r}\frac{\partial \zeta^{(1)}}{\partial \theta} \tag{4.27}$$

Without loss of generality and in order to avoid a new amplitude different from the amplitude *A* of the most unstable mode, the homogeneous solution $\zeta_h^{(2)}$ of (4.27) is chosen to be orthogonal to the solution of the first order $\zeta^{(1)}$. In the present case, the appropriate scalar product is

$$\prec \zeta_h^{(2)},\zeta^{(1)} \succ=\frac{1}{R}\frac{n}{2\pi}\frac{\omega_c}{2\pi}\int_0^{2\pi/n}\int_1^R\int_0^{2\pi/\omega_c}\zeta_h^{(2)}\overline{\zeta}^{(1)}rdrd\theta dt \tag{4.28}$$

here, in the nonlinear analysis, the overbar $\overline{\zeta}^{(1)}$ means the complex conjugate. The condition of the orthogonality leads to $\zeta_h^{(2)}=0$.

The right side of equation (4.27) suggests to search a particular inhomogeous solution in the following form:

$$\zeta^{(2)}=A^2(t_2)\tilde{\zeta}^{(2,2)}(r)e^{2i\omega_c t-2in\theta}+\left|A(t_2)\right|^2\tilde{\zeta}^{(2,0)}(r)+C.C \tag{4.29}$$

By introducing this form of a particular solution into equation (4.27), $\tilde{\zeta}^{(2,2)}$ and $\tilde{\zeta}^{(2,0)}$ are respectively the solutions of equations:

$$2i\omega_c\tilde{\zeta}^{(2,2)}+\frac{1}{r}\frac{\partial \tilde{\zeta}^{(2,2)}}{\partial r}-2in\frac{\mu_c}{r^2}\tilde{\zeta}^{(2,2)}=-\tilde{u}_r^{(1)}\frac{\partial \tilde{\zeta}^{(1)}}{\partial r}+in\frac{\tilde{u}_\theta^{(1)}}{r}\tilde{\zeta}^{(1)} \tag{4.30}$$

$$\frac{1}{r}\frac{\partial \tilde{\zeta}^{(2,0)}}{\partial r}=-\overline{\tilde{u}}_r^{(1)}\frac{\partial \tilde{\zeta}^{(1)}}{\partial r}+in\frac{\overline{\tilde{u}}_\theta^{(1)}}{r}\tilde{\zeta}^{(1)} \tag{4.31}$$

The solutions of (4.30) and (4.31) are

$$\tilde{\zeta}^{(2,2)}(r)=r\tilde{u}_r^{(1)}\tilde{\zeta}^{(1)} \tag{4.32}$$

$$\tilde{\zeta}^{(2,0)}(r)=-r\tilde{u}_r^{(1)}\overline{\tilde{\zeta}}^{(1)} \tag{4.33}$$

once $\tilde{\zeta}^{(2)}$ is known, we can now proceed to determine $\left\{u_r^{(2)},u_\theta^{(2)}\right\}$.

At order ε^2, equations (4.2a) and (4.2e) become,

$$\frac{\partial (ru_r^{(2)})}{\partial r}+\frac{\partial u_\theta^{(2)}}{\partial \theta}=0 \tag{4.34}$$

$$\frac{1}{r}\frac{\partial(ru_\theta^{(2)})}{\partial r}-\frac{1}{r}\frac{\partial u_r^{(2)}}{\partial\theta}=\zeta^{(2)} \tag{4.35}$$

with boundary conditions:

$$u_r^{(2)}=u_\theta^{(2)}=0 \text{ at } r=1 \tag{4.36}$$

In the same manner, we look for solutions of equations (4.34) - (4.36) in the form:

$$(u_r^{(2)},u_\theta^{(2)})=A^2(t_2)(\tilde{u}_r^{(2,2)}(r),\tilde{u}_\theta^{(2,2)}(r))e^{2i\omega t-2in\theta}+|A(t_2)|^2(\tilde{u}_r^{(2,0)}(r),\tilde{u}_\theta^{(2,0)}(r))+C.C \tag{4.37}$$

After some tedious calculations, the solutions may be written as,

$$\tilde{u}_r^{(2,2)}(r)=-i\left\{F_2+G_2-r^{2n-1}G_2(r=1)\right\} \tag{4.38}$$

$$\tilde{u}_\theta^{(2,2)}(r)=F_2-G_2+r^{2n-1}G_2(r=1) \tag{4.39}$$

$$\tilde{u}_r^{(2,0)}=0 \tag{4.40}$$

$$\tilde{u}_\theta^{(2,0)}=\frac{1}{r}\int_1^r r_0\tilde{\zeta}^{(2,0)}(r_0)dr_0 \tag{4.41}$$

where F_2 and G_2 are defined by

$$F_2(r)=\frac{1}{2}\int_1^r\tilde{\zeta}^{(2,2)}(r_0)(\frac{r_0}{r})^{2n+1}dr_0$$

$$G_2(r)=\frac{1}{2}\int_r^R\tilde{\zeta}^{(2,2)}(r_0)(\frac{r}{r_0})^{2n-1}dr_0$$

4.3.4 Third order solvability condition

At order ε^3, the following system for $(u_r^{(3)},u_\theta^{(3)},\zeta^{(3)})$ is obtained,

$$\begin{aligned}
&\frac{\partial(ru_r^{(3)})}{\partial r}+\frac{\partial u_\theta^{(3)}}{\partial\theta}=0\\
&\frac{1}{r}\frac{\partial(ru_\theta^{(3)})}{\partial r}-\frac{1}{r}\frac{\partial u_r^{(3)}}{\partial\theta}-\zeta^{(3)}=0\\
&\frac{\partial\zeta^{(3)}}{\partial t}+\frac{1}{r}\frac{\partial\zeta^{(3)}}{\partial r}+\frac{\mu_c}{r}\frac{\partial\zeta^{(3)}}{\partial\theta}=RHS\\
&=-\frac{\partial\zeta^{(1)}}{\partial t_2}-\frac{\mu_2}{r}\frac{\partial\zeta^{(1)}}{\partial\theta}-u_r^{(1)}\frac{\partial\zeta^{(2)}}{\partial r}-u_r^{(2)}\frac{\partial\zeta^{(1)}}{\partial r}-\frac{u_\theta^{(1)}}{r}\frac{\partial\zeta^{(2)}}{\partial\theta}-\frac{u_\theta^{(2)}}{r}\frac{\partial\zeta^{(1)}}{\partial\theta}
\end{aligned} \tag{4.42}$$

We use *RHS* to represent all terms on the right hand side in the last expression, and the above equation has a solution if and only if a solvability condition, known as the Fredholm

alternative, is satisfied. This condition states that the right hand side of the above equations must be orthogonal to the linear solution of the adjoint problem obtained in section 4.3.2.

Applying the solvability condition leads to the following amplitude equation,

$$\chi \frac{dA}{dt_2} = (\beta_r + i\beta_i)\mu_2 A - (\delta_r + i\delta_i)A|A|^2 \tag{4.43}$$

the above amplitude equation describes the behavior of the amplitude $A(t_2)$ at the time scale t_2.

The coefficients appearing in equation (4.43) are given by,

$$\chi = \int_1^R \tilde{\zeta}\bar{\tilde{\zeta}}^* r dr \tag{4.44}$$

$$\beta_r + i\beta_i = in\int_1^R \frac{1}{r}\left(\int_1^r \tilde{\zeta}(r_0)\bar{\tilde{u}}_\theta^*(r_0) r_0 dr_0\right) dr \tag{4.45}$$

and

$$\delta_r + i\delta_i = \int_1^R [\tilde{u}_r^{(2,2)} \frac{\partial \bar{\tilde{\zeta}}}{\partial r} + \frac{in\tilde{u}_\theta^{(2,2)}}{r}\bar{\tilde{\zeta}} + \bar{\tilde{u}}_r \frac{\partial \tilde{\zeta}^{(2,2)}}{\partial r} - \frac{2in\bar{\tilde{u}}_\theta}{r}\tilde{\zeta}^{(2,2)} + \tilde{u}_r \frac{\partial}{\partial r}(\tilde{\zeta}^{(2,0)} + \bar{\tilde{\zeta}}^{(2,0)}) - \frac{in\tilde{u}_\theta^{(2,0)}}{r}\tilde{\zeta}]\bar{\tilde{\zeta}}^* r dr \tag{4.46}$$

One can get rid of the small parameter ε by re-introducing the original variables $t_2 = \varepsilon^2 t$, and $\mu_2 = (\mu - \mu_c)/\varepsilon^2$, and substituting εA by A. This yields an equation for the amplitude A in terms of the original time variable t of the landau type with complex coefficients:

$$\frac{dA}{dt} = (\lambda_r + i\lambda_i)\ (\mu - \mu_c)A - (\gamma_r + i\gamma_i)A|A|^2 \tag{4.47}$$

with

$$\lambda_r + i\lambda_i = \frac{\beta_r + i\beta_i}{\chi} \text{ and } \gamma_r + i\gamma_i = \frac{\delta_r + i\delta_i}{\chi}$$

Writing the complex amplitude A in the norm-phase form,

$$A = |A|e^{i\omega_2 t} \tag{4.48}$$

and substituting it in equation (4.47), we get the following equations,

$$\begin{cases} \dfrac{d|A|}{dt} = \lambda_r(\mu - \mu_c)|A| - \gamma_r|A|^3 \\ \omega_2 = \lambda_i(\mu - \mu_c) - \gamma_i|A|^2 \end{cases} \tag{4.49}$$

The physical meaning of these coefficients is: $\lambda_r(\mu - \mu_c)$ is the linear growth rate of the instability above its threshold, $\lambda_i(\mu - \mu_c)$ and $-\gamma_i|A|^2$ represents respectively the linear and

the nonlinear correction of the frequency in the supercritical regime, and the sign of γ_r determines the nature of the bifurcation.

We determined numerically the coefficients λ_r and λ_i for fixed values of the radius ratio *R* and the number *n* of rotating stalls. This allows us to determine the linear growth rate of the instability and the linear correction of its frequency in the unstable regime. Unfortunately and up to now, we did not succeed to determine numerically the coefficients γ_r and γ_i which involve complicated integrals (4.46). This task will be accomplished in a future work.

Depending on the sign of γ_r, two response diagrams to general perturbations are possible:

If $\gamma_r > 0$, the bifurcation is supercritical and therefore the steady solutions to equation (4.49) are:

$$\begin{cases} |A|^2 = \dfrac{\lambda_r}{\gamma_r}(\mu - \mu_c) \\ \omega_2 = (\lambda_i - \gamma_i \dfrac{\lambda_r}{\gamma_r})(\mu - \mu_c) \end{cases} \tag{4.50}$$

In this case, the bifurcation diagram describing the nonlinear behavior of the amplitude of the instability as a function of the distance to criticality $\mu - \mu_c$ is plotted in Figure 4.1. This illustrative figure shows that for a supercritical instability, the critical value μ_c at which instability sets in does not depend on the magnitude of the initial perturbation.

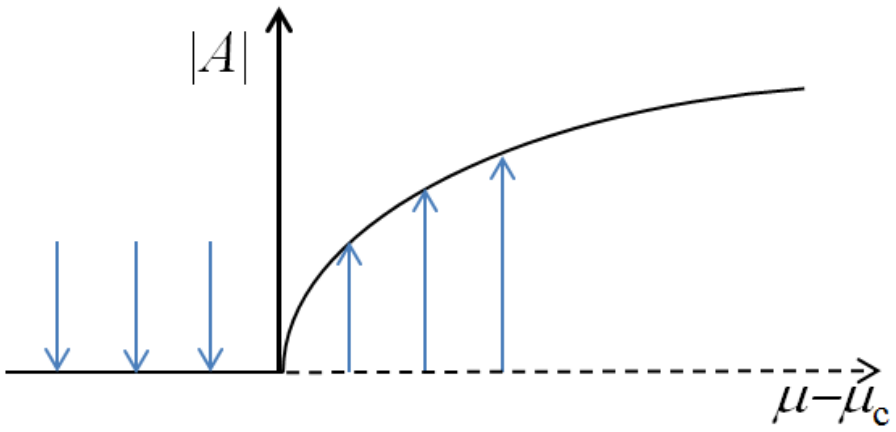

Figure 4.1 Supercritical bifurcation diagram in the case of positive coefficient γ_r (the solid line represents stable solution while the dashed line represents unstable solution)

If $\gamma_r < 0$, the bifurcation is subcritical and the qualitative diagram of bifurcation is illustrated in Figure 4.2. From this figure, one can notice that the instability may be initiated by finite perturbations for $\mu < \mu_c$. Physically it means that the diffuser flow can be disturbed by rotating stall even at an angle larger than the critical one obtained by linear theory. We emphasize here that in the case of a subcritical bifurcation, we need to develop the solutions until the fifth order in the small parameter ε to obtain the amplitude equation.

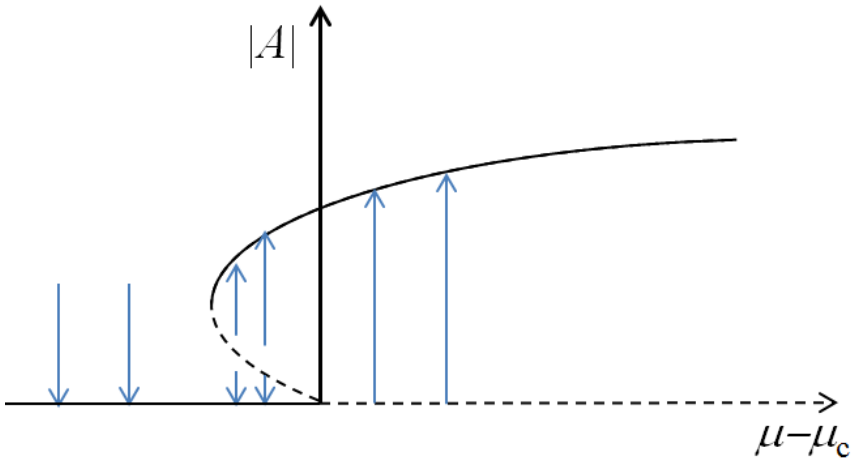

Figure 4.2 Subcritical bifurcation diagram in the case of negative coefficient γ_r (the solid line represents stable solution while the dashed line represents unstable solution)

4.4 Comparison with experimental results

Although the coefficients γ_r and γ_i which give nonlinear corrections have not been numerically solved yet, however, the solved linear coefficients λ_r and λ_i are used to compare with the experimental results to have a first evaluation on this weakly nonlinear stability analysis. It should be noticed that the experimental growth rate of rotating stall is not defined, which means the comparison of the instability growth rate λ_r cannot be made. On the other hand, the experimental angular frequencies of rotating stall have been measured in chapter 2, and because the weakly nonlinear analysis restricts the flow condition very close to the critical stall condition, in order to ensure the distance as small as possible, we take the first two points to determine the experimental slope of the angular frequency, as shown in Figure 4.3. Then, the experimental and theoretical results are compared in Table 4.1.

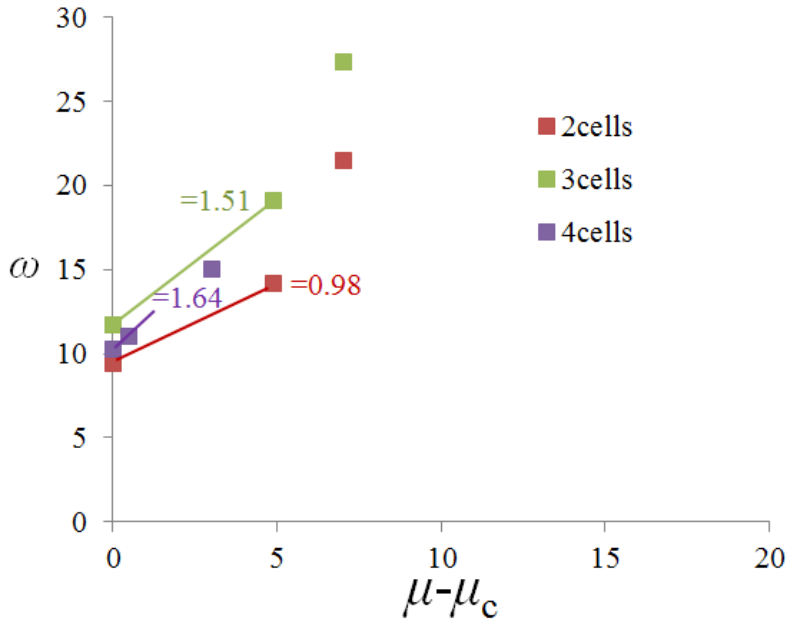

Figure 4.3 Slopes of the experimental angular velocity of rotating stall

Table 4.1 Comparison of the slope of angular frequency

Stall mode (R = 1.5)	Experiment	Theory(λ_i)
n = 2	0.98	1.12
n = 3	1.51	1.79
n = 4	1.64	2.08

It can be seen good agreements are obtained in the comparison: the experimental and theoretical results are very close to each other, and the slope of the angular frequency is larger for mode with more number of cells.

Although the theoretical results are slightly higher than the experimental results, but this may be calibrated by the nonlinear contribution not taken into account in this comparison. A completely comparison is able to be made when the nonlinear coefficient are numerically solved.

Chapter 5 Conclusions and future works

This study was focused on the rotating stall in a wide vaneless diffuser. An experimental study was first performed to measure the impeller and diffuser performance, and to analyze the characteristics of rotating stall. The effect of rotating stall on the diffuser performance was discussed based on the experimental results. A linear stability analysis was introduced to predict the characteristics of rotating stall. The limits and abilities of this linear model were discussed. A nonlinear stability analysis was then introduced. The main conclusions of this study are summarized in this chapter, and future works are suggested.

5.1 Conclusions

Rotating stall in a wide vaneless diffuser has been experimentally studied, 22 flow rates (Q/Q_d = 1.5 → 0.26) were tested. The spectrum analysis showed that rotating stall exists at 5 partial flow rates (Q/Q_d = 0.26, 0.36, 0.47, 0.56, 0.58). It is characterized by low frequency peaks in the spectra, these peaks are related to different stall modes, impeller frequency or harmonics. A dedicated spectrum analysis is then applied to identify the stall frequencies, and the characteristics of rotating stall are summarized as follows:

(1) Three stall modes are identified at the five partial flow rates: n = 2, 3 and 4, and these different stall modes can coexist at one given operating condition.

(2) The propagation velocity increases with the decrease of the flow rate, and the modes with fewer cells propagate faster than modes with more cells.

(3) The amplitude analysis showed that the dominant stall mode varies with the flow rate from n = 4 (Q/Q_d = 0.58, 0.56, 0.47) → n = 2 (Q/Q_d = 0.36) → n = 3 (Q/Q_d = 0.26).

The diffuser performance is clearly affected by the occurrence of rotating stall. An analysis associating the effect of rotating stall to the losses in the vaneless diffuser is presented. The isentropic pressure recovery curve from diffuser inlet to outlet and the experimental pressure recovery curve are plotted, and then the definition of the "losses" is proposed to be the difference between the two curves at the diffuser outlet. In general, the losses in the vaneless diffuser at stable conditions are divided into three parts: diffusion losses, mixing losses and friction losses. In the present case, the diffusion losses and mixing losses are neglected due to the conclusions presented by Aungier (1993) and Dou (1991), and the friction losses are assumed to be the main losses in the vaneless diffuser. The diffuser loss coefficient is then defined. The theoretical analysis showed that the loss coefficient is a linear function of the length of the streamline in the vaneless diffuser, with a slope equal to λ/D_H. This is confirmed by the experimental results which show that the loss increases linearly with the length of streamline with a slope nearly equal to the theoretical prediction. This agreement proved that the friction losses are the main source of losses in the vaneless diffuser, and it is then defined as the normalized losses and used to evaluate the diffuser losses at stable conditions.

The comparison shows that, in unstable conditions, the normalized losses are much higher than the actual losses measured in the experiment. It is then concluded that the occurrence of

rotating stall decreased the diffuser losses, and the diffuser performance is increased. Two reasons are proposed to explain such a result:

(1) First, the topology of stall cells obtained from previous PIV results shows that each stall cell generated a blockage area, which leads to an increase of the radial velocity component in the vaneless diffuser. Consequently, the increased flow angle shortens the length of the streamline, and then the friction losses are decreased due to the shorter flow path. The new estimation for the diffuser losses, based on the calibrated length of streamline, has been compared to the experimental results, and a good agreement is obtained.

(2) Second, rotating stall is characterized by inward flows which come from the diffuser downstream. It convects fluid with a pressure which is higher than the one in the diffuser, and high pressure flow mixed with the diffuser flow at the stall region. As a consequence, the measured time averaged pressure could be increased.

A linear stability analysis is then proposed to predict the characteristics of rotating stall. According to the experiment setup, it is assumed that the flow is two dimensional, the fluid is incompressible and inviscid, and the static pressure is uniform at diffuser outlet. The linear model is constructed based on the continuity, momentum and vorticity equations. By specifying the diffuser radius ratio and the number of stall cells, the model is able to calculate the critical flow angle and the propagation velocity of the specified stall mode. To verify the model, the results have been compared to the results presented by Tsujimoto et al (1996), and good agreements, in terms of order of magnitude, are obtained in terms of critical flow angle, propagation velocity, velocity and pressure fluctuation distributions. The linear stability analysis has been extended to unstable conditions to study if the most unstable mode is able to predict the dominant stall mode in experiment. However, the theoretical prediction gives the mode $n = 4$ as the most unstable one whatever the operating condition is, which contrasts with dominant stall modes observed in experiment ($n = 4 \rightarrow n = 2 \rightarrow n = 3$ when the flow rate is decreased). It is concluded that the present linear stability study well predicted the stall inception, the calculated critical flow angle, propagation velocity of stall cells, velocity and pressure fluctuation are well verified by the results found in the literatures, but it fails to predict the dominant stall mode, probably due to the nonlinear mode combinations which are neglected.

An analysis of the kinetic energy of the perturbed flow showed that the growth rate of the rotating instability can be decomposed in two terms associated with the radial and tangential velocity components of the steady flow (another term associated with the pressure is found to have no contribution to the instability). The radial velocity component has a stabilizing effect on the flow and the tangential velocity one has a destabilizing effect on the flow. This confirmed the importance of the flow angle on the occurrence of rotating stall. An additional discussion based on the characteristics times of a perturbation convection in radial and tangential directions well explained why the stall mode is developing, the relation between the two time scales determines the possibility of developing of stall mode. It also explained why the radial and tangential velocity components play a key role in the determination of the

occurrence of rotating stall. This analysis showed that the instability is more likely to happen in large radius ratio diffuser because in this case, the time needed for a perturbation to go out from the diffuser is longer, and the instability is developing first for high number of modes because the more is the number of mode, the less is the distance between two cells.

Since the linear stability analysis is limited to predict the dominant stall mode, a nonlinear analysis is developed to take the nonlinear combinations into account. The analysis has been extended to the third order: the first order is the same problem as the linear stability analysis, the second order has been solved, and the third order equations are proposed.

5.2 Future works

1. The linear stability analysis fails to predict the dominant stall mode in experiment, but the predictions for R =2 and 2.5 indicated that the dominant mode varies with the flow rate; this is a motivation to perform new experiments to validate the prediction and to get more comprehensive conclusions on the growth rate.

2. The boundary conditions are supposed to be axisymmetric in the present analysis. An extension of the present study taking into account a velocity profile at inlet and a pressure distribution at outlet more representative of the experimental conditions could give some interesting results.

3. The third order equations of the nonlinear stability analysis have been proposed, but the integrations have not been done in the present work. Dedicated mathematical or numerical solutions will be needed to get the numerical results and finish this non-linear analysis.

4. The present study is focused on the wide vaneless diffuser rotating stall which is associated with a two dimensional core flow instability. This condition is especially important for the present study because this is the base of the hypothesis needed to build the stability model. However, in the literature, there is no consistent conclusion to classify the “narrow” or “wide” vaneless diffuser, except that this classification is linked with the thickness of the boundary layers. Concerning the development of the boundary layers, it will be interesting to perform extensive experimental studies in various vaneless diffusers for various operating point to define which are the key parameters which will lead to one type of rotating stall or another.

Appendix A Diffuser leakages

A.1 Diffuser upper side leakage

The diffuser upper side leakage is defined as follow

$$Q_{L2U} = S_U \bullet V_{z,upper} \tag{A.1}$$

Here, S is the cross sectional area of the gap at upper side,

$$S_U = \pi(r_3^2 - r_2^2) \tag{A.2}$$

and $V_{z,upper}$ is the z axis velocity component at the upper side clearance,

$$V_{z,upper} = \pm \sqrt{\frac{2 \bullet \Delta P_{upper}}{(\frac{Ra \bullet l}{D_H} + K_1 + K_2)\rho}} \tag{A.3}$$

The sign depends on diffuser upper side pressure is higher or lower than the atmosphere pressure. In which ΔP_{upper} is the pressure difference between the diffuser upper side and the atmosphere pressure. l is the axial length of the clearance on the upper side: l = 6 mm. According to Cherdieu (2013), K_1 = 0.5 and K_2 = 1.

A.2 Diffuser lower side leakage

In the same manner with the diffuser upper side leakage, the lower side leakage is defined by

$$Q_{L2U} = S_L \bullet V_{z,lower} \tag{A.4}$$

where $S_L = S_U$, and $V_{z,lower}$ is the z axis velocity component at the lower side clearance,

$$V_{z,lower} = \sqrt{\frac{2\Delta P_{lower}}{(K_1 + K_2 + 2K_3)\rho}} \tag{A.5}$$

where ΔP_{lower} is the pressure difference between the diffuser lower side and the atmosphere pressure, and K_3 = 1.13.

The final results are given in Table A1.

Table A1 Leakage flow in the vaneless diffuser

Q/Q_d	Q_{L2U}	Q_{L2L}	Q_{L2}	Q_D/Q_d
0.26	0.0058	0.0066	0.0124	0.32
0.36	0.0066	0.0070	0.0136	0.41
0.47	0.0068	0.0068	0.0136	0.53
0.56	0.0062	0.0057	0.0119	0.61
0.58	0.0063	0.0059	0.0122	0.63
0.61	0.0063	0.0058	0.0121	0.66
0.63	0.0062	0.0057	0.0120	0.68
0.68	0.0052	0.0050	0.0102	0.73
0.71	0.0063	0.0056	0.0119	0.76
0.71	0.0062	0.0057	0.0119	0.76
0.75	0.0057	0.0051	0.0108	0.79
0.74	0.0048	0.0047	0.0095	0.78
0.82	0.0064	0.0055	0.0119	0.87
0.86	0.0066	0.0056	0.0122	0.91
0.94	0.0060	0.0053	0.0113	0.99
0.95	0.0065	0.0055	0.0120	1.00
0.98	0.0060	0.0051	0.0111	1.03
1.07	0.0064	0.0054	0.0118	1.11
1.04	0.0066	0.0054	0.0120	1.09
1.15	0.0059	0.0047	0.0106	1.2
1.38	0.0056	0.0046	0.0102	1.42
1.53	0.0058	0.0047	0.0106	1.57

Appendix B Frequency spectra

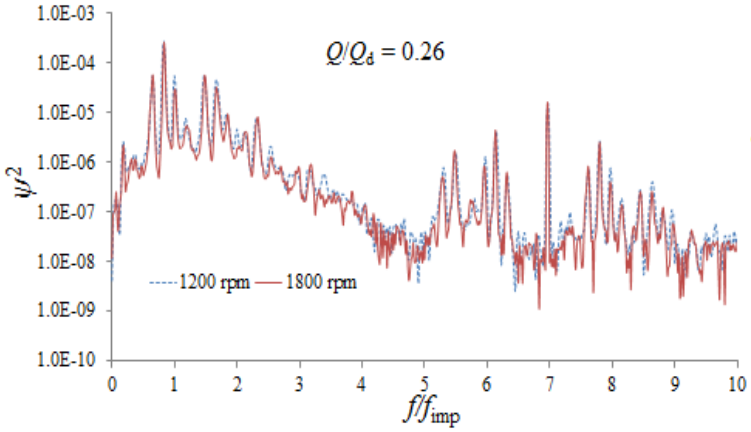

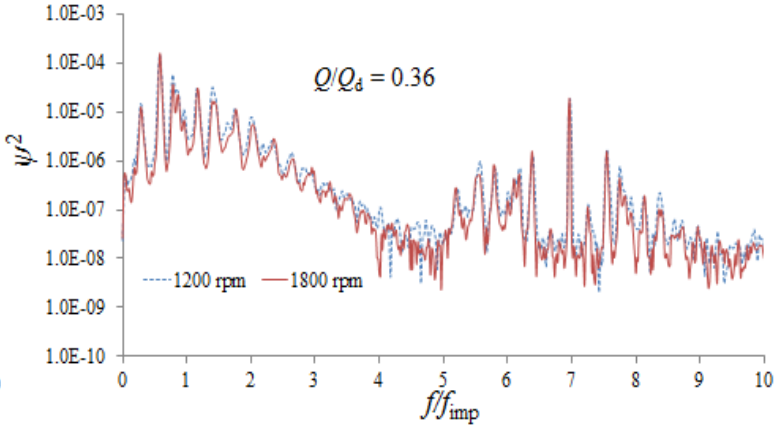

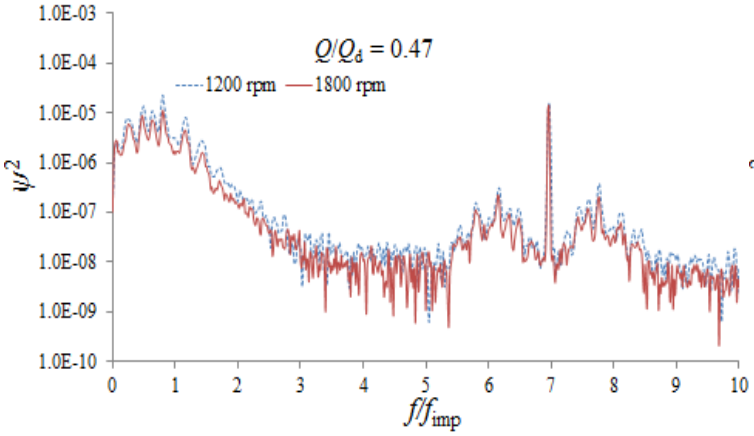

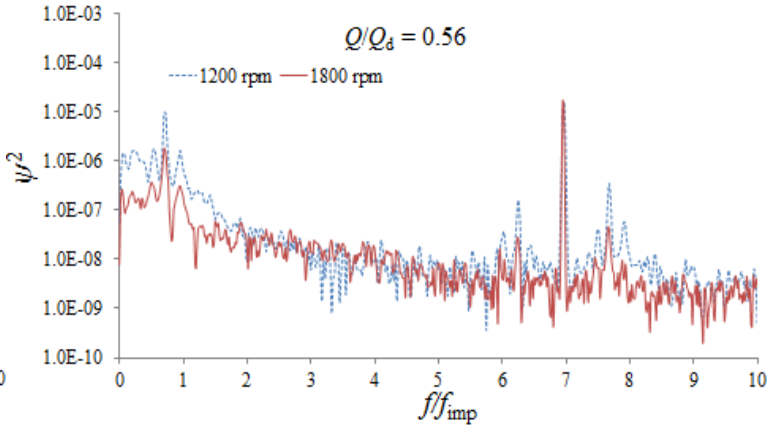

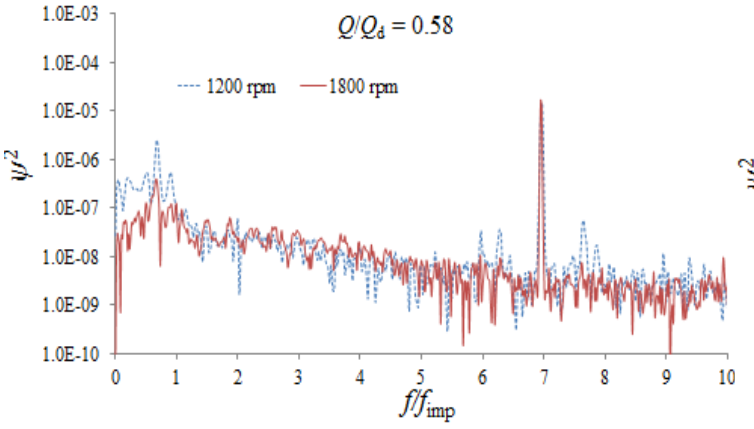

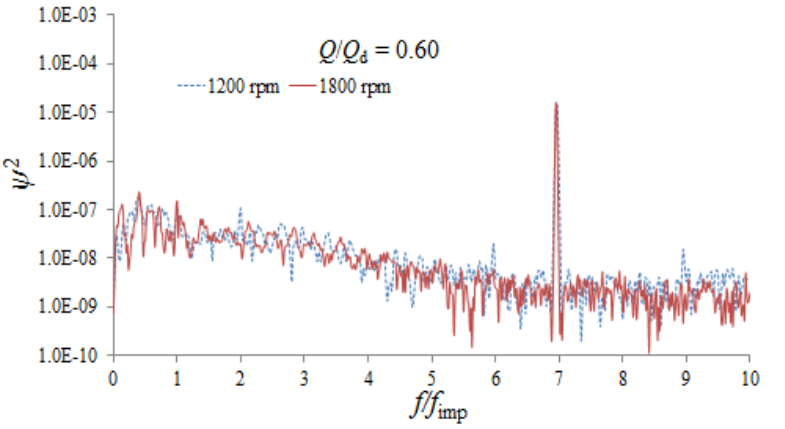

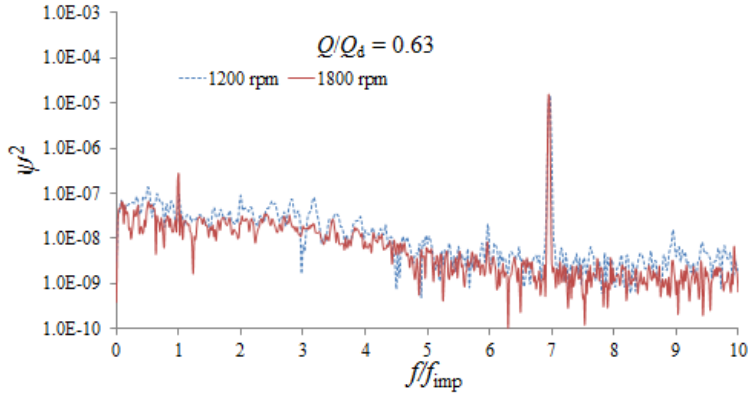
Q/Q_d = 0.63
1200 rpm
1800 rpm
ψ^2
f/f_{imp}

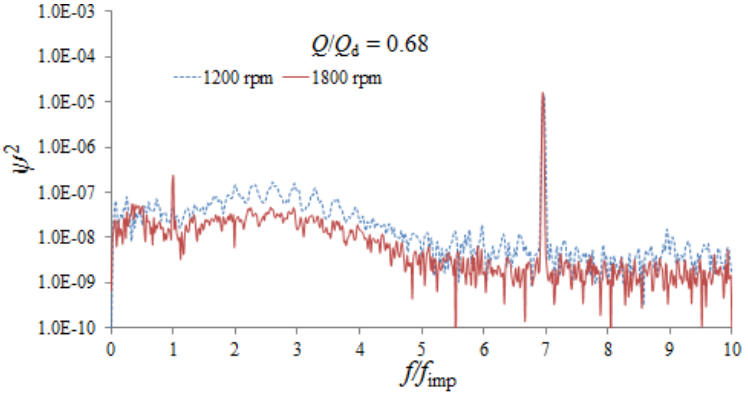
Q/Q_d = 0.68
1200 rpm
1800 rpm
ψ^2
f/f_{imp}

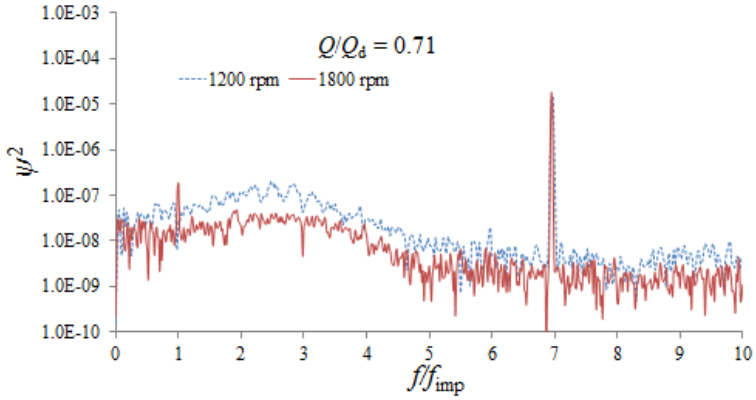
Q/Q_d = 0.71
1200 rpm
1800 rpm
ψ^2
f/f_{imp}

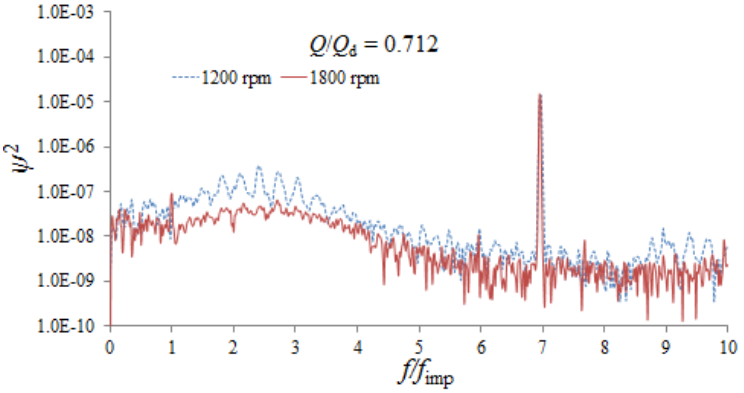
Q/Q_d = 0.712
1200 rpm
1800 rpm
ψ^2
f/f_{imp}

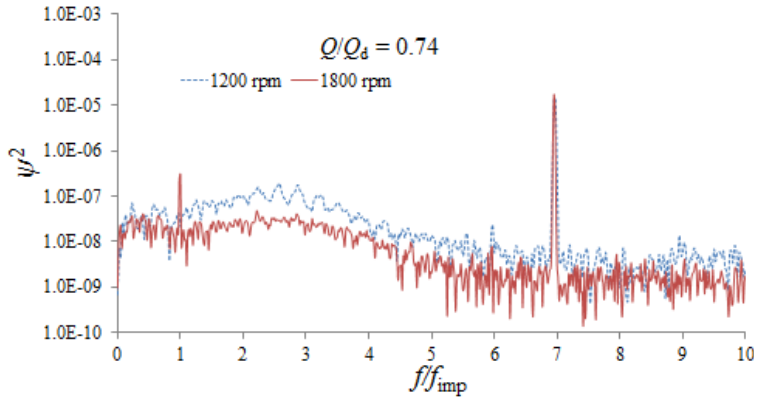
Q/Q_d = 0.74
1200 rpm
1800 rpm
ψ^2
f/f_{imp}

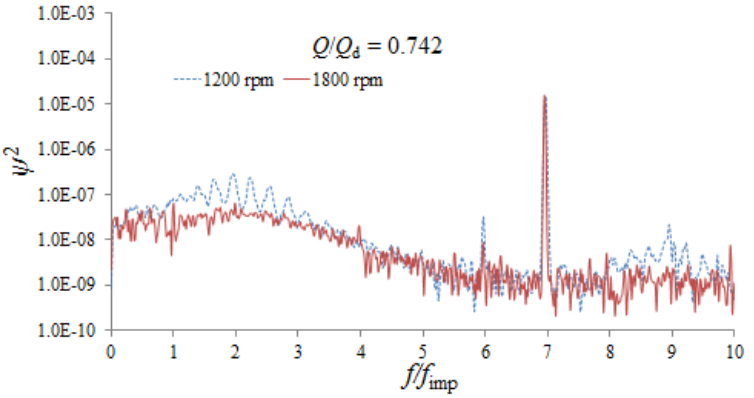
Q/Q_d = 0.742
1200 rpm
1800 rpm
ψ^2
f/f_{imp}

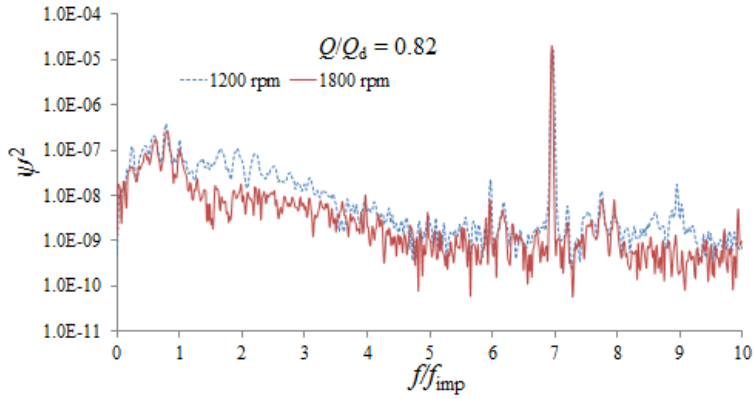
Q/Q_d = 0.82
1200 rpm
1800 rpm
ψ^2
f/f_{imp}

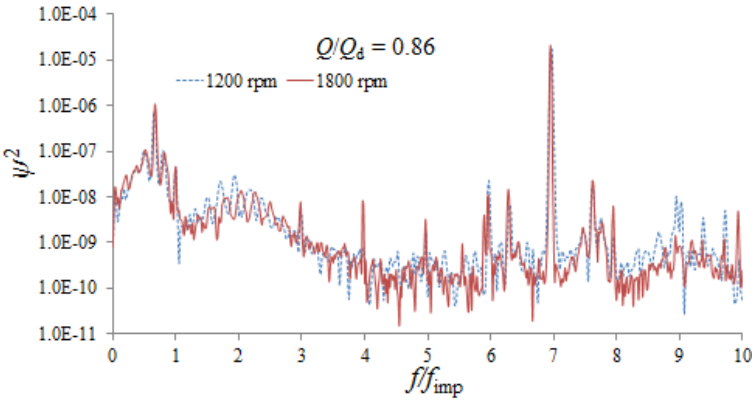
Q/Q_d = 0.86
1200 rpm
1800 rpm
ψ^2
f/f_{imp}

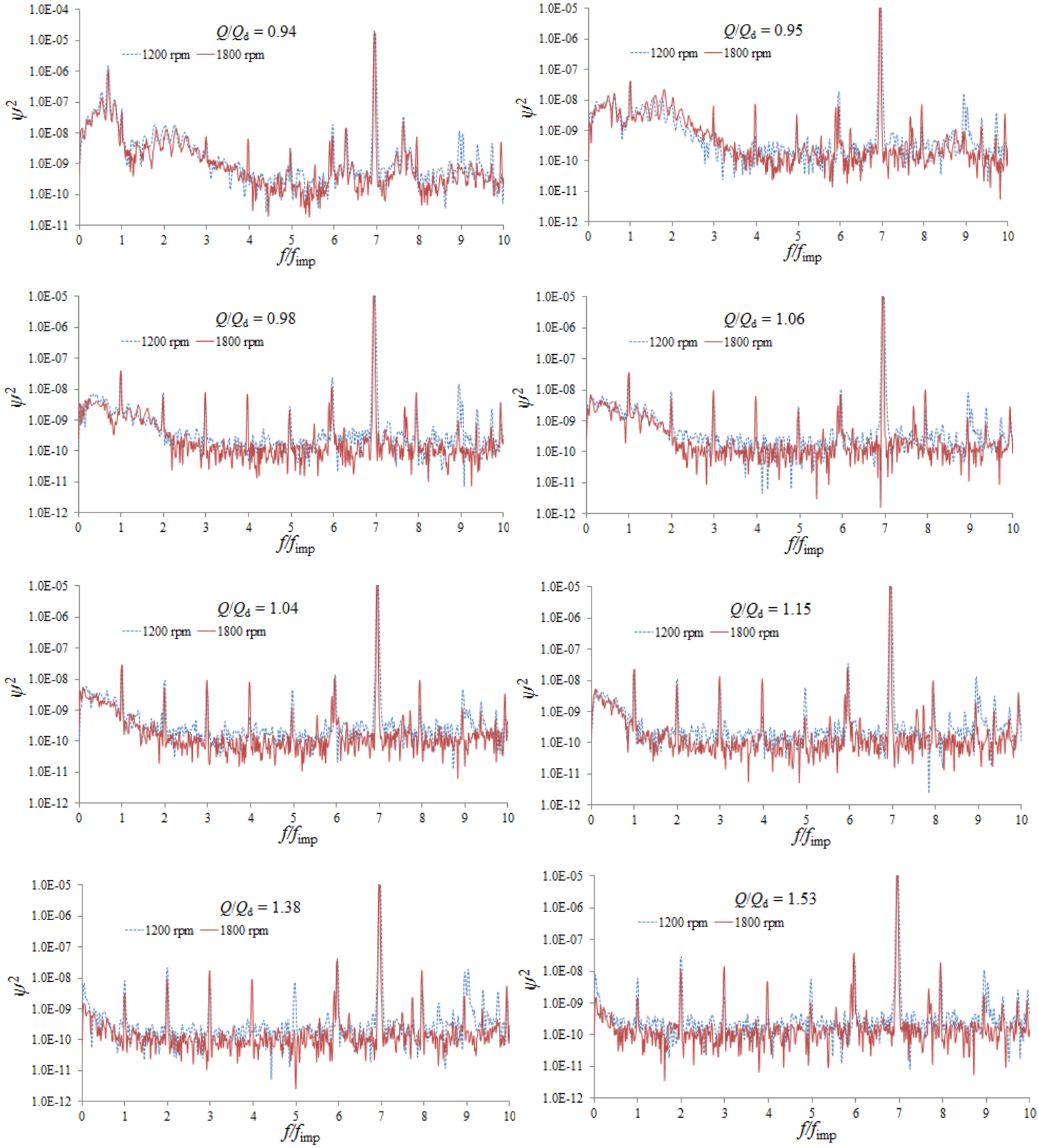

Figure B1 Crosspower spectra at all tested flow rates

Appendix C Spectrum analysis

Table C1 Spectrum analysis at $Q/Q_d = 0.26$

$Q/Q_d = 0.26$				
Amplitude (Pa^2)	Frequency (Hz)	Phase difference (º)	Classification	Number of stall cells
410	16.5	222	Rotating stall	3
87.2	13	150	Rotating stall	2
82.6	20	62.6	Impeller frequency	/
82.1	29.5	– 9	Nonlinear interaction	/
69.8	33	– 83.7	Harmonic	/

Table C2 Spectrum analysis at $Q/Q_d = 0.36$

$Q/Q_d = 0.36$				
Amplitude (Pa^2)	Frequency (Hz)	Phase difference (º)	Classification	Number of stall cells
221	11.5	149	Rotating stall	2
84.3	15.5	223	Rotating stall	3
47.6	27	–14	Nonlinear interaction	/
43.5	23	59	Harmonic	/

Table C3 Spectrum analysis at $Q/Q_d = 0.47$

$Q/Q_d = 0.47$				
Amplitude (Pa^2)	Frequency (Hz)	Phase difference (º)	Classification	Number of stall cells
34.2	16	298	Rotating stall	4
20	10	152	Rotating stall	2
16	12.5	223	Rotating stall	3
11.9	23	–13	Harmonic	/

Table C4 Spectrum analysis at $Q/Q_d = 0.56$

$Q/Q_d = 0.56$				
Amplitude (Pa^2)	Frequency (Hz)	Phase difference (º)	Classification	Number of stall cells
13.89	14	300	Rotating stall	4

Table C5 Spectrum analysis at $Q/Q_d = 0.58$

$Q/Q_d = 0.58$				
Amplitude (Pa^2)	Frequency (Hz)	Phase difference (º)	Classification	Number of stall cells
3.63	13.5	305	Rotating stall	4

Appendix D Pressure recovery

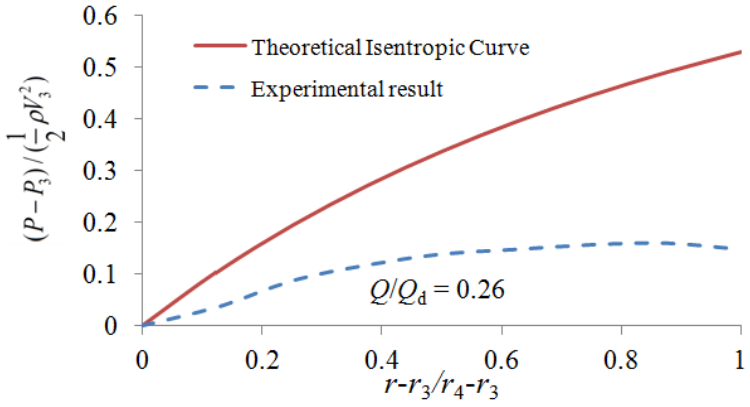

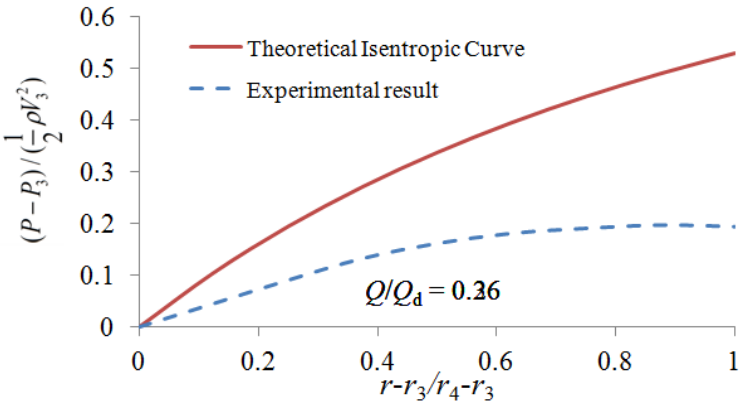

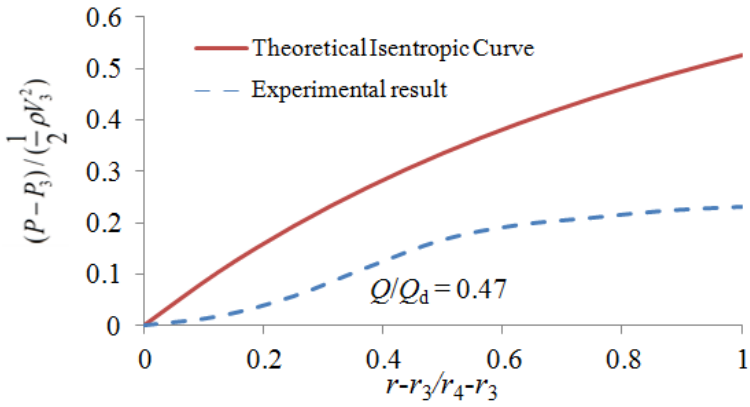

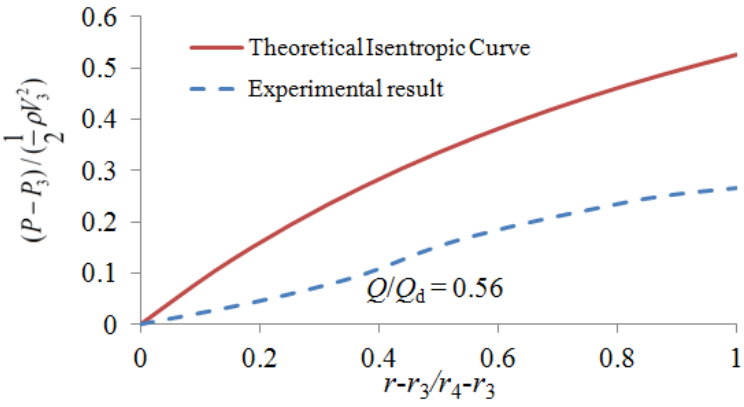

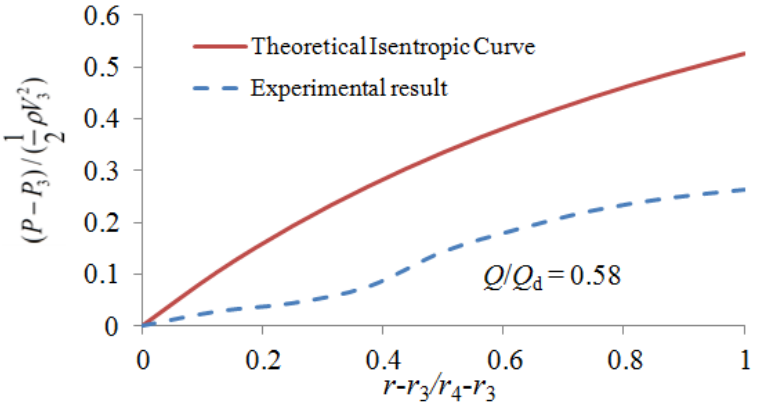

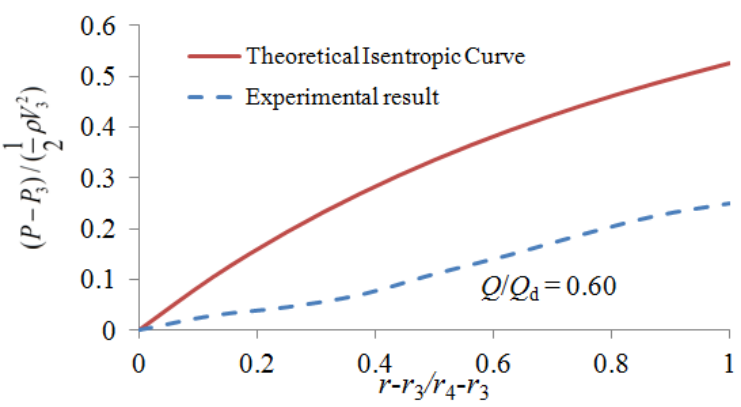

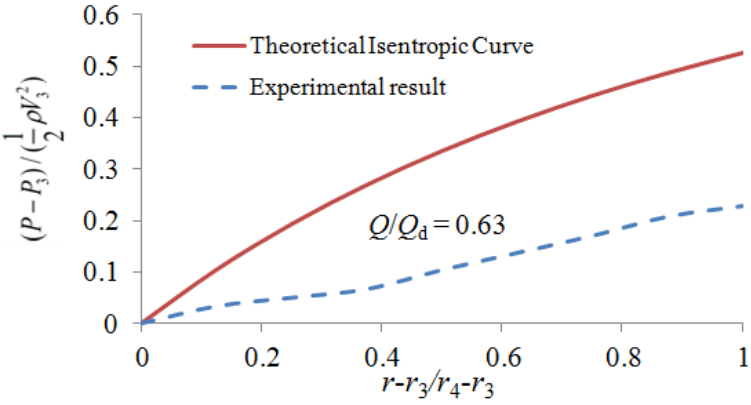
Theoretical Isentropic Curve
Experimental result
$Q/Q_d = 0.63$
$(P-P_3)/(\frac{1}{2}\rho V_3^2)$
$r\text{-}r_3/r_4\text{-}r_3$

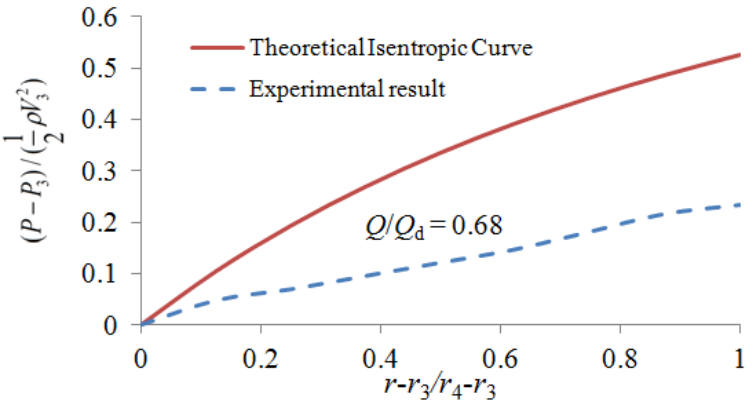
Theoretical Isentropic Curve
Experimental result
$Q/Q_d = 0.68$
$(P-P_3)/(\frac{1}{2}\rho V_3^2)$
$r\text{-}r_3/r_4\text{-}r_3$

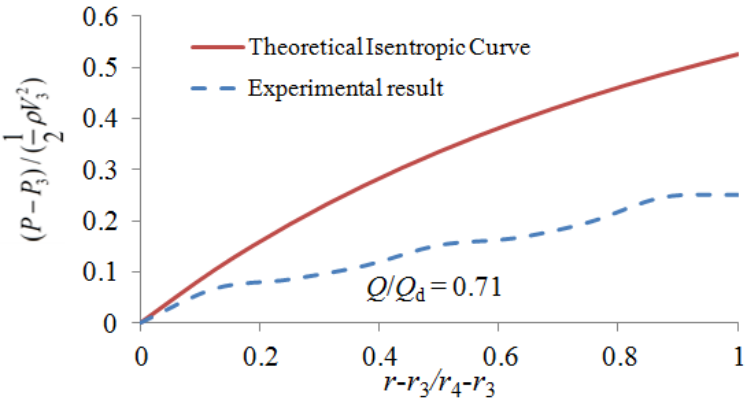
Theoretical Isentropic Curve
Experimental result
$Q/Q_d = 0.71$
$(P-P_3)/(\frac{1}{2}\rho V_3^2)$
$r\text{-}r_3/r_4\text{-}r_3$

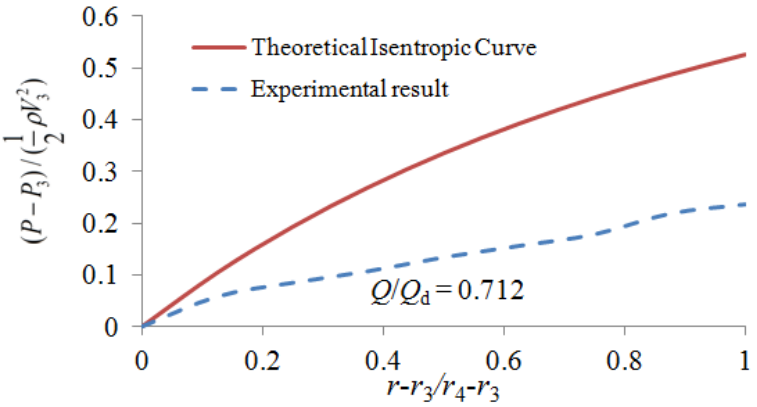
Theoretical Isentropic Curve
Experimental result
$Q/Q_d = 0.712$
$(P-P_3)/(\frac{1}{2}\rho V_3^2)$
$r\text{-}r_3/r_4\text{-}r_3$

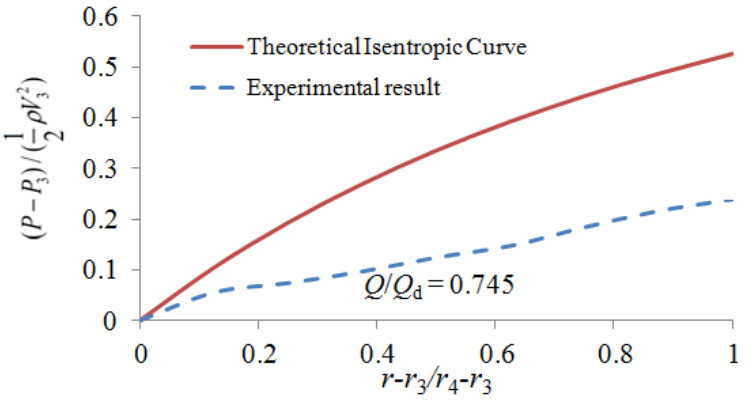
Theoretical Isentropic Curve
Experimental result
$Q/Q_d = 0.745$
$(P-P_3)/(\frac{1}{2}\rho V_3^2)$
$r\text{-}r_3/r_4\text{-}r_3$

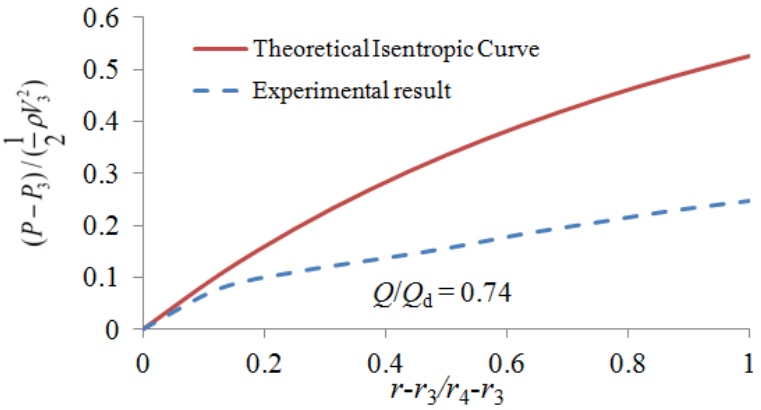
Theoretical Isentropic Curve
Experimental result
$Q/Q_d = 0.74$
$(P-P_3)/(\frac{1}{2}\rho V_3^2)$
$r\text{-}r_3/r_4\text{-}r_3$

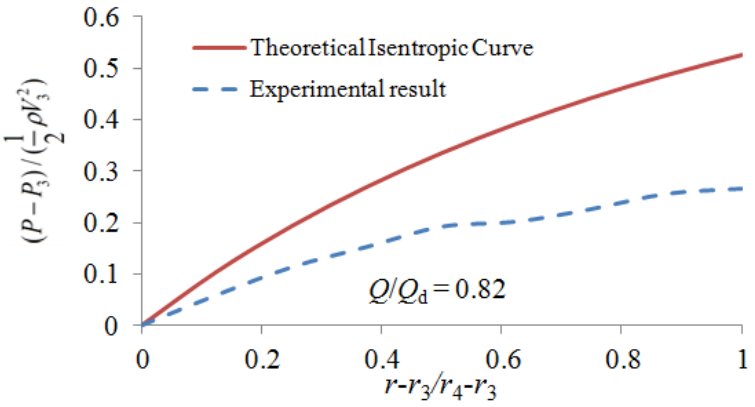
Theoretical Isentropic Curve
Experimental result
$Q/Q_d = 0.82$
$(P-P_3)/(\frac{1}{2}\rho V_3^2)$
$r\text{-}r_3/r_4\text{-}r_3$

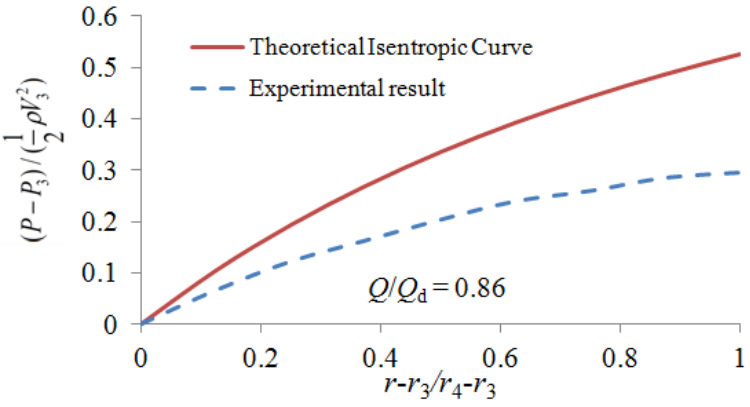
Theoretical Isentropic Curve
Experimental result
$Q/Q_d = 0.86$
$(P-P_3)/(\frac{1}{2}\rho V_3^2)$
$r\text{-}r_3/r_4\text{-}r_3$

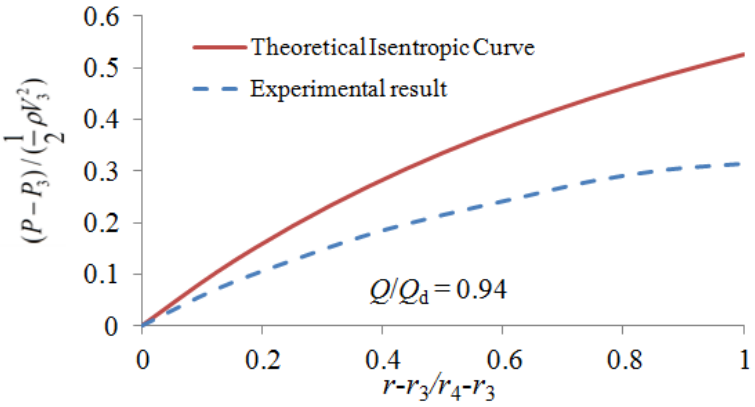
Theoretical Isentropic Curve
Experimental result
$Q/Q_d = 0.94$
$(P-P_3)/(\frac{1}{2}\rho V_3^2)$
$r\text{-}r_3/r_4\text{-}r_3$

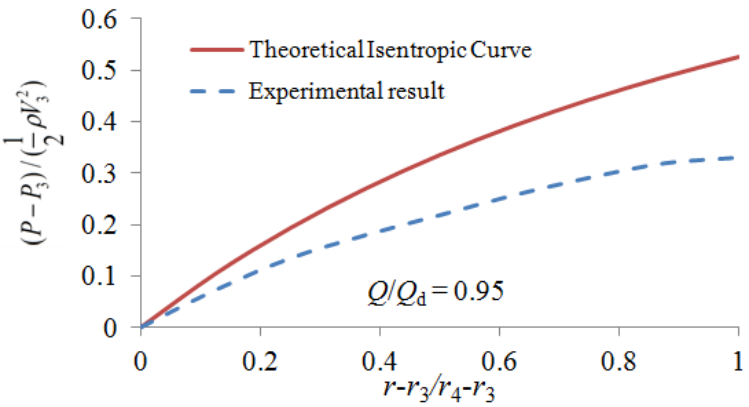
Theoretical Isentropic Curve
Experimental result
$Q/Q_d = 0.95$
$(P-P_3)/(\frac{1}{2}\rho V_3^2)$
$r\text{-}r_3/r_4\text{-}r_3$

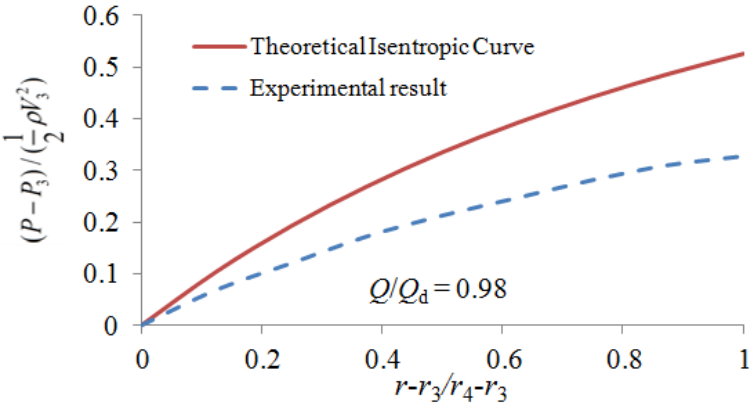
Theoretical Isentropic Curve
Experimental result
$Q/Q_d = 0.98$
$(P-P_3)/(\frac{1}{2}\rho V_3^2)$
$r\text{-}r_3/r_4\text{-}r_3$

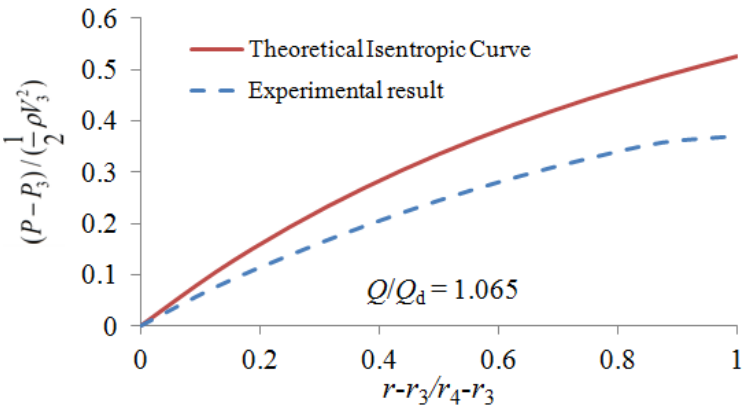
Theoretical Isentropic Curve
Experimental result
$Q/Q_d = 1.065$
$(P-P_3)/(\frac{1}{2}\rho V_3^2)$
$r\text{-}r_3/r_4\text{-}r_3$

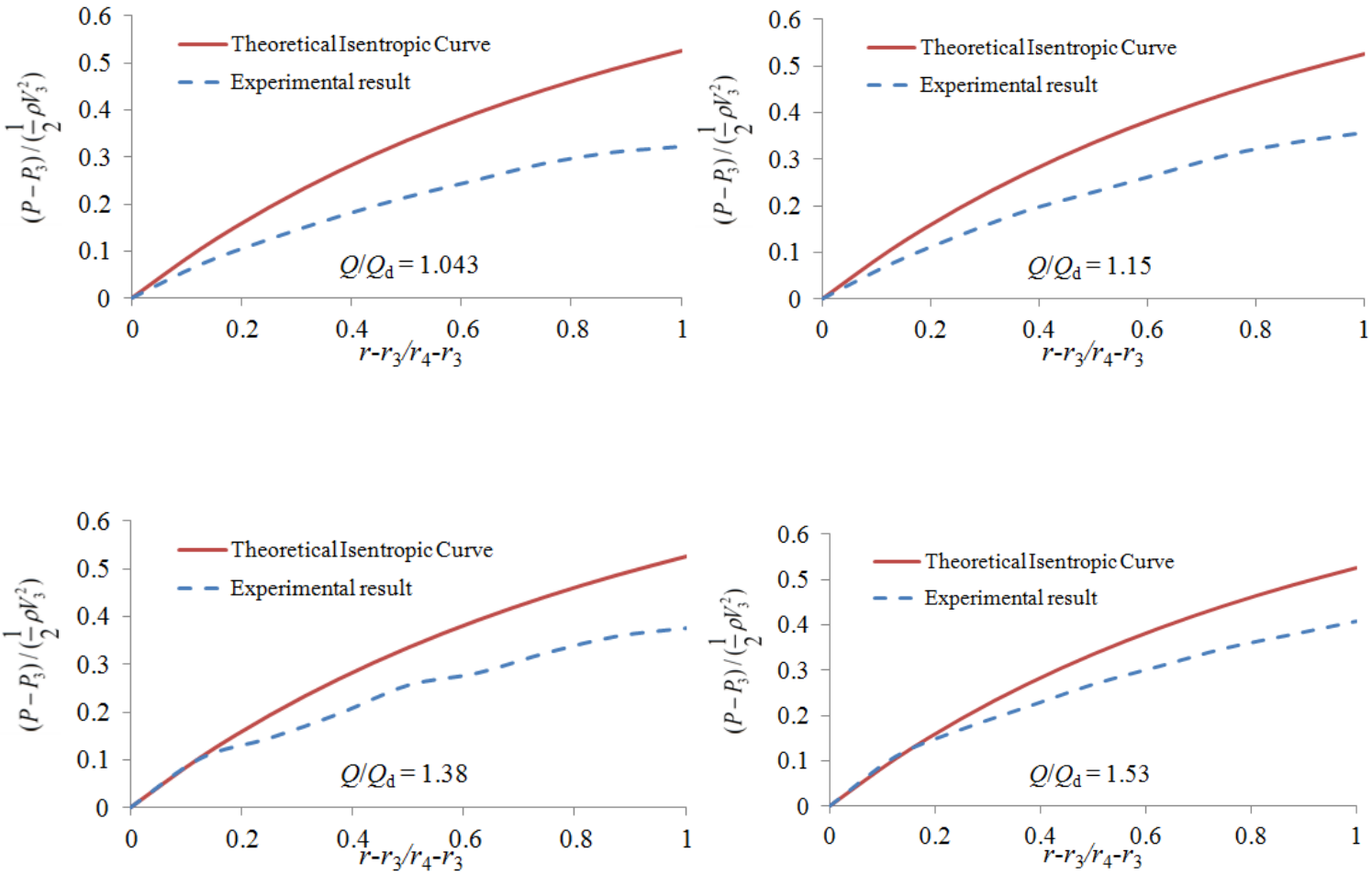

Figure D1 Theoretical and experimental pressure recovery in the vaneless diffuser

Table D1 Loss coefficients at diffuser outlet

Q/Q_d	L	ε	Q/Q_d	L	ε
0.26	3.00	0.38	0.74	0.87	0.29
0.36	2.14	0.33	0.82	0.76	0.26
0.47	1.56	0.30	0.86	0.72	0.23
0.56	1.26	0.26	0.94	0.63	0.21
0.58	1.20	0.26	0.95	0.62	0.20
0.61	1.14	0.28	0.98	0.59	0.20
0.63	1.08	0.30	1.04	0.54	0.20
0.68	0.97	0.29	1.06	0.52	0.16
0.71	0.93	0.29	1.15	0.46	0.17
0.71	0.92	0.28	1.38	0.34	0.15
0.74	0.88	0.28	1.53	0.29	0.12

Bibliography

[1] Abdelhamid, A. N., and Bertrand, J. (1979). Distinctions between two types of self-excited gas oscillations in vaneless radial diffusers. ASME Paper 79-GT-58.

[2] Abdelhamid, A. N., Colwell, W. H., and Barrows, J. F. (1979). Experimental investigation of unsteady phenomena in vaneless radial diffusers. Transactions of the ASME, 101: 52 - 59

[3] Abdelhamid, A. N. (1980). Analysis of rotating stall in vaneless diffusers of centrifugal compressors. ASME Paper 80-GT-184.

[4] Abdelhamid, A. N. (1981). Effects of vaneiess diffuser geometry on flow instability in centrifugal compression systems. ASME Paper 81-GT-10.

[5] Abidogun, K. B., and Ahmed, S. A. (2000). Experimental investigation of rotating stall characteristics in a radial vaneless diffuser. ASME 2000 International Pipeline Conference, Calgary, Canada, Paper No. IPC2000 - 258, 8 pages.

[6] Abidogun, K. B. (2006). Effects of vaneless diffuser geometries on rotating stall. Journal of Propulsion and Power, 22(3): 542 – 449.

[7] Ahmed, S. A. (2008). Control of stall in a radial diffuser using rough surfaces. Canadian Aeronautics and Space Journal, 54(1): 9-15.

[8] Arnulfi, G. L., Micheli, D., and Pinamonti, P. (1996). Experimental investigation on rotating stall in a centrifugal blower with two and four stages and vaneless diffusers. ASME Paper 96-GT-171.

[9] Aungier, R. H. (1993). Aerodynamic design and analysis of vaneless diffusers and return channels. ASME 1993 International Gas Turbine and Aeroengine Congress and Exposition, Paper No: 93-GT-101, pp. V001T03A042; 8 pages. Cincinnati, USA. doi : 10.1115/93-GT-101.

[10] Bianchini, A., Biliotti, D., Ferrara, G., Belardini, E., Giachi, M., Tapinassi, L., and Vannini, G. (2013). A systematic approach to estimate the impact of the aerodynamic force induced by rotating stall in a vaneless diffuser on the rotordynamic behavior of centrifugal compressors. Journal of Engineering for Gas Turbines and Power, 135: 112502-1 - 112502-9.

[11] Bianchini, A., Biliotti, D., Rubino, D. T., Ferrari, L., Ferrara, G. (2015). Experimental analysis of the pressure field inside a vaneless diffuser from rotating stall inception to surge. ASME Journal of Turbomachinery, 137: 111007-1 – 111007-10.

[12] Biliotti, D., Bianchini, A., Vannini, G., Belardini, E., Giachi, M., Tapinassi, L., Ferrari, L., Ferrara, G. (2015). Analysis of the rotordynamic response of a centrifugal compressor subject to aerodynamic loads due to rotating stall. ASME Journal of Turbomachinery, 137: 021002-1 - 021002-8.

[13] Camp, T. R., and Day, I. J. (1997). A study of spike and modal stall phenomena in a low-speed axial compressor. ASME Paper 97-GT-526.

[14] Cavazzini, G. (2007). *Experimental and numerical investigation of the rotor-stator intercation in radial turbomachines*. PhD thesis, Università Degli Studi di Padova, Italy.

[15] Cherdieu, P. (2013). *Contrôle du décollement dans un diffuseur aubé de turbomachine centrifuge (in French)*. PhD thesis, Ecole Centrale de Lille, France.

[16] Crevel, F., Gourdain, N., and Moreau, S. (2014). Numerical simulation of aerodynamic instabilities in a multistage high-speed high-pressure compressor on its test-rig – part i: rotating stall. ASME Journal of Turbomachinery, 136: 101003-1 – 101003-14.

[17] Cumpsty, N. A. (1989). Compressor Aerodynamics, Wiley, New York, pp. 266-309.

[18] Day, I. J. (1993). Stall inception in axial compressors. Journal of Turbomachinery, 115(1): 1-9.

[19] Day, I. J., Breuer, T., Escuret, J., Cherett, M., and Wilson, A. (1999). Stall inception and the prospects for active control in four high-speed compressors. Journal of Turbomachinery, 121(1): 18-27.

[20] Dazin, A., Coudert, S., Dupont, P., Caignaert, G., and Bois, G. (2008). Rotating instability in the vaneless diffuser of a radial flow pump. Journal of Thermal Science, 17(4):368–374.

[21] Dazin, A., Cavazzini, G., Pavesi, G., Dupont, P., Coudert, S., Ardizzon, G., Caignaert, G., and Bois, G. (2011). High-speed stereoscopic PIV study of rotating instabilities in a radial vaneless diffuser. Experiments in Fluids, 51: 83-93.

[22] Dean, Jr. R. C., and Senoo, Y. (1960). Rotating wakes in vaneless diffusers. Journal of Basic Engineering, 82(3): 563-570.

[23] Den, G., N. (1960). The effects of relative width of fixed part on the work of centrifugal stages with vaneless diffusers. Power-Machine-building, (in Russian), 11: 20 – 24.

[24] Dodds, J., and Vahdati, M. (2015). Rotating stall observations in a high speed compressor-part II: numerical study. ASME Journal of Turbomachinery, 137: 051003-1 – 051003-10.

[25] Dou, H. S. (1989). A method of predicting the energy losses in vaneless diffusers of centrifugal compressors. ASME Paper 89-GT-158.

[26] Dou, H. S. (1991). Investigation of the prediction of losses vaneless diffusers. ASME Paper 91-GT-323.

[27] Dou, H. S., and Mizuki, S. (1998). Analysis of the flow in vaneless diffusers with large width-to-radius ratios. Jounal of Turbomachinery, 120: 193-201.

[28] Drazin, P. G. and Reid, W. H. (1981). Hydrodynamic Stability. Cambridge University Press, London.

[29] Ferrara, G., Ferrari, L., and Baldassarre. (2004). Rotating stall in centrifugal compressor vaneless diffuser: experimental analysis of geometrical parameters influence on phenomenon evolution. International Journal of Rotating Machinery, 10(6): 433-442.

[30] Frigne, P., and Van Den Braembussche, R. (1984). Distinction between different types of impeller and diffuser rotating stall in a centrifugal compressor with vaneless diffuser. Journal of Engineering for Gas Turbines and Power, 106: 468-474.

[31] Fringe, P., and Van den Braembussche, R. (1985). A theoretical model for rotating stall in the vaneless diffuser of a centrifugal compressor. Journal of Engineering for Gas Turbine and Power, 107: 507-513.

[32] Gao, C., Gu, C., Wang, T., and Yang, B. (2007). Analysis of geometries' effects on rotating stall in vaneless diffuser withwavelet neural networks. International Journal of Rotating Machinery, Volume 2007, Article ID 76476, 10pages, doi:10.1155/2007/76476.

[33] Garnier, V. H., Epstein, A. H, and Greitzer. E. M. (1990). Rotating waves as a stall inception indication in axial compressors. ASME Paper 90-GT-156.

[34] Hoying, D. A. (1995). Stall inception in a multistage high-speed axial compressor. AIAA Journal of Propulsion and Power, 11(5): 915-922.

[35] Inoue, M., Kuroumaru, M., Tanino, T., and Furukawa, M. (2000). Propagation of multiple short length-scale stall cells in an axial compressor rotor. ASME Paper 99-GT-97.

[36] Ishida, M., Sakaguchi, D., and Ueki, H. (2001). Suppression of rotating stall by wall roughness control in vaneless diffusers of centrifugal blowers. Journal of Turbomachinery, 123: 64-72.

[37] Ishida, M., Surana, T., Ueki, H., and Sakaguchi, D. (2005). Suppression of unstable flow at small flow rates in a centrifugal blower by controlling tip leakage flow and reverse flow. Journal of Turbomachinery, 127: 76-83.

[38] Jansen, W. (1964a). Rotating stall in a radial vaneless diffuser. Journal of Basic Engineering-Transactions of the ASME, 86(4): 750-758.

[39] Jansen, W. (1964b). Steady fluid flow in a radial vaneless diffuser. Journal of Basic Engineering-Transactions of the ASME, 86(3), 607-617.

[40] Johnston, J. P., and Dean, Jr. R. C. (1966). Losses in vaneless diffusers of centrifugal compressors and pumps: analysis, experiment, and design. Journal of Engineering for Power, 88(1): 49-60.

[41] Kang, J. S., and Kang, S. H. (2001). Stall inception in a high-speed centrifugal compressor. ASME Paper 2001-GT-301.

[42] Kurokawa, J., Saha, S. L., Matsui, J., and Kitahora, T. (2000). Passive control of rotating stall in a parallel-wall vaneless diffuser by radial grooves. Journal of Fluids Engineering, 122: 90-96.

[43] Lakshminarayana, B., Runstedler, P. W. Jr. (1980). Measurement methods in rotating components of turbomachinery. New York: ASME.

[44] Lawless, P. B., and Fleeter, S. (1995). Rotating stall acoustic signature in a low-speed centrifugal compressor: Part1-vaneless diffuser. ASME Journal of Turbomachinery, 117:87-96.

[45] Lennemann, E., and Howard, J. H. G. (1970). Unsteady flow phenomena in rotating centrifugal impeller passages. ASME Paper 69-GT-35.

[46] Ligrani, P. M., Van Den Braembussche, R., and Roustan, M. (1982). Rotating stall measurements in the vaneless diffuser of a radial flow compressor. ASME Paper 82-GT-257.

[47] Ljevar, S., de Lange, H. C., and van Steenhoven, A. A. (2005). Rotating stall characteristics in a wide vaneless diffuser. Proceedings of ASME Turbo Expo 2005, Reno-Tahoe, Nevada, USA.

[48] Ljevar, S., de Lange, H. C., and van Steenhoven, A. A. (2006a). Two-dimensional rotating stall analysis in a wide vaneless diffuser. International Journal of Rotating Machinery, Volume 2006 (2006), Article ID 56420, 11 pages.

[49] Ljevar, S., de Lange, H. C., van Steenhoven, A. A., Dupont, P., Caignaert, G., and Bois, G. (2006b). Core flow instability in wide vaneless diffusers for the purpose of rotating stall investigation. In The 13th International Conference on Fluid Flow Technologies, Budapest, Hungary, September 6 – 9.

[50] Ljevar, S., de Lange, H. C., van Steenhoven, A. A. (2006c). Comparison of rotating stall characteristics between the viscid and inviscid two dimensional model. WSEAS Transaction of Fluid Mechanics, 5(1): 480-487.

[51] Ljevar, S., de Lange, H. C., van Steenhoven, A. A. (2006d). Comparison of a two-dimensional viscid and inviscid model for rotating stall analysis. in Proceedings of the 4th WSEAS International Conference on Fluid Mechanics and Aerodynamics, Crete, Greece, August 21-23.

[52] Ljevar, S., de Lange, H. C., van Steenhoven, A. A. (2006e). Two-dimensional rotating stall analysis in a wide vaneless diffuser. International Journal of Rotating Machinery, vol. Volume 2006, pp. 1-11.

[53] Ljevar, S. (2007). *Rotating stall in wide vaneless diffusers*. PhD thesis, Eindhoven University of Technology, Netherlands.

[54] Lucius, A., and Brenner, G. (2011). Numerical simulation and evaluation of velocity fluctuations during rotating stall of a centrifugal pump. ASME Journal of Fluids Engineering, 133: 081102-1 – 081102-8.

[55] Mathioudakis, K., and Breugelmans., F. A. E. (1985). Development of small rotating stall in a single stage axial compressor. ASME Paper 85-GT-227.

[56] McDougal, N., Cumpsty, N., and Hynes, T. (1990) Stall inception in axial compressors. ASME Journal of Turbomachinery, 112(1):116-125.

[57] Mizuki, S., Park, C. W., and Deckker, B. E. L. (1985). Unstable flow in the vaneless diffuser of a centrifugal compressor at low flow rates. ASME Paper 85-IGT-7, 9 pages.

[58] Moore, F. K. (1989). Weak rotating flow disturbances in a centrifugal compressor with a vaneless diffuser. ASME Journal of Turbomachinery, 111:442-449.

[59] Moore, F. K. (1991). Theory of finite disturbances in a centrifugal compression system with a vaneless radial diffuser. ASME Paper 91-GT-82.

[60] Moreal, P. (1993*). Écoulements décollés dans une roue de pompe centrifuge*. PhD thesis, Université des Sciences et Technologies de Lille.

[61] Newell, A. C., and Whitehead, J. A. (1969). Finite bandwidth, finite amplitude convection. Journal of Fluid Mechanics. 28: 279-303.

[62] Ötügen, M. V., So, R. M. C., and Hwang, B. C. (1988). Diffuser stall and rotating zones of separated boundary layer. Experiments in Fluids, 1988, 6: 521-533.

[63] Pavesi, G., Dazin, A., Cavazzini, G., Caignaert, G., Bois, G., and Ardizzon, G. (2011) Experimental and numerical investigation of unforced unsteadiness in a vaneless radial diffuser. In Proceeding of the 9th european conference on turbomachinery-fluid dynamics and thermodynamics, pp. 625-636, Turkey.

[64] Saha, S. L., Kurokawa, J., Matsui, J., and Imamura, H. (2001). Passive control of rotating stall in a parallel-wall vaned diffuser by J-grooves. Journal of Fluids Engineering, 123: 507-515.

[65] Sano, T., Yoshida, Y., Tsujimoto, Y., Nakamura, Y., and Matsushima, T. (2002). Numerical study of rotating stall in a pump vaned diffuser. Journal of Fluids Engineering, 124: 363-370.

[66] Saxer-Felici, H. M., Saxer, A. P., Inderbitzin, A., and Gyarmathy, G. (1999). Prediction and measurement of rotating stall cells in an axial compressor. ASME Journal of Turbomachinery, 121: 365-375.

[67] Senoo, Y., and Kinoshita, Y. (1977). Influence of inlet flow conditions and geometries of centrifugal vaneless diffusers on critical flow angle for reverse flow. ASME Journal of Fluids Engineering, 99(1): 98–103.

[68] Senoo, Y., Kinoshita, Y., and Ishida, M. (1977). Asymmetric flow in vaneless diffusers of centrifugal blowers. ASME Journal of Fluids Engineering, 99(1):104-114.

[69] Senoo, Y., and Kinoshita, Y. (1978). Limits of rotating stall and stall in vaneless diffuser of centrifugal compressors. ASME Paper 78-GT-19.

[70] Shin, Y. H., Kim, K. H., and Son, B. J. (1998). An experimental study on the development of a reverse flow zone in a vaneless diffuser. JSME International Journal, Series B, 41(3): 546-555.

[71] Sinha, M., Pinarbasi, A., and Katz, J. (2001). The flow structure during onset and developed states of rotating stall within a vaned diffuser of a centrifugal pump. Journal of Fluids Engineering, 123: 490-499.

[72] Stewartson, K. and Stuart, J. (1971). A nonlinear instability theory for a wave system in plane Poiseuille flow. Journal of Fluid Mechanics. 48: 529-545.

[73] Tramm, P. C., and Dean, Jr. R. C. (1976). Centrifugal compressor and pump stability, stall and surge. New York: ASME.

[74] Tsujimoto, Y., Yoshida, Y., and Mori, Y. (1996). Study of vaneless diffuser rotating stall based on two-dimensional inviscid flow analysis. Journal of Fluids Engineering, 118: 123-127.

[75] Tsurusaki, H., Imaichi, K., and Miyake, R. (1986). A study on the rotating stall in vaneless diffusers of centrifugal fans: 1st report, rotational speeds of stall cells, critical inlet flow angle. Transactions of the JSME, Series B, 52(480): 2930-2938.

[76] Tsurusaki, H., and Mori, Y. (1988). A study on the rotating stall in vaneless diffusers of centrifugal fans: 3rd report, effect of diffuser radius. Transactions of the JSME, Series B, 54(500): 803-811.

[77] Tsurusaki, H., and Ichihara, T. (1988). A study on the rotating stall in vaneless diffusers of centrifugal fans: 4th report, effect of impellers. Transactions of the JSME, Series B, 54(503): 1661-1668.

[78] Tsurusaki, H., and Kinoshita, T. (2001). Flow control of rotating stall in a radial vaneless diffuser. Journal of Fluids Engineering, 123: 281-286.

[79] Wuibaut, G., Dupont, P., Bois, G., Caignaert, G., and Stanislas, M. (2001). Analysis of flow velocities within the impeller and the vaneless diffuser of a radial flow pump. Proceedings of the Institution of Mechanical Engineers, Part A: Journal of Power and Energy, 215(6): 801-808.

[80] Wuibaut, G., Bois, G., Dupont, P., Caignaert, G., and Stanislas, M. (2002a). PIV measurements in the impeller and the vaneless diffuser of a radial flow pump in design and off-design operating conditions. Journal of Fluids Engineering, 124: 791-797

[81] Wuibaut G., Bois, G., Dupont, P., and Caignaert, G. (2002b). Rotor stator interactions in a vaned diffuser of a radial flow pump for different flow rates using PIV measurement technique, 9th International Symposium on Transport Phenomena and Dynamics of Rotating Machinery, ISROMAC 9, 10 -14 Février 2002, Hawaii, USA, paper FD-ABS-018.

[82] Yoshida, Y., Murakami, Y., Tsurusaki, T., and Tsujimoto, Y. (1991) Rotating stall in centrifugal impeller/vaned diffuser systems. In Proceedings of the First ASME/JSME Joint Fluids Engineering Conference, 1991, FED-107, pp. 125-130.

[83] Zhu, Y. K., and Sjolander, S. A. (1987). Effect of geometry on the performance of radial vaneless diffusers. Journal of Turbomachinery, 109: 550-556.

Décrochage tournant dans un diffuseur lisse radial: Étude de stabilité et effet sur la performance

RESUME: Le comportement des turbomachines génératrices fonctionnant hors adaptation, et particulièrement à débit partiel, est sujet à des phénomènes d'instabilité qui peuvent affecter leur performance et peuvent être dramatiques pour les machines elles-mêmes ou leur environnement. Cette étude se concentre sur le décrochage tournant dans un diffuseur lisse radial. L'objectif est de proposer un modèle théorique capable de prédire rapidement les caractéristiques du décrochage tournant. Une étude expérimentale est effectuée en premier lieu, afin d'obtenir les caractéristiques de décrochage tournant dans un diffuseur lisse d'une roue radiale. L'effet du décrochage tournant sur la performance du diffuseur est discuté en se basant sur les mesures de la récupération de pression statique. Les résultats montrent que décrochage tournant améliore celle-ci, et un modèle simple, basé sur les longueurs de ligne de courant dans le diffuseur est proposé. Une étude de stabilité linéaire est proposée pour prédire les caractéristiques du décrochage tournant. Le taux d'accroissement des modes est utilisé pour déterminer les conditions critiques d'apparition du décrochage, et le mode dominant lorsque différents modes coexistent. Les champs de vitesse et de pression fluctuantes sont tracées pour décrire l'allure de l'écoulement en situation instable. Les capacités et les limites de cette étude sont discutées par comparaison entre les résultats théoriques et expérimentaux. Ensuite, une analyse faiblement non linéaire est introduite avec pour objectif de prendre en compte les interactions entre les modes qui sont négligées dans les approches linéaires.

Mots clés: Décrochage tournant, stabilité, turbomachines, linearité et non-linearité

Rotating instability in a radial vaneless diffuser: stability analysis and effect on the performance

ABSTRACT: The behavior of work-absorbing turbomachines operating at off design conditions, and especially at partial flow rates, is subject to instability phenomena that could affect their performance and can be dramatic for the machines or their environment. This study is focused on the rotating stall in the vaneless diffuser or a centrifugal machine: the objective is to propose a theoretical model able to predict the characteristics of such instability. An experimental study is performed to obtain the characteristics of rotating stall in a vaneless diffuser. The effect of rotating stall on the diffuser performance is discussed based on the static pressure recovery measurements. The results show that rotating stall is improving the diffuser pressure recovery, and a model based on the length of the diffuser streamlines is proposed to explain it. A linear stability analysis is proposed to predict the characteristics of rotating stall. The growth rate is used to determine the critical stall condition and the dominant stall mode when different stall modes are coexisting. The theoretical velocity and pressure fluctuations are also plotted to show the diffuser unstable flow. The abilities and limits of the linear stability analysis are discussed through the comparisons between theoretical and experimental results. Based on the linear model, a nonlinear stability analysis is the proposed to consider the nonlinear combinations which are neglected in the linear model.

Keywords: Rotating stall, stability analysis, turbomachinery, linear and non-linear